Alma Mater Studiorum - Università degli Studi di Bologna

DOTTORATO DI RICERCA

Modellistica Fisica per la Protezione dell'Ambiente

Ciclo XX

Settore scientifico disciplinare di afferenza: FIS/06

Retrieval of trace gases vertical profile in the lower atmosphere combining Differential Optical Absorption Spectroscopy with radiative transfer models

Presentata da:
Dott.ssa Elisa Palazzi

Relatore:
Chiar.mo Prof. Rolando Rizzi

Co-relatore:
Dott. Giorgio Giovanelli

Coordinatore:
Chiar.mo Prof. Ezio Todini

Esame finale anno 2008

Contents

List of Figures

List of Tables

Acronyms and abbreviations

ACS Absorption Cross Section

AMF Air Mass Factor

CCD Charged Coupled Device

CFC Chlorofluorocarbons

CNR National Research Council

COSPEC COrrelation SPECtrometer

DOAS Differential Optical Absorption Spectroscopy

ENEA Ente per le Nuove Tecnologie, l'Energia e l'Ambiente

ENVISAT ENVIronmental SATellite

EOS Earth Observing System

ERS European Remote Sensing

GASCOD Gas Analyzer Spectrometer Correlating Optical Differences

GDAS Global Data Assimilation System

GOME Global Ozone Monitoring Experiment

GOMOS Global Ozone Monitoring by Occultation of Stars

H-G Henyey-Greenstein

HYSPLIT Hybrid Single-Particle Lagrangian Integrated Trajectory

ISAC Institute of Atmospheric Sciences and Climate

IR Infrared

IRIS InfraRed Interferometer Spectrometer

IUGG International Union of Geodesy and Geophysics

LIDAR Light Detection And Ranging

LIMS Limb Infrared Monitor of the Stratosphere

MAX-DOAS Multiple AXis DOAS

MC Monte Carlo

MODTRAN MODerate resolution TRANsmittance

NASA National Aeronautics and Space Administration

NCEP National Centers for Environmental Prediction

NOOA National Oceanic and Atmospheric Administration

OA Off-Axis

OMI Ozone Monitoring Instrument

PROMSAR PROcessing of Multi-Scattered Atmospheric Radiation

RTE Radiative Transfer Equation

RTM Radiative Transfer Model

SAGE-II Stratospheric Aerosol and Gas Experiment-II

SCD Slant Column Density

SCIAMACHY SCanning Imaging Absorption spectroMeter for Atmospheric ChartographY

SIRS Satellite InfraRed Spectrometer

SZA Solar Zenith Angle

TOA Top Of the Atmosphere

TROPOGAS TROPOsheric GAScod

UTC Coordinated Universal Time

UV Ultraviolet

VCD Vertical Column Density

VRT Variance Reducing Technique

WMO World Meteorological Organization

Introduction

Historically, human activities have always interacted with the atmosphere, but the growth of population and industrialisation in the 19^{th} and 20^{th} century has led to dramatic changes in the Earth system. Long-term measurements have clearly shown that human activities are changing the composition of the Earth's atmosphere and research has demonstrated the important consequences of such changes for climate, human health, and the balance of ecosystems. As a consequence, in the last decades, several efforts have been made to develop new observational platforms, to model the future behaviour of the atmosphere, to understand the historic development of climate, to monitor anthropogenic and natural emissions as well as to collect knowledge for policy makers to facilitate their decisions.
The observational platforms for atmospheric composition comprise several components such as ground-based measurements (including *in-situ*, remote sensing and ballon instrumentation), aircraft measurements, satellite measurements as well as a data modelling system with assimilation to provide a comprehensive global picture.

Useful measurement techniques for atmospheric trace species should fulfill at least two main requirements. First, they must be sufficiently sensitive to detect the species under consideration at their ambient concentration levels. This can be a very demanding criterion; for instance, species present at mixing ratios ranging from as low as 0.1 ppt (mixing ratio of 10^{-13}, equivalent to about 2×10^6 molecules/cm^3) to several ppb (mixing ratio of 10^{-9}) can have a significant influence on the chemical processes in the atmosphere. Thus, detection limits from below 0.1 ppt to the ppb range are required, depending on the application. Second, it is equally important for measurement techniques to be specific, which means that the results of the measurement of a particular species must be neither positively nor negatively influenced by any other trace species simultaneously present in the probed volume of air. Given the large number of different molecules present at the ppt and ppb levels, even in clean air, this is also not a trivial condition.
Air monitoring by spectroscopic techniques has proven to be a very useful

tool to fulfill these desirable requirements as well as a number of other important properties. During the last decades, many such instruments have been developed which are based on the absorption properties of the constituents in various regions of the electromagnetic spectrum, ranging from the far infrared to the ultraviolet. Among them, Differential Optical Absorption Spectroscopy (DOAS) has played an important role.

DOAS is an established remote sensing technique for atmospheric trace gases probing, which identifies and quantifies the trace gases in the atmosphere taking advantage of their molecular absorption structures in the near UV and visible wavelengths of the electromagnetic spectrum (from 0.25 μm to 0.75 μm). DOAS has a flexible measurement configuration that allows multiple applications (ground-based, airborne and satellite-borne measurements are possible), and the investigation of the chemistry in the atmosphere to assess the influence of anthropogenic pollution and natural processes.

In the case of *passive* DOAS, which uses the sun as radiation source, the trace gases absorption is analyzed and quantified to conclude on the concentration of the trace gases integrated along the optical path between the sun and the receiver. Therefore, the ability to properly interpret UV/visible absorption measurements of atmopsheric constituents using diffuse sunlight depends crucially on how well the optical path of light collected by the system is understood.
The standard DOAS set-up as used for several decades was that in which radiation is collected along the vertical direction (zenith-sky DOAS), and has its highest sensitivity in the stratosphere, in particular during twilight. This is the result of the large enhancement in stratospheric light path at dawn and dusk combined with a relatively short tropospheric path.
The sensitivity of the instrument towards tropospheric signals can be strongly increased by pointing the telescope to the horizon instead of the zenith (off-axis DOAS). Depending on tropospheric visibility, the light path in the lower layers can become very long and increases as the viewing direction approaches the horizon. At the same time, the light path through the stratosphere is in good approximation independent of the instrument pointing.
The combination of simultaneous measurements at different off-axis angles is referred to as Multiple AXis DOAS (MAX-DOAS). This recent measurement technique is highly sensitive to the absorbers located in the lowest few kilometers of the atmosphere and has the advantage that vertical profile information can be retrieved by combining the simultaneous off-axis measurements with Radiative Transfer Model (RTM) calculations and inversion techniques.

The motivation for the work presented in this thesis is to retrieve profile information for the trace gases nitrogen dioxide (NO_2) and ozone (O_3) from a set of ground-based UV/visible MAX-DOAS measurements. NO_2 is an im-

portant trace gas in the lower troposphere due to the fact that it is involved in the production of tropospheric ozone. Ozone and nitrogen dioxide are key factors in determining the quality of air with impacts e.g. on human health and the growth of vegetation. To understand the NO_2 and ozone chemistry in more detail not only the concentrations at ground but also the acquisition of the vertical distribution of the trace gases is necessary. In fact, the budget of nitrogen oxides and ozone in the atmosphere is determined both by local emissions and non-local chemical and dynamical processes (i.e. diffusion and transport at various scales) that greatly impact on their vertical and temporal distribution: thus a tool to resolve the vertical profile information is really important.
DOAS offers the advantage to be a flexible and relatively simple technique, but it can detect the presence of a trace gas in terms of its integrated concentration over the atmospheric path (referred to as the *slant column density*) and it cannot measure directly the concentration as a function of location or altitude. To retrieve from such measurements the vertical profile of absorbers, sophisticated radiative transfer calculations have to be performed and inversion schemes applied. It should be intended that this is in strictly analogy with many satellite sounders for atmospheric composition.

To derive quantitative information on trace gases distributions, in fact, it is necessary to model the processes intervening along the light path with a Radiative Transfer Model (RTM). In particular there is a need for a RTM which is capable of dealing with such processes, supporting all DOAS geometries used, and treating multiple scattering events with varying phase functions involved. Deterministic radiative transfer models, for example, are affected by important limitations: they are often limited to two dimensions (or to plane parallel geometry) neglecting Earth sphericity and multiple scattering, and they cannot model all DOAS geometries which are used to retrieve the vertical profile of absorbers in the atmosphere.

To achieve the multiple goals mentioned above, a statistical approach based on the Monte Carlo technique can be used. A Monte Carlo RTM generates an ensemble of random photon paths between the light source and the detector, and uses these paths to reconstruct a remote sensing measurement. Within the present study, the radiative transfer model PROMSAR (PROcessing of Multi-Scattered Atmospheric Radiation) has been developed and used to correctly interpret the slant column densities obtained from MAX-DOAS measurements. PROMSAR allows to calculate the key processes as the solar transmittance, the irradiance and the radiance obtained by a detector with a specified position, viewing direction and field of view, and for a defined atmospheric scenario. Moreover, PROMSAR includes the Air Mass Factor (AMF) in the calculation, which is the most important output for the inter-

pretation of remote sensing DOAS measurements, allowing the conversion of the slant column density into a *vertical column density* (the concentration of the absorber integrated along the vertical). The air mass factor is defined as the ratio of the slant column density to the vertical column density and can be used to quantify the enhancement of the light path length within the absorber layers.

In order to derive the vertical concentration profile of a trace gas from its slant column measurement, the AMF is only one part in the quantitative retrieval process. One indispensable requirement is a robust approach to invert the measurements and obtain the unknown concentrations, the air mass factors being known. For this purpose, in the present thesis, we have used the *Chahine relaxation method*. This method had already been used in the past by several authors to estimate the profile information contained in zenith-sky DOAS measurements using ground-based instruments. The vertical resolution of such profiles was, however, relatively low and information was limited mainly to the stratospheric part of the profile. Within the study presented in this thesis, the Chahine inversion method has been modified so as to be applied for inversion of ground-based Multiple AXis DOAS measurements and retrieval of the vertical profile of the trace gases of interest in the lower troposphere.

The outline of this work is as follows: in **chapter 1** an overview on the fundamentals of atmospheric chemistry and physics is given, with the aim of introducing some important aspects necessary to understand the research presented in this thesis. The main aspects are the structure and composition of the Earth's atmosphere, and the processes that concur in the attenuation of solar radiation, such as scattering and absorption by gases and particles and their effects on visibility.
Chapter 2 deals with the DOAS technique and especially the novel Multiple AXis Differential Optical Absorption Spectroscopy (MAX-DOAS). Chapter 2 also presents the results of a comparison exercise between radiative transfer models from different international research groups carried out in 2005/2006, which has been fundamental to point out new aspects connected with this technique and the importance to correctly model the MAX-DOAS measurements.
Chapter 3 outlines the theory of radiative transfer for the atmosphere necessary for a proper interpretation of remote sensing data. Moreover, it extensively describes the PROMSAR radiative transfer model, which is suitable for the interpretation of passive DOAS mesurements under different viewing directions and instrumental settings. This model participated to the inter-

comparison exercise described in chapter 2. In chapter 3, investigations with the PROMSAR model for a variety of DOAS geometries, other than those shown in chapter 2, are performed and discussed. The development and use of the PROMSAR model has represented a primary goal of this thesis.
Chapter 4 illustrates briefly the retrieval theory in the remote sensing context, following mainly the work of Rodgers. One particular method, the Chahine relaxation method, is described for which an important application is discussed in chapter 5.
Chapter 5 presents the vertical profile of nitrogen dioxide and ozone from the application of the PROMSAR RTM and the Chahine inversion method to an event of pollutants transport observed at Castel Porziano (near Rome) in October 2006.
Conclusions provide the main surveys of this work and give the perspective of future applications.

Chapter 1

Absorption and scattering of UV and visible solar radiation in the atmosphere

Aerosol particles and gases scatter and absorb radiation as a function of wavelength. In this chapter, attention will be focused on absorption and scattering of near-ultraviolet and visible solar radiation (from 0.25 to 0.75 μm), as these are relevant processes for the Differential Optical Absorption Spectroscopy (DOAS) technique. DOAS is a spectroscopic technique which determines the integrated concentration of a trace gas along the light path that radiation covers in the atmosphere, by means of the trace gas absorption characteristics in the UV/visible spectral ranges. The trace gases present along the light path absorb the light at wavelengths which are unique to the respective molecular structure, allowing for the identification of the species. From the strength of the absorption conclusions can be drawn about the trace gases concentration. Also scattering by molecules and absorption and scattering by aerosol particles have to be taken into account in the processing of recorded spectra by DOAS methodology, because these processes influence the quantity and intensity of solar radiation that reaches the instrument. The DOAS technique will be dealt with in detail in chapter 2.

In this chapter, some considerations about visibility are also made, because it is strictly connected to the presence of aerosol particles and molecules in the atmosphere and their interaction with solar radiation. In polluted cloud free air the main process reducing visibility is aerosol particle scattering. Particles absorption of visible light is relevant only when soot (black carbon and organic matter) is present. Gas absorption is important only when nitrogen dioxide concentrations are high. Instead gas scattering always occurs but it is important relative to other processes only in clean air.

In the first section of this chapter the composition and structure of the atmosphere are briefly described because these aspects are important to the understanding of the research presented in this study.

1.1 Composition and structure of the Earth's atmosphere

To describe the interaction of the Earth's atmosphere with solar radiation, it is essential that the atmosphere's composition is understood. The atmosphere is composed of a group of nearly permanent gases and a group of gases with variable concentrations. In addition, the atmosphere also contains various solid and liquid particles such as aerosols, water drops, and ice crystals, which are highly variable in space and time. Tables 1.1 and 1.2 list the chemical formula and volume ratio for the concentrations of the permanent and variable gases in the atmosphere, respectively. For variable gases, also an indication of their major sources is given in Table 1.2.

Table 1.1: *Volume mixing ratios of fixed gases in the lowest 100 km of the Earth's atmosphere.*

Gas name	Major remarks	Chemical formula	Volume mixing ratio	
			%	ppmv
Molecular nitrogen	Biological	N_2	78.08	780000
Molecular oxygen	Biological	O_2	20.95	209500
Argon	Inert	Ar	0.93	9300
Neon	Inert	Ne	0.0015	15
Helium	Inert	He	0.0005	5
Krypton	Inert	Kr	0.0001	1
Xenon	Inert	Xe	0.000005	0.05

It is apparent from Table 1.1 that nitrogen, oxygen and argon account for more that 99.99% of the permanent gases, which are characterized by the fact that their mixing ratios do not vary very much in time or space. Although the mixing ratio of the permanent gases is constant with increasing altitudes, their partial pressure decreases with increasing altitudes because air pressure decreases with increasing altitudes and the permanent gases partial pressures are constant fractions of air pressure. The noble fixed gases possess very long lifetimes against chemical destruction and, hence, are relatively well mixed throughout the entire homosphere (i.e., below 100 km).

Table 1.2: *Volume mixing ratios of some variable gases in three atmospheric regions: clean troposphere, polluted troposphere, and stratosphere.*

Gas name	Major sources and remarks	Chemical formula	Volume mixing ratio (ppbv)		
			Clean troposphere	Polluted troposphere	Stratosphere
Inorganic					
Water vapour	Volcanic, evaporation	H_2O	3000-4.0·10^7	(0.5-4.0)·10^7	3000-6000
Carbon dioxide	Volcanic, biogenic, anthropogenic	CO_2	365000	365000	365000
Carbon monoxide	Photochemical, anthropogenic biogenic	CO	40-200	2000-10000	10-60
Ozone	Photochemical	O_3	10-100	10-350	1000-12000
Sulfur dioxide	Photochemical, volcanic, anthropogenic	SO_2	0.02-1	1-30	0.01-1
Nitric oxide	Anthropogenic biogenic, lightning, photochemical	NO	0.005-0.1	0.05-300	0.005-10
Nitrogen dioxide	Photochemical	NO_2	0.01-0.3	0.2-200	0.005-10
CFC-12		CF_2Cl_2	0.55	0.55	0.22
Organic					
Methane	Biogenic, anthropogenic	CH_4	1800	1800-2500	150-1700
Ethane		C_2H_6	0-2.5	1-50	Negligible
Ethene		C_2H_4	0-1	1-30	Negligible
Formaldehyde	Photochemical	HCHO	0.1-1	1-200	Negligible
Toluene		$C_6H_5CH_3$	Negligible	1-30	Negligible
Xylene		$C_6H_4(CH_3)_2$	Negligible	1-30	Negligible
Methyl chloride	Biogenic, anthropogenic	CH_3Cl	0.61	0.61	0.36

Table 1.2 summarizes the volume mixing ratios of some variable gases in the clean troposphere, the polluted troposphere (e.g., urban areas), and in the stratosphere divided also in organic and inorganic gases. Many organic gases have low mixing ratios in the stratosphere because they degrade chemically before they reach this region.

Most of the constituents of air that are of prime importance in atmospheric chemistry are present in very small concentrations, consequently they are called *trace constituents*. Some of them influence the transmission of solar and terrestrial radiation in the atmosphere and are therefore linked to the physical climate system. They are key components of biogeochemical cycles; in addition, they determine the "oxidizing capacity" of the atmosphere and, hence, the atmospheric lifetime of biogenic and anthropogenic trace gases.

The role of the trace constituents nitrogen dioxide and ozone in urban en-

vironments and in the free troposphere, and the main chemical reactions in which these species are involved, are in particular discussed in the Appendix.

The vertical temperature profile for the standard atmosphere is depicted in Fig. 1.1. This profile represents typical conditions in middle latitudes.

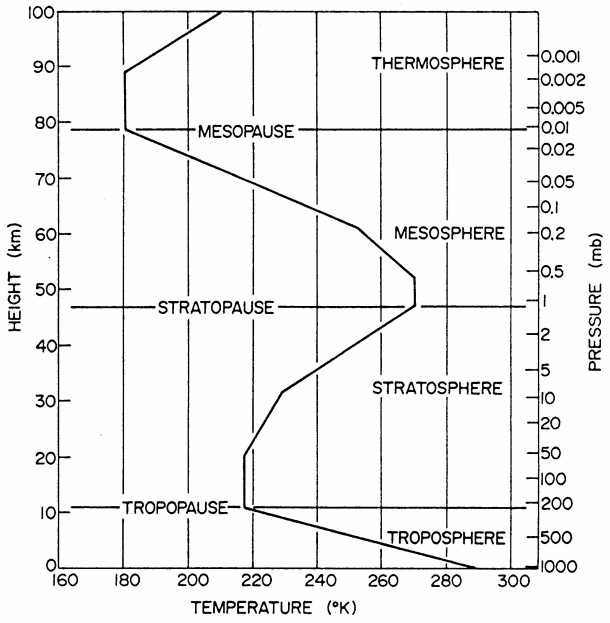

Figure 1.1: *Vertical profile of the temperature between the surface and 100 km altitude as defined in the U.S. Standard Atmosphere (1976) and related atmospheric layers. Note that the tropopause level is represented for mid-latitude conditions. From [1].*

According to the standard nomenclature defined by the International Union of Geodesy and Geophysics (IUGG) in 1960, the vertical temperature profile is divided into four distinct layers. These are the *troposphere*, *stratosphere*, *mesosphere* and *thermosphere*. The tops of these layers are respectively called tropopause, stratopause, mesopause, and thermopause.

The troposphere is characterized by a decrease of temperature with respect to height with a typical lapse rate of 6.5° C/km. The temperature structure in this layer is a consequence of the radiative balance and the convective transport of energy from the surface to the atmosphere. The ground surface receives energy from the sun daily, heating the ground, but the top of the troposphere continuously radiates energy upward, cooling the upper troposphere. Convective thermals from the surface transfer energy upward, but as these thermals rise into regions of lower pressure, they expand and cool,

resulting in a decrease of temperature with increasing height in the troposphere. Virtually all the water vapour, cloud, and precipitation are confined in this layer.
The boundary layer is the region of the troposphere where surface effects are important. Stull [2] defines the atmospheric boundary layer as "the part of the troposphere that is directly influenced by the presence of the Earth's surface, and responds to surface forcings with a time scale of about an hour or less". The boundary layer differs from the "free troposphere" in that the temperature profile responds to changes in ground temperatures over a period of less than an hour, whereas the temperature profile in the free troposphere responds to changes in ground temperatures over a longer period. The boundary layer depth is of the order of 1 km, but varies significantly with the time of day and with meteorological conditions. The exchange of chemical compounds between the surface and the free troposphere is directly dependent on the stability of the boundary layer.
The tropopause is the upper boundary of the troposphere. Above the tropopause base, temperatures are relatively constant with increasing altitude. Tropopause heights are higher (15 to 18 km) over the equator than over the poles (8 to 10 km). Strong vertical motions over the equator raise the base of the ozone layer there. Because ozone is responsible for warming above the tropopause, pushing ozone to greater heights over the equator increases the altitude at which warming begins. Near the poles, downward motions move stratospheric ozone downward, lowering the tropopause height over the poles. Temperatures at the tropopause over the equator are colder than they are over the poles. One reason is that the higher base of the ozone layer over the equator allows tropospheric temperatures to cool to a greater altitude over the equator than over the poles. A second reason is that lower- and mid-tropospheric water vapour contents are much higher over the equator than they are over the poles. Water vapour absorbs thermal-IR radiation emitted from the Earth's surface, preventing that radiation to reach the upper troposphere. The troposphere, which contains about 85-90% of the atmospheric mass, is often dynamically unstable with rapid vertical exchanges of energy and mass being associated with convective activity. Globally, the time constant for vertical exchanges is of the order of several weeks.

The stratosphere is characterized by an isothermal layer from the tropopause to about 20 km from where the temperature increases to the stratopause. Ozone occurs chiefly in the stratosphere causing the inversion temperature. Ozone absorbs the UV radiation from sun (with wavelengths between 0.23 and 0.32 μm) and reemits thermal-infrared radiation, heating in this way the stratosphere. Peak stratospheric temperatures occur at the top of the stratosphere (about 50 km) because this is the altitude at which ozone

absorbs the shortest UV wavelengths (about 0.175 μm) reaching the stratosphere. Although the content of ozone at the top of the stratosphere is low, each ozone molecule can absorb these short wavelengths, increasing the average kinetic energy and, by consequence, temperature of all molecules. Short UV wavelengths do not penetrate to the lower stratosphere. Ozone densities in the stratosphere peak from 25 to 32 km. In addition, thin layers of aerosol are observed to persist for a long period of time within certain altitude ranges of the stratosphere. A typical residence time for material injected in the lower stratosphere is one to three years.

Like the troposphere the temperatures in the mesosphere decrease with height from about 50 to about 85 km. Ozone densities are too low in comparison with those of oxygen and nitrogen for ozone absorption of UV radiation to affect the average temperature of all molecules in the mesosphere. In this region dynamical instability occurs frequently and is characterized by rapid vertical mixing.

Above 85 km and extending upward to an altitude of several hundred kilometers lies the thermosphere where temperatures range from 500 K to as high as 2000 K, depending on the solar activity. In the thermosphere temperatures increase with increasing altitude because O_2 and N_2 absorb very short far-UV wavelengths (< 0.1 μm), that in such way do not penetrate to the mesosphere. Vertical exchanges associated with dynamical mixing become insignificant, but molecular diffusion becomes an important process that produces gravitational separation of species according to their molecular or atomic weight.

1.2 Absorption in the UV/visible solar spectrum

Before we proceed to discuss the absorption of solar radiation in the near-ultraviolet and visible regions (from 0.25 to 0.75 μm), it would be helpful to introduce the ways in which a molecule can store various energies.

Any moving particle has kinetic energy as a result of its motion in space. This is known as *translational energy*. The averaged translational kinetic energy of a single molecule in the X, Y, and Z directions is found to be equal to $KT/2$, where K is the Boltzmann constant (5.67×10^{-8} $\mathrm{Wm^{-2}K^{-4}}$) and T is the absolute temperature.

The molecule which is composed of atoms can rotate about an axis through its center of gravity and, therefore, has *rotational energy*.

The atoms of the molecule are bounded by certain forces in which the

individual atoms can vibrate about their equilibrium positions relative to one other. The molecule therefore will have *vibrational energy*.

These three molecule energy types are based on a rather mechanical model of the molecule that ignores the detailed structure of the molecule in terms of nuclei and electrons. It is possible, however, for the energy of a molecule to change due to a change in the energy state of the electrons of which it is composed. Thus, the molecule has *electronic energy*.

Rotational, vibrational and electronic energies are quantized and take discrete values only. Absorption and emission of radiation take place when the atoms or molecules undergo transitions from one energy state to another. In general, these transitions are governed by selection rules. Atoms can exhibit line spectra associated by electronic energy. Molecules, however, can have two additional types of energy which lead to complex band systems.

Solar radiation is mainly absorbed in the atmosphere by O_2, O_3, N_2, CO_2, H_2O, O, and N, although gases which occur in very small quantities also exhibit absorption spectra. Absorption spectra due to electronic transitions of molecular and atomic oxygen and nitrogen, and ozone occur chiefly in the ultraviolet region, while those due to the vibrational and rotational transitions of triatomic molecules such as H_2O, O_3 and CO_2 lie in the infrared region. Figure 1.2 shows the spectrum of solar radiation reaching the Earth's surface for the case of an overhead sun (the lower curve) together with the spectrum of solar radiation incident upon the top of the atmosphere (the upper curve). The area between the two curves represents the depletion of the incident radiation during its passage through the atmosphere. The depletion is divided into two parts: the unshaded area represents the combined effects of backscattering and absorption by clouds and aerosol, and backscattering by air molecules, while the shaded area represents the absorption by air molecules. Nearly all the shaded area can be identified with discrete absorption bands, the most important of these being the water vapour bands in the in the near infrared. There is very little absorption of solar radiation at visible wavelengths by the gaseous constituents of the atmosphere. This remarkable *window* in the absorption spectrum coincides with the wavelengths of maximum solar emission.

Table 1.3 shows the gases that absorbs UV and visible radiation. Of the gases listed in Table 1.3 only ozone, NO_2 and NO_3 absorb in the visible spectrum. The rest absorbs in the ultraviolet spectrum. Absorption by ozone is weak in the visible spectrum and concentrations of the nitrate radical (NO_3) are relatively low except at night, when sunlight is absent, as explained in the Appendix. Probably the most important molecule having substantial absorption in the visible is NO_2, which has significant absorption in the blue region of the spectrum, near 0.430 μm. As already pointed out at the

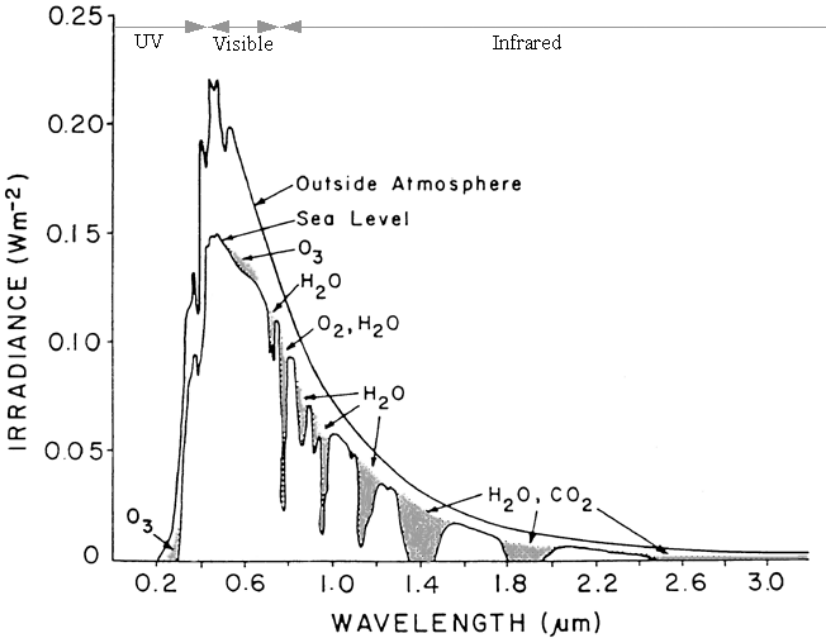

Figure 1.2: *Spectrum of solar radiation at the top of the atmosphere (upper curve) and at sea level (lower curve) for average atmospheric conditions and an overhead sun. The shaded area represents absorption by gaseous constituents, as indicated.*

beginning of this chapter, absorption of solar radiation by trace gases is dealt with, in this thesis, within the field of application of the DOAS technique. In particular, attention will be focused on tropospheric ozone and nitrogen dioxide, for which the absorption cross section in the UV/visible part of the solar spectrum is shown in Fig. 1.3. The part of the solar spectrum between 200 and 300 nm primarily is absorbed by the ozone in the upper stratosphere and mesosphere. The regions which consist of the strongest absorption bands of O_3 are called *Hartley bands*. The bands between 300 and 360 nm are called *Huggins bands*, which are not as strong as Hartley bands. O_3 also shows weak absorption bands in the visible (and near infrared) region, called *Chappuis bands*. The role of nitrogen dioxide in the absorption of solar radiation has been widely discussed in [3].

1.2.1 The Beer-Bouguer-Lambert law

A pencil of radiation traversing a medium will be weakened by its interaction with matter. If the intensity of radiation I_λ becomes $I_\lambda + dI_\lambda$ after traversing a thickness ds in the direction of its propagation, as depicted in Fig. 1.4,

Table 1.3: *Wavelengths of absorption in the visible and UV spectra by several gases.*

Gas name	Chemical formula	Absorption wavelengths (μm)
Visible/near-UV/ far-UV absorbers		
Ozone	O_3	<0.35, 0.45-0.75
Nitrate radical	NO_3	<0.67
Nitrogen dioxide	NO_2	<0.71
Near-UV/far-UV absorbers		
Nitrous acid	HONO	<0.4
Dinitrogen pentoxide	N_2O_5	<0.38
Formaldehyde	HCHO	<0.36
Hydrogen peroxide	H_2O_2	<0.35
Acetaldehyde	CH_3CHO	<0.345
Peroxynitric acid	HO_2NO_2	<0.33
Nitric acid	HNO_3	<0.33
Peroxyacetyl nitrogen	$CH_3CO_3NO_2$	<0.3
Far-UV absorbers		
Molecular oxygen	O_2	<0.245
Nitrous oxide	N_2O	<0.24
CFC-11	$CFCl_3$	<0.23
CFC-12	CF_2Cl_2	<0.23
Methyl chloride	CH_3Cl	<0.22
Carbon dioxide	CO_2	<0.21
Water vapour	H_2O	<0.21
Molecular nitrogen	N_2	<0.1

then

$$dI_\lambda = -k_\lambda \cdot \rho \cdot I_\lambda \cdot ds, \tag{1.1}$$

where ρ is the density of the material, and k_λ denotes the mass extinction cross section (in units of area per mass) for radiation of wavelength λ. The mass extinction cross section is the sum of the mass absorption and scattering cross sections. Thus, the reduction in intensity is caused by absorption in the material as well as scattering of radiation by the material. On the other hand the intensity may be strengthened by emission of the material plus multiple scattering from all other directions into the pencil under consideration at the same wavelength. We define the source function coefficient j_λ such that the increase of the intensity due to emission and multiple scattering is given by:

$$dI_\lambda = j_\lambda \cdot \rho \cdot ds. \tag{1.2}$$

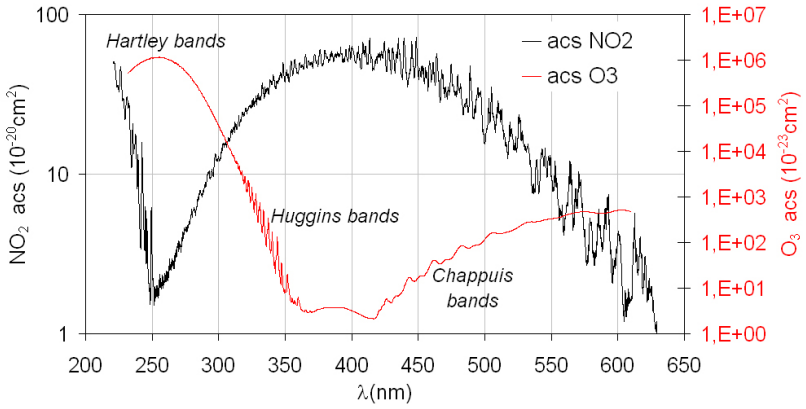

Figure 1.3: *Absorption cross section (acs) of NO_2 (left axis) and O_3 (right axis) in the wavelength interval (200-650) nm. A semi-logarithmic scale is used.*

Combining Eqs. 1.1 and 1.2 we obtain:

$$dI_\lambda = -k_\lambda \cdot \rho \cdot I_\lambda \cdot ds + j_\lambda \cdot \rho \cdot ds. \tag{1.3}$$

Moreover it is convenient to define the source function J_λ such that:

$$J_\lambda \equiv j_\lambda / k_\lambda. \tag{1.4}$$

It follows that Eq. 1.3 can be rearranged to yield:

$$\frac{dI_\lambda}{k_\lambda \cdot \rho \cdot ds} = -I_\lambda + J_\lambda. \tag{1.5}$$

When both multiple scattering and emission contributions may be neglected ($J_\lambda = 0$), and in the absence of scattering by the material, Eq. 1.5 only accounts for absorption in the material, and it reduces to the form:

$$\frac{dI_\lambda}{k_\lambda \cdot \rho \cdot ds} = -I_\lambda, \tag{1.6}$$

where k_λ now represents the mass absorption cross section (or simply *absorption coefficient*) only. The absorption coefficient is a measure of the fraction of the absorbers per unit wavelength interval that are absorbing radiation at the wavelength in question. If the incident intensity at $s = 0$ is $I_\lambda(0)$, as shown in Fig. 1.4, then the emergent intensity at a distance s can be obtained by integrating Eq. 1.6, and is given by:

$$I_\lambda(S_1) = I_\lambda(0) \cdot e^{(-\int_0^{S_1} k_\lambda \cdot \rho \cdot ds)} \tag{1.7}$$

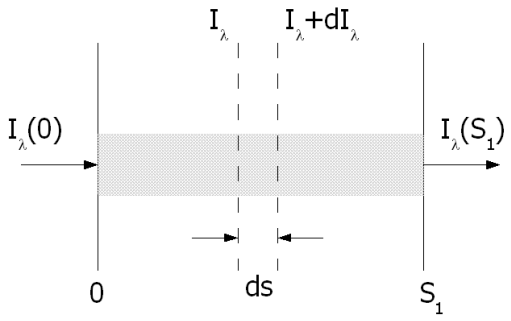

Figure 1.4: *Depletion of the radiant intensity in traversing an absorbing medium.*

Assuming that the medium is homogeneous, then k_λ is independent on the distance s. Thus by defining the path length u

$$u = \int_0^{S_1} \rho \cdot ds, \tag{1.8}$$

Eq. 1.7 becomes:

$$I_\lambda(S_1) = I_\lambda(0) \cdot e^{(-k_\lambda \cdot \mu)}. \tag{1.9}$$

This is known as *Beer-Bouguer-Lambert* law, which states that the decrease of the radiant intensity traversing a homogeneous absorbing medium is according to the simple exponential function whose argument is the product of the mass absorption cross section and the path length. The dimensionless quantity $(k_\lambda \cdot \mu)$ is called the *optical depth* or *optical thickness*. It is a measure of the cumulative depletion that the beam of radiation has experienced as a result of its passage through the medium.
It is important to note here that the Beer-Bouguer-Lambert law is the physical low on which the DOAS methodology is based, as will be shown in chapter 2. In the DOAS context the quantity u is referred to as *slant column density* (SCD), and indicates the trace gas concentration integrated along the light path.

1.3 Scattering of solar radiation

Most of the light that reaches our eyes comes not directly from its sources but indirectly by the process of scattering. We see diffusely scattered sunlight when we look at clouds or at the sky. The land and water surfaces, and the objects surrounding us are visible through the light that they scatter.

In the atmosphere, we see many colorful examples of scattering generated by molecules, aerosols, and clouds containing droplets and ice crystals. Blue sky, white clouds, rainbows and haloes, are samples of optical phenomena due to scattering.

Scattering is a fundamental physical process associated with the light and its interaction with the matter. By this process, a particle in the path of an electromagnetic wave continuously abstracts energy from the incident wave and reradiates that energy in all directions. The particle, therefore, may be thought of as a point source of the scattered energy. The radiation scattered by a particle results from the superposition of all wavelets scattered by oscillating dipoles. These dipoles, oscillating at the frequency of the applied electromagnetic field, produce a secondary field that radiates out in all directions (the scattered field). Particle scattering is a complex problem because the secondary waves generated by each dipole also act to stimulate oscillations in neighboring dipoles.

It is possible to formulate an expression analogous to Eq. 1.1 for the fraction of parallel beam radiation that is scattered when passing downward through a layer of infinitesimal thickness:

$$dI_\lambda = -K \cdot A \cdot I_\lambda \cdot ds, \tag{1.10}$$

where K is a dimensionless coefficient playing the role of a *scattering area coefficient*, and A is the cross-sectional area that the particles in a unit volume present to the beam of incident radiation. Thus, K measures the ratio of the effective scattering cross section of the particles to their geometric cross section. For the idealized case of scattering by spherical particles of uniform radius r, the scattering area coefficient K can be prescribed on the basis of theory. It is convenient to express K as a function of a dimensionless *size parameter* $\alpha = 2\pi r/\lambda$, which is a measure of the size of the particles in comparison to the wavelength of the incident radiation. Figure 1.5 shows a plot of α as a function of r and λ.

The scattering area coefficient K depends not only upon the size parameter but also upon the index of refraction of the particles responsible for the scattering. Figure 1.6, for example, shows K as a function of α for non-absorbing spheres with a refractive index of 1.33. For the special case of $\alpha \ll 1$ (the extreme left-hand side of Fig. 1.6), Rayleigh showed that, for a given value of the refractive index, $K \propto \alpha^4$ and the scattered radiation is evenly divided between the forward and backward hemispheres, as will be shown in section 1.3.1. When α is greater than 50, $K \simeq 2$ and the angular distribution of scattered radiation can be described by the principles of geometric optics, as will be shown in section 1.3.3. For intermediate values of

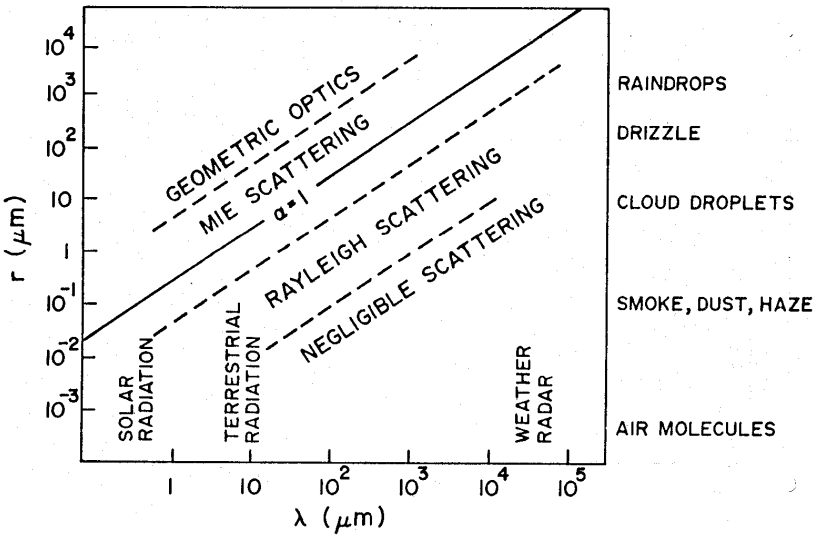

Figure 1.5: *Size parameter α as a function of wavelength of the incident radiation and particle radius. From [4].*

the size parameter, the scattering phenomenon must be described in terms of the more general theory developed by Mie (section 1.3.2). Within the Mie regime K exhibits the oscillatory behaviour shown in Fig. 1.6. The angular distribution of scattered radiation is very complicated and varies rapidly with α, with forward scattering predominating over back scattering.

In the atmosphere, the particles responsible for the scattering cover the sizes from gas molecules (10^{-8} cm) to large raindrops and hail particles ($\sim$ 1 cm). The relative intensity of the scattering pattern depends strongly on the ratio of particle size to wavelength of the incident wave.

1.3.1 Rayleigh scattering

When particles are much smaller than the incident wavelength ($\alpha \ll 1$), the scattering is called *Rayleigh scattering*, after Lord Baron Rayleigh born John William Strutt (1842-1919), who first described the properties of scattered sunlight by air molecules. Rayleigh's theoretical work on gas scattering was published in 1871 [6]; the English experimental physicist John Tyndall (1820-1893) demonstrated experimentally that the sky's blue color results from scattering of visible light by gas molecules and that a similar effect occurs with small particles.

Consider a small homogemeous, isotropic spherical particle whose radius is much smaller than the wavelength of the incident radiation. The simpli-

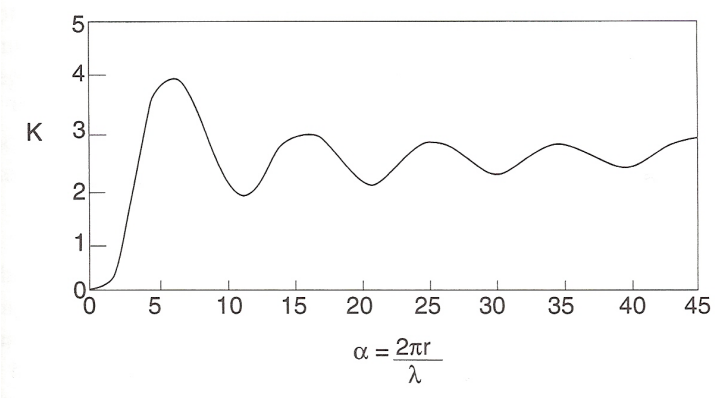

Figure 1.6: *Scattering area coefficient K as a function of size parameter α for nonabsorbing spheres with a refractive index of 1.33. From [5].*

fication introduced by the small size is that the incident radiation produces a homogeneous electric field E_0 which generates a dipole configuration on the small particle. The electric dipole causes an electric field which, in turn, modifies the applied field inside and near the particle; let E be the applied field plus the particle own's field. Let p_0 be the induced dipole moment, defined as (electrostatic formula)

$$p_0 = \alpha_0 \cdot E_0. \tag{1.11}$$

This relation defines α_0, the *polarizability* of the small particle. Since the dimension of E_0 is charge per area, and the dimension of p_0 is charge times length, α_0 has the dimension of a volume. In general, α_0 is a tensor. This means that the directions of p_0 and E_0 coincide only if the field is applied in one of three mutually perpendicular directions.
The applied field E_0 generates oscillation of an electric dipole in a fixed direction; the oscillating dipole, in turn, produces an electromagnetic wave, the scattered wave. The scattered electric field in regions which are far away from the dipole is given by

$$E = \frac{1}{c^2}\frac{1}{r}\frac{\partial^2 p}{\partial t^2}\sin\gamma, \tag{1.12}$$

where r denotes the distance between the dipole and the observational point, γ the angle between the scattered dipole moment p and the direction of observation and c the velocity of light ($c = 3 \times 10^8$ ms^{-1}). In an oscillating periodic field, p may be written in terms of the induced dipole moment as

$$p = p_0 \cdot e^{-ik(r-ct)} \tag{1.13}$$

where k is the wave number ($k = 2\pi/\lambda$). By combining Eqs. 1.11 and 1.13, Eq. 1.12 yields:

$$E = -E_0 \frac{e^{-ik(r-ct)}}{r} k^2 \alpha_0 \sin\gamma. \tag{1.14}$$

Now we consider the scattering of unpolarized sunlight by air molecules. In that circumstance, α_0 may be considered a scalar. Let the plane defined by the directions of incident and scattered waves be the reference plane (plane of scattering), with respect to which we define the perpendicular (E_r) and parallel (E_l) components of E. According to Eq. 1.14 we have:

$$E_r = -E_{0r} \frac{e^{-ik(r-ct)}}{r} k^2 \alpha_0 \sin\gamma_1 \tag{1.15}$$

$$E_l = -E_{0l} \frac{e^{-ik(r-ct)}}{r} k^2 \alpha_0 \sin\gamma_2, \tag{1.16}$$

where $\gamma_1 = \pi/2$ and $\gamma_2 = \pi/2 - \Theta$, where Θ is the angle between the incident and scattered waves (the *scattering angle*). The corresponding intensities (per solid angle $\Delta\Omega$) of the incident and scattered radiation may be written as

$$I_0 = \frac{1}{\Delta\Omega} \frac{c}{4\pi} \mid E_0 \mid^2, \quad I = \frac{1}{\Delta\Omega} \frac{c}{4\pi} \mid E \mid^2 . \tag{1.17}$$

Thus, Eqs. 1.15, 1.16 and 1.17 can be expressed in the form of intensities as

$$I_r = I_{0r} k^4 \alpha_0^2 / r^2 \tag{1.18}$$

$$I_l = I_{0l} k^4 \alpha_0^2 \cos^2\Theta / r^2 \tag{1.19}$$

where I_r and I_l are polarized intensity components perpendicular and parallel to the plane of scattering. The total scattered intensity of the unpolarized sunlight incident on a molecule in the directon of Θ is then

$$I = I_r + I_l = (I_{0r} + I_{0l} \cos^2\Theta) k^4 \alpha_0^2 / r^2. \tag{1.20}$$

But for unpolarized sunlight, $I_{0r} = I_{0l} = I_0/2$ and by noting that $k = 2\pi/\lambda$, we get

$$I = \frac{I_0}{r^2} \alpha_0^2 \left(\frac{2\pi}{\lambda}\right)^4 \cdot \frac{1 + \cos^2\Theta}{2}. \tag{1.21}$$

The term "1" in Eq. 1.21 corresponds to the r-component (electric vector perpendicular to the plane of scattering), and the term "$\cos^2\Theta$" corresponds

to the l-component of the scattered light (electric vector parallel).
Figure 1.7 illustrates Eq. 1.21 by the well known scattering diagram. The polar diagram represents the total intensity resulting from the sum of the polarized components contributions perpendicular to plane of drawing (1) and in plane of drawing ($\cos^2\Theta$); the light scattered by 90° is fully polarized in the r-direction (which is not true for anysotropic particles). Equation 1.21

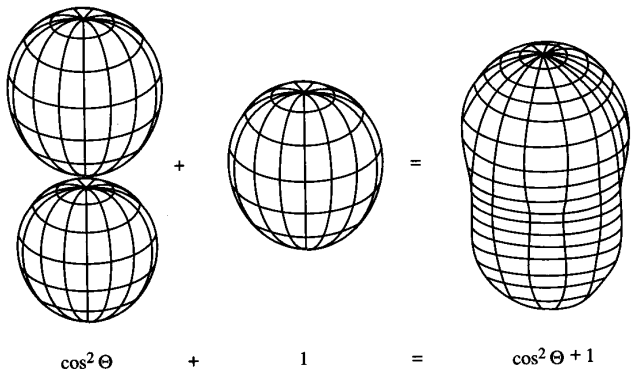

Figure 1.7: *Rayleigh scattering: polar diagram of scattered intensity if incident radiation is unpolarized.*

is the original formula derived by Rayleigh, by which the intensity scattered by a molecule for unpolarized sunlight is proportional to the incident intensity I_0 and is inversely proportional to the square of the distance between the molecule and the point of observation. In addition to these two factors, it also depends on the polarizability, the wavelength of the incident wave, and the scattering angle. Scattering of unpolarized sunlight by molecules has maxima in the forward ($\Theta = 0°$) and backward ($\Theta = 180°$) directions, whereas it shows minima in the side directions ($\Theta = 90°$ and 270°). The inverse dependence of the scattered intensity on the wavelength to the fourth power is the foundation for the explanation of the blue of the sky. It is apparent that the λ^{-4} low causes more of the blue light to be scattered than the red, the green and the yellow, and so the sky, when viewed away from the sun's disk appears blue.

It can be seen in Fig. 1.5 that Rayleigh scattering describes not only how visible radiation is scattered by atmospheric gases, but also how the longer wavelength infrared radiation is scattered by aerosol particles a few tenths of a micron in size, and how, the even longer microwave radiation is scattered by cloud droplets and small rain drops.

1.3.2 Mie scattering

Larger particles in the atmosphere such as aerosols, cloud droplets, and ice crystals, also scatter sunlight and produce many fascinating optical phenomena. However, their single scattering properties are less wavelength-selective and depend largely upon the particle size.
The dipole mode of the electric field, which leads to the development of the Rayleigh scattering theory, is not applicable for particles larger than the wavelength of the incident radiation. Because of the large particle size, the incident beam of light induces high-order modes of polarization configuration, which require more advanced treatment.

Scattering by a spherical particle of arbitrary size has been treated exactly by Gustav Mie (1868-1957) in 1908 [7], by means of solving the electromagnetic wave equation derived from the fundamental Maxwell equations.

Figure 1.8 illustrates the scattering diagram for scattering by a particle in the Mie regime (α=1.0, 1.5, 3, 6, 20 from top to bottom). The scattering appears extremely directional in the forward direction: the larger the particle, the more it scatters forward and the greater the forward to backward asymmetry. The forward component (forward peak) dominates with respect to the backward component because forward moving waves tend to be in phase and this gives a large resultant amplitude whereas backward waves tend to be out of phase and this results in a small resultant amplitude.

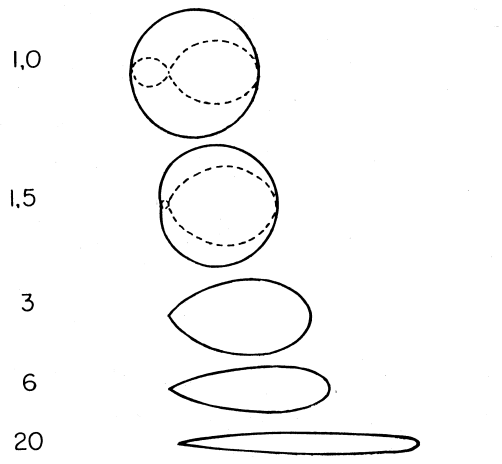

Figure 1.8: *Mie scattering: polar diagram of scattered intensity. α=1.0, 1.5, 3, 6, 20 from top to bottom.*

Mie scattering occurs when particles have about the same size as ($\alpha \sim 1$) or are greater than ($\alpha > 1$) the wavelength of radiation. The scattering of

sunlight by particle of haze, smoke, smog, and dust usually falls within this regime.

1.3.3 Geometric scattering

Particles for which the radius is much greater than the wavelength of light ($\alpha \gg 1$) fall into the so-called *geometric scattering* regime. In this case, the scattering can be determined from geometrical optics of reflection, refraction and diffraction. Geometric optics means that the scattering of light can be determined by ray tracing, which is also used to determine the optical effects of lenses and prisms, etc.
A good example of the application of geometric optics to particle scattering is the formation of a rainbow. Figure 1.9 shows the ray paths in a single droplet that contribute to the formation of a primary rainbow. Light beams

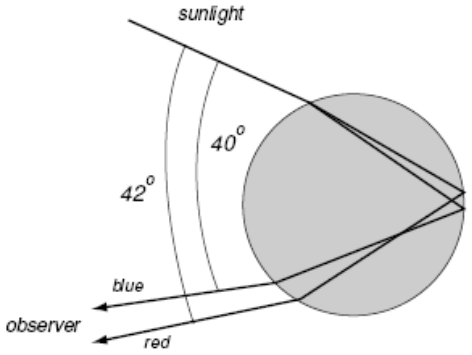

Figure 1.9: *Ray paths inside a droplet that lead to the formation of a rainbow.*

entering a droplet are first refracted (leading to dispersion), reflected off the back of the droplet and refracted again on leaving the droplet. Independent of the size of the droplet (provided $\alpha \gg 1$) the angle between the incident beam and the return beam is 42° for red light and 40° for the blue light. Note that not all the light that impinges the droplet goes into forming the rainbow. Much of it is simply reflected off the surface or is refracted and then exits the droplet in the forward direction. Note also that only one wavelength from a single droplet impinges upon the viewer's eye. A rainbow appears when waves from many droplets hit the eye.
For geometric scattering by a sphere, the fraction of incident light that is scattered (expressed in terms of the scattering area coefficient K) is 2. This means that a sphere with radius much greater than the wavelength of light scatters twice as much energy as it intercepts. This is because light is not

only redirected by refraction and reflection (for rays that enter the droplet) but also diffracted about the sphere. Thus a droplet can "intercept" light waves that would otherwise pass by.

1.4 Visibility

Visibility is a measure of how far we can see through the air. Perhaps one of the most noticeable effects of air pollution is reduction in visibility. Even in cleanest air, however, our ability to see along the Earth's horizon is limited to a few hundred kilometers by background gases and aerosol particles. If we look up through the sky at night, however, we can discern light from stars that are millions of kilometers away. The difference is that more gas molecules and aerosol particles lie in front of us in the horizontal line of sight than in the vertical one.
The regulatory definition of visibility is the *meteorological range*. It can be defined as the distance from an observer at which an ideal black object just disappears when viewed against the horizon sky in daytime. It can better be explained in terms of the following example. Suppose a perfectly absorbing dark object lies against a white background at a point x_0, as shown in Fig. 1.10. Because the object is perfectly absorbing, it reflects and emits no visible

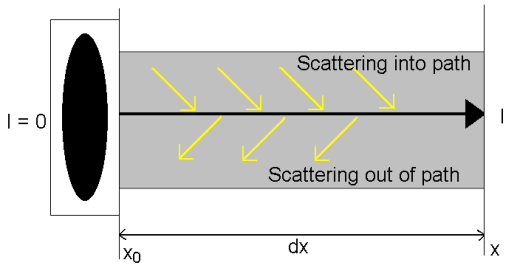

Figure 1.10: *Change of radiation intensity along a beam. A radiation beam originating from a dark object has intensity I=0 at point x_0. Over a distance dx the beam's intensity increases due to scattering of background light into the beam. This added intensity is diminished somewhat by along the beam and scattering out of the beam.*

radiation; thus, its visible radiation intensity (I) at point x_0 is zero and it appears black. As a viewer backs away from the object, background white light of intensity I_B scatters into the field of view, increasing the intensity of light in the viewer's direction. Although some of the added background light is scattered out of the field of view or absorbed along it by gases and aerosol

particles, at some distance away from the object, so much background light has entered the path that the viewer can barely discern the black object against the background light.
The meteorological range is a function of the *contrast ratio* which is defined as

$$C_{ratio} = \frac{I_B - I}{I_B}, \tag{1.22}$$

where I is the intensity of object and I_B the intensity of background. The contrast ratio gives the difference between the background intensity and the intensity of the object in the viewer's line of sight, all relative to the background intensity. If the contrast ratio is unity, than an object is perfectly visible; if it is zero, than the object cannot be distinguished from the background. The meteorological range is the distance from an object at which the contrast ratio equals the *liminal contrast ratio* of 0.02 (2%). The liminal contrast ratio is the lowest visually perceptible brightness contrast a person can see. It obviously varies from individual to individual. In 1924 Koschmieder selected the value of 0.02, which has become an accepted liminal contrast value for meteorological range calculation. The meteorological range is therefore the distance from an ideal dark object at which the object has a 0.02 liminal contrast ratio against a white background. The meteorological range value can be derived from the equation describing the change in object intensity along the path. This equation is:

$$\frac{dI}{dx} = \sigma_t \cdot (I_B - I), \tag{1.23}$$

where all wavelength subscripts have been removed; σ_t is the total extinction coefficient, $(\sigma_t \cdot I_B)$ accounts for the scattering of background light radiation into the path and $-(\sigma_t \cdot I)$ for the attenuation of radiation along the path due to scattering out of the path and absorption along the path. A total extinction coefficient is expressed as the sum of extinction coefficients due to scattering and absorption by gases and particles:

$$\sigma_t = \sigma_{a,g} + \sigma_{s,g} + \sigma_{a,p} + \sigma_{s,p}. \tag{1.24}$$

Integrating Eq. 1.23 from $I = 0$ $(x = x_0)$ to $I(x)$ with constant σ_t yields the equation for the contrast ratio:

$$\frac{I_B - I}{I} = C_{ratio} = e^{-(\sigma_t \cdot x)}. \tag{1.25}$$

When $C_{ratio} = 0.02$ at a wavelength of 0.55 μm, the resulting distance x is the meteorological range, also called the *Koschmieder equation*:

$$x = \frac{3.912}{\sigma_t}. \tag{1.26}$$

Equation 1.26 relates a theoretical quantity, the meteorological range, to a measured extinction coefficient, which is commonly expressed in km^{-1}. In polluted air, the only important gas-phase visible light attenuation processes are Rayleigh scattering and absorption by nitrogen dioxide [8]. Several studies have found that scattering by particles, particularly those containing sulphate, organic carbon and nitrate, may cause 60-95% of visibility reduction and absorption by soot may cause 5-40% of visibility reduction in polluted air [8], [9], [10]. Table 1.4 shows meteorological ranges derived from extinction coefficients measurements for a polluted and a less polluted day in Los Angeles. Particle scattering dominates light extinction on both days. On the less polluted day, gas absorption, particle absorption and gas scattering all have similar small effects. On the polluted day the most important visibility reducing processes are particle scattering, particle absorption, gas absorption and gas scattering, in that order.

Table 1.4: *Meteorological Ranges (km) resulting from gas scattering, gas absorption, particle scattering, particle absorption, and all processes at a wavelength of 550 nm on a polluted and less polluted day in Los Angeles. From [11].*

	Meteorological Range (km)				
Day	Gas scattering	Gas absorption	Particle scattering	Particle absorption	All
Polluted (25/08/83)	366	130	9.6	49.7	7.4
Less polluted (07/04/83)	352	326	151	421	67.1

1.4.1 Gas absorption effects on visibility

In the solar spectrum, gas absorption primarily by nitrogen dioxide affects visibility. Table 1.5 gives extinction coefficients and meteorological ranges due to NO_2 absorption and Rayleigh scattering. For NO_2, values are shown at two mixing ratios, representing clean and polluted air respectively. On the contrary, for Rayleigh scattering, one value only is shown because Rayleigh scattering is dominated by molecular nitrogen and oxygen, whose mixing ratios do not change much between clean and polluted air. Table 1.5 shows that NO_2 absorbs much more strongly at shorter than at longer visible wavelengths. At low concentrations (0.01 ppmv) the effect of NO_2 absorption on visibility is less than that of gas scattering (Rayleigh scattering) at all wavelengths. At typical polluted-air concentrations (0.1-0.25 ppmv), NO_2 reduces visibility significantly for wavelengths < 0.50 μm and moderately for

Table 1.5: *Extinction coefficients ($\sigma_{a,g}$) and meteorological Ranges ($x_{a,g}$) due to NO_2 absorption at selected wavelength intervals ($l \pm 0.0005$ μm) and concentration. Absorption cross section data (b) for NO_2 are from Schneider et al. [12]. Also shown is the meteorological range due to Rayleigh scattering only ($x_{s,g}$). T= 298 K and p_a= 1 atm.*

		NO_2 absorption				Rayleigh scattering
		0.01 ppmv NO_2		0.1-0.25 ppmv NO_2		
λ (μm)	b (10^{-19} cm^2)	$\sigma_{a,g}$ (10^8 cm^{-1})	$x_{a,g}$ (km)	$\sigma_{a,g}$ (10^8 cm^{-1})	$x_{a,g}$ (km)	$x_{s,g}$ (km)
0.42	5.39	13.2	296	330	11.8	112
0.45	4.65	11.4	343	285	13.7	148
0.50	2.48	6.10	641	153	25.6	227
0.55	0.999	2.46	1590	61.5	63.6	334
0.60	0.292	0.72	5430	18.0	217	481
0.65	0.121	0.30	13000	7.5	520	664

wavelengths 0.5-0.6 μm. Most effects of NO_2 on visibility are limited to times when its concentration peaks.

Figure 1.11 shows extinction coefficients due to NO_2 and ozone absorption at different mixing ratios. The figure indicates that NO_2 affects extinction

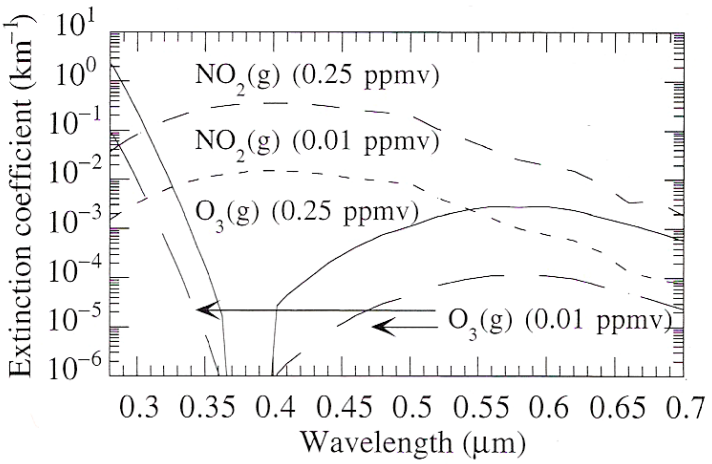

Figure 1.11: *Extinction coefficients due to NO_2 and O_3 absorption when T=298 K and p_a=1013 hPa.*

(and therefore visibility) primarily at high mixing ratios and at wavelengths

below about 0.5 μm. Ozone has a larger effect on extinction than does nitrogen dioxide at wavelengths below about 0.32 μm. Nevertheless the cumulative effect of ozone, NO_2 and other gases on extinction is small in comparison with effects of scattering and absorption by particles.

Chapter 2

Multiple AXis Differential Optical Absorption Spectroscopy (MAX-DOAS)

Multiple AXis Differential Optical Absorption Spectroscopy (MAX-DOAS) in the atmosphere is a novel measurement technique that represents a significant advance on the well-established zenith looking DOAS. MAX-DOAS utilizes scattered sunlight received simultaneously (or in a very short time period) from multiple viewing directions. Ground-based MAX-DOAS is highly sensitive to absorbers in the lowest few kilometers of the atmosphere and vertical profile information can be retrieved by combining the measurements with Radiative Transfer Model (RTM) calculations and inversion techniques.

2.1 The absorption spectroscopy for atmospheric measurements

The analysis of the atmospheric composition by scattered sunlight absorption spectroscopy has a long tradition. This application is also called "passive" absorption spectroscopy in contrast to spectroscopy using artificial light sources (e.g., active DOAS, see [13]).

Shortly after Dobson and Harrison [14] conducted measurements of atmospheric ozone by passive absorption spectroscopy, the "Umkehr" technique [15], which was based on the observation of a few (typically 4) wavelengths, allowed the retrieval of ozone concentrations in several atmospheric layers yielding the first vertical profiles of ozone.

The COSPEC (COrrelation SPECtrometer) technique developed in the

late 1960s was the first attempt to study tropospheric species by analyzing scattered sunlight in a wider spectral range while making use of the detailed structure of the absorption bands with the help of an opto-mechanical correlator [16]. It has now been applied for over more than three decades for measurements of total emissions of SO_2 and NO_2 from various sources, e.g. industrial emissions [17] and volcanic plumes [18].

Scattered sunlight was later used in numerous studies of stratospheric and (in some cases) tropospheric NO_2 as well as other stratospheric species by ground-based Differential Optical Absorption Spectroscopy (DOAS). This was a significant step forward, since the quasi continuous wavelength sampling of DOAS instruments in typically hundreds of spectral channels allows the detection of much weaker absorption features and thus higher sensitivity. This is due to the fact that the differential absorption pattern of the trace gas cross section is unique for each absorber and its amplitude can be readily determined by a fitting procedure using for example least squares methods to separate the contributions of the individual absorbers. The simultaneous measurement of several absorbers is possible while cross-interferences and the influence of Mie scattering are virtually eliminated.

Scattered sunlight DOAS measurements yield the *slant column density* of the respective absorbers, that is, the trace gas concentration integrated along the light path. Most observations were done with zenith (vertical) looking instruments because the radiative transfer modelling necessary for the determination of *vertical column density* (the vertically integrated trace gas concentration) is best understood for zenith scattered sunlight. This configuration was particularly suitable for the measurement of stratospheric absorbers. On the other hand, for studies of trace species near the ground, artificial light sources were used in *active* DOAS experiments (see e.g. [19] and references therein). These active DOAS measurements yield trace gas concentrations averaged along the several kilometer long light path, extending from a searchlight type light source to the spectrometer. Active DOAS instruments have the advantage of allowing measurements to be made independent of daylight and at wavelengths below 300 nm; however, they require a much more sophisticated optical system, more maintenance, and one to two orders of magnitude more power than passive instruments [19]. Therefore a type of instrument allowing measurements of trace gases near the ground like active DOAS, while retaining the simplicity and self-sufficiency of a passive DOAS instrument, is highly desirable.

Passive DOAS observations, essentially all using light scattered in the zenith, had already been performed for many years when the "Off-Axis" geometry (i.e., observation at directions other than towards the zenith) for measurements of scattered sunlight was first introduced by Sanders et al.

[20] to observe OClO over Antarctica during twilight. The strategy of their study was to observe OClO in the stratosphere using scattered sunlight as long into the "polar night" as possible. As the sun rises or sets, the sky is of course substantially brighter towards the horizon in the direction of the sun compared to the zenith. Thus the light intensity and therefore the signal to noise ratio is improved significantly. Sanders et al. also pointed out that the off-axis geometry increases the sensitivity for lower absorption layers. They concluded that absorption by tropospheric species (e.g. O_4) is greatly enhanced in the off-axis viewing mode, whereas for an absorber in the stratosphere the absorptions for zenith and off-axis geometries are comparable.
Arpaq et al. [21] used their off-axis observations during morning and evening twilight to derive information on stratospheric BrO at midlatitudes, including some altitude information from the change in the observed columns during twilight.
In spring 1995 Miller et al. [22] conducted off-axis measurements at Kangerlussuaq, Greenland, in order to study tropospheric BrO and OClO related to boundary layer ozone depletion after polar sunrise. These authors used off-axis directions of 87° and 85° (with respect to zenith) to obtain a larger signal due to the absorption by the tropospheric BrO fraction. The twilight behaviour of the slant columns was used to identify episodes of tropospheric BrO.
Off-axis DOAS was also employed for the measurement of stratospheric and tropospheric NO_3 by ground-based instruments [23], [24], [25].

Multiple AXis DOAS represents a new approach to the problem of measuring tropospheric species by observing their absorption in scattered sunlight. This technique combines the advantages of all preceding attempts and introduces several new concepts: combination of measurements at several off-axis viewing angles and multiple scattering radiative transfer modelling. It allows the study of atmospheric trace gases in the boundary layer with ground-based instruments with extreme sensitivity and some degree of spatial resolution. The approaches developed in inversion theory, in fact, can be applied to MAX-DOAS measurements to derive profile information.

A simplified scheme of the stratospheric and tropospheric absorption paths is shown in Fig. 2.1 for a zenith- and a multiple axis- looking spectrometer.

2.2 The DOAS technique

Differential Optical Absorption Spectroscopy is a technique that identifies and quantifies trace gas abundances with narrow band absorption structures

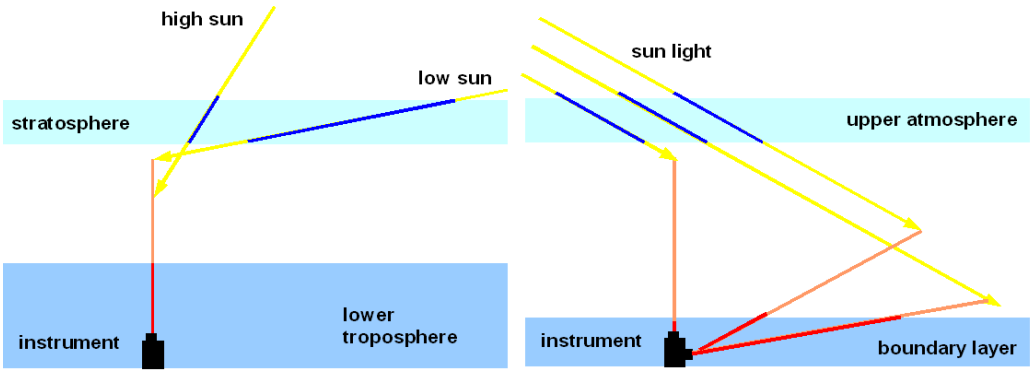

Figure 2.1: *Simplified scheme illustrating paths through the atmosphere of scattered solar radiation detected by a zenith looking (left) and a multiple axis (right) DOAS instrument.*

in the near UV and visible wavelength regions (from 0.25 to 0.75 μm) in the open atmosphere (e.g. [19] and references therein).

The basic idea of DOAS is to separate the trace gas absorption cross section into two parts, one that varies "slowly" with wavelength, and a rapidly varying differential cross section σ'. The latter can be thought of as absorption lines or bands. Broadband extinction by Mie scattering, instrumental effects and turbulence are difficult to quantify, therefore these interferences have to be corrected to derive trace gas concentrations. If the same filtering procedure is applied to the atmospheric absorption spectrum, the narrow band absorption can be used to calculate the trace gas concentrations (see [19]). The advantages of DOAS are the ability to detect extremely weak absorptions (optical depths $\sim 10^{-4}$), the unequivocal and absolute identification of the trace gases, as well as the fact that trace gas concentrations are determined solely from the absorption cross section. A calibration is therefore not necessary.

A DOAS detector device consists of a spectrograph with a telescope and a detector unit. The telescope is aimed into a given direction out of which it collects the light scattered into it; the light is usually transferred into the entrance slit of a spectrograph by use of one or multiple quartz fibres. The spectrograph's grating is adjusted to decompose light of wavelengths within a given wavelength interval (λ_1, λ_2). The light is imaged as a line or rectangle along the dispersion axis with the wavelength of the light changing from λ_1 to λ_2 from one end to the other. This image, the actual spectrum, is recorded with a detecting device and analyzed for trace gas absorptions.

Quantitatively the absorption of radiation at one specific λ is expressed

by the Beer-Bouguer-Lambert law (chapter 1, Eq. 1.9) with modified source intensity I'_0 and absorption cross section σ' to eliminate contributions that vary only slowly with wavelength:

$$I(\lambda) = I'_0(\lambda) \cdot e^{-(\sigma'(\lambda) \cdot SCD)}, \tag{2.1}$$

where SCD is the slant column density (μ in Eq. 1.9), which is readily seen to be:

$$SCD = \frac{\ln\left[\frac{I'_0(\lambda)}{I(\lambda)}\right]}{\sigma'(\lambda)}. \tag{2.2}$$

There are several aspects which are characteristic of scattered sunlight measured by passive DOAS instruments. Among them, the *Fraunhofer spectrum* and the *Ring effect* are briefly described in the following subsections.

2.2.1 The Fraunhofer reference spectrum

> *I found very many strong and weak vertical lines,*
> *which are darker than the remaining part of the spectrum.*
> *Some of them are almost dark.*
> Fraunhofer

The solar radiation can be described, in first approximation, as the continuous emission of a *blackbody*[1] with T≈ 5800 K, as shown in Fig. 2.2. This continuum, however, is overlaid by a large number of strong absorption lines called the *Fraunhofer lines*. These lines are due to selective absorption and re-emission of radiation by atoms in the solar photosphere. Many solar Fraunhofer lines are dominant in scattered sunlight, especially in the range (300-600) nm (see Fig. 2.3, left) and are substantially stronger than absorption due to most constituents of the terrestrial atmosphere. Fraunhofer lines have to be carefully removed in the DOAS analysis procedure in order to evaluate the absorption structures of the much weaker absorptions due to trace gases in the Earth's atmosphere (optical densities of 10^{-3} and less compared to Fraunhofer lines with up to 30% absorption at typical DOAS spectral resolution). A so-called Fraunhofer reference spectrum is so always included in the fitting process for the DOAS evaluation of scattered sunlight spectra [26].

[1] A blackbody is a hypothetical body comprising a sufficient number of molecules absorbing and emitting electromagnetic radiation in all parts of the electromagnetic spectrum so that (1) all incident radiation is completely absorbed (hence the term *black*), and (2) in all wavelength bands and in all directions the maximum possible emission is realized. The term *body* refers to a coherent mass of material which can be regarded as having uniform temperature and composition.

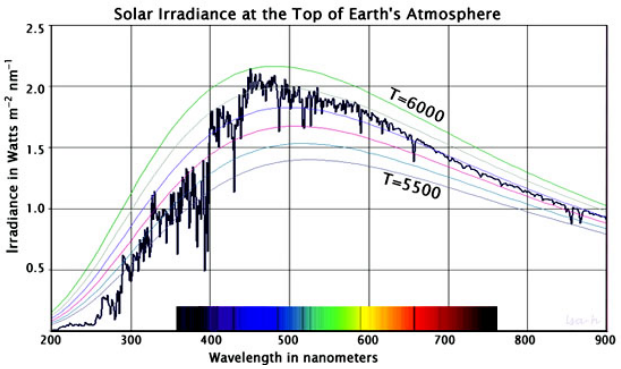

Figure 2.2: *Solar irradiance at the top of the atmosphere.*

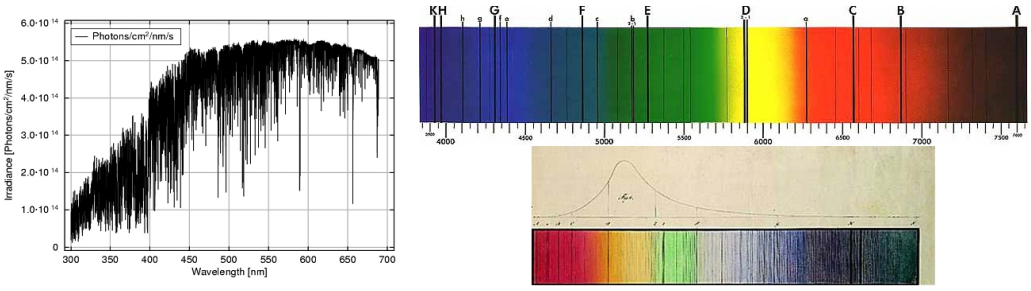

Figure 2.3: *(Left) Fraunhofer lines in the near UV/visible part of the solar spectrum. (Right) Fraunhofer lines (top) and a sketch of the solar spectrum coloured by Fraunhofer around 1814 (bottom).*

2.2.2 The Ring effect

The *Ring effect*, named after Grainger and Ring [27], leads to a reduction of the observed optical densities of solar Fraunhofer lines depending on the atmospheric light path. For example, Fraunhofer lines observed at large Solar Zenith Angles (SZAs) appear weaker than the same lines at small SZAs. Precise measurements can only be made if this effect is compensated for, otherwise complete removal of Fraunhofer lines by division of spectra taken at small and large SZA, respectively, is impossible.
Rotational Raman scattering is thought to be the most probable cause for the Ring effect, as illustrated in [28], [29]. In addition to elastic Rayleigh and Mie scattering, inelastic rotational Raman scattering on air molecules is also important in the atmosphere. Raman scattering moves energy from the incoming wavelength to neighbouring wavelengths and thus changes the spectral distribution in the scattered light. Raman scattering is non polarising,

isotropic, proportional to λ^{-4}, and responsible for about 4% of all Rayleigh scattered light.
Optical density changes due to the Ring effect are of the order of a few percent, which significantly affects DOAS measurements of scattered radiation. Thus a very accurate correction is required, since the atmospheric absorptions which are evaluated are sometimes more than an order of magnitude smaller than the filling in of the Fraunhofer lines. Therefore a so called Ring reference spectrum is included in the DOAS fitting process when scattered sunlight spectra are evaluated.

2.3 MAX-DOAS: the geometric approach

Stratospheric path length is a function of the Solar Zenith Angle, tropospheric path length is a function of the instrument Line Of Sight.

The calculation of path average trace gas concentrations from slant column density measurements using direct sunlight or active DOAS arrangements is straightforward. The ability to properly interpret UV/visible absorption measurements of atmospheric constituents using scattered light, on the contrary, depends crucially on how well the multiple paths of light collected by the system are understood. In other words, it is crucial to correctly describe the radiative transfer in the atmosphere [30].
DOAS measurements using scattered sunlight yield slant column densities, SCDs, which are defined as the trace gas concentration integrated along the effective light path (in reality it is an average of an infinite number of different light paths):

$$SCD = \int_0^L c(s) \cdot ds, \tag{2.3}$$

where L is the total path length. Since the SCD depends on the observation geometry and the current meteorological conditions, it is usually converted to the vertical column density, VCD. The vertical column density is a quantity not dependent e.g. on solar position or the instrumental line of sight, and is defined as the trace gas concentration, $c(z)$, integrated along the vertical path through the atmosphere:

$$VCD = \int_0^\infty c(z) \cdot dz. \tag{2.4}$$

The concept of Air Mass Factor (AMF) has been used for interpreting scattered light DOAS observations for many years (e.g. [31], [32]). The AMF

is the conversion factor to convert SCD into VCD and is defined as the ratio of slant column density and vertical column density:

$$AMF(\lambda, \theta, \alpha, \phi) = \frac{SCD(\lambda, \theta, \alpha, \phi)}{VCD}, \tag{2.5}$$

where λ denotes the wavelength of radiation, θ the solar zenith angle, α the elevation angle of the line of sight and ϕ the relative azimuth angle, which is defined as the azimuth angle between the telescope direction and the sun. For zenith sky measurements the relative azimuth is not relevant; however, for off-axis directions, it has to be taken into consideration. The elevation angle indicates the pointing of the telescope and is defined by the angle between the tangential plane of the Earth's surface and the direction of the telescope. Thus an elevation angle of 90° denotes zenith sky. From Eq. 2.5 it can be deduced that the diurnal cycle of the AMF follows that of the slant column density unless the total amount or vertical profile of the absorber changes in the course of the day.
The observation geometry and the respective angles for zenith and off-axis configurations in the **single scattering approximation** are shown in Fig. 2.4. For simplicity the relative azimuth angle ϕ is assumed to be 180° here. Taking a as the fraction of the total vertical trace gas column (VCD) residing below the scattering altitude, we obtain SCD (in the single scattering approximation sketched in Fig. 2.4):

$$SCD \approx [a \cdot \underbrace{\frac{1}{\sin\alpha}}_{AMF_{below}} + (1-a) \cdot \underbrace{\frac{1}{\cos\theta}}_{AMF_{above}}] \cdot VCD \qquad a \leq 1. \tag{2.6}$$

Therefore, in the single scattering approximation, a trace gas near the ground (e.g. in the planetary boundary layer) enhances the air mass factor according to approximately a $(1/\sin\alpha)$ relation, expressing the strong dependence of the AMF on the elevation angle α. In contrast, the air mass factor strongly depends on the solar zenith angle θ with approximately a $(1/\cos\theta)$ relation for an absorber in the higher atmosphere (e.g. in the stratosphere).

2.4 MAX-DOAS: the radiative transfer approach

As mentioned above, the geometric, single scattering approach using the equation $AMF \approx (1/\cos\theta)$ (for scattering below the trace gas layer), where θ is the solar zenith angle, or $AMF \approx (1/\sin\alpha)$ (for scattering above the

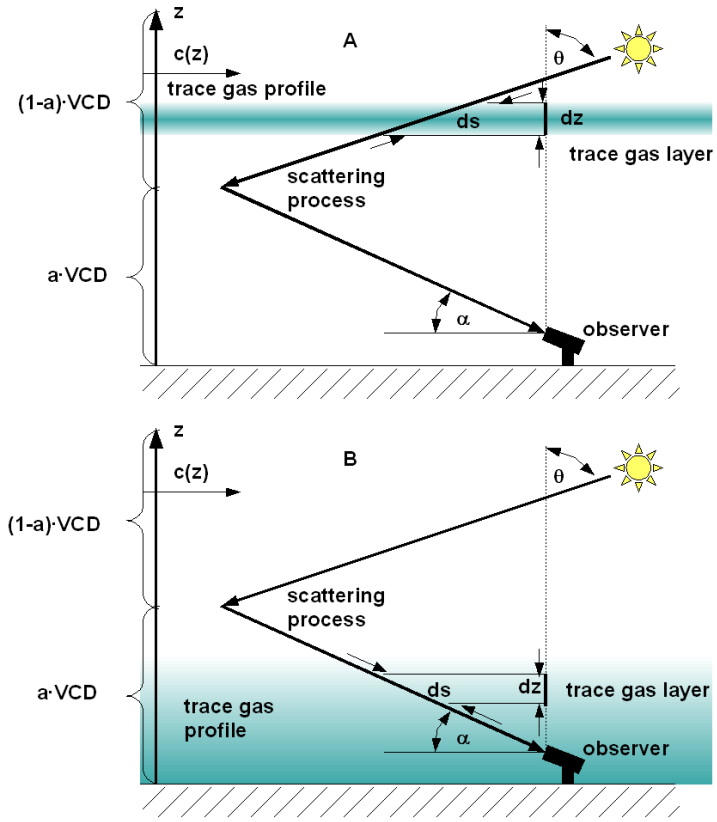

Figure 2.4: *Observation geometries for ground-based DOAS using scattered sunlight: Light enters the atmosphere at a certain solar zenith angle θ. In the single scattering approximation light received by the observer was scattered exactly once into the telescope viewing direction defined by the observation elevation angle α. The observed SCD (integral along ds) is larger than the VCD (integral along dz), with AMF being the conversion factor. Panel A represents the situation for a high (stratospheric) trace gas layer, panel B is representative for a trace gas layer near the surface.*

trace gas layer), where α is the telescope elevation angle, can only be regarded as an approximation. For zenith sky measurements a simple model that only takes single scattering of the light into account is able to illustrate the basic mechanisms. By means of the zenith sky slant column's diurnal cycle, for example, it can be qualitatively determined if a gas mainly absorbs in the troposphere or in the stratosphere. For large SZAs the photons cover a long and slant distance from the sun to the upper atmosphere before getting scattered in the zenith into the telescope. The most likely scattering height depends on the solar zenith angle and displaces rapidly upward with

the sinking sun. For a stratospheric absorber the slant column increases with increasing SZA as long as the scattering height lies initially below and then within the absorbing layer. If at very low sun the most likely scattering height is situated above the absorbing layer the slant column decreases in turn (see, for example, the SCDs of nitrogen dioxide depicted in Fig. 2.5 top right). A tropospheric trace gas, on the contrary, absorbs below the most likely scattering height along a relatively short light path which changes only slightly with the solar zenith angle; by consequence, also the slant column density changes only slightly with the solar zenith angle (see, for example, the SCD of formaldehyde (CHOH) depicted in Fig. 2.5 bottom right).
A graphical representation of what discussed above can be seen in Fig. 2.5, where the slant column densities of a stratospheric (nitrogen dioxide) and tropospheric (formaldehyde) trace gas and their variation with the solar zenith angle are shown. These slant column densities have been simulated

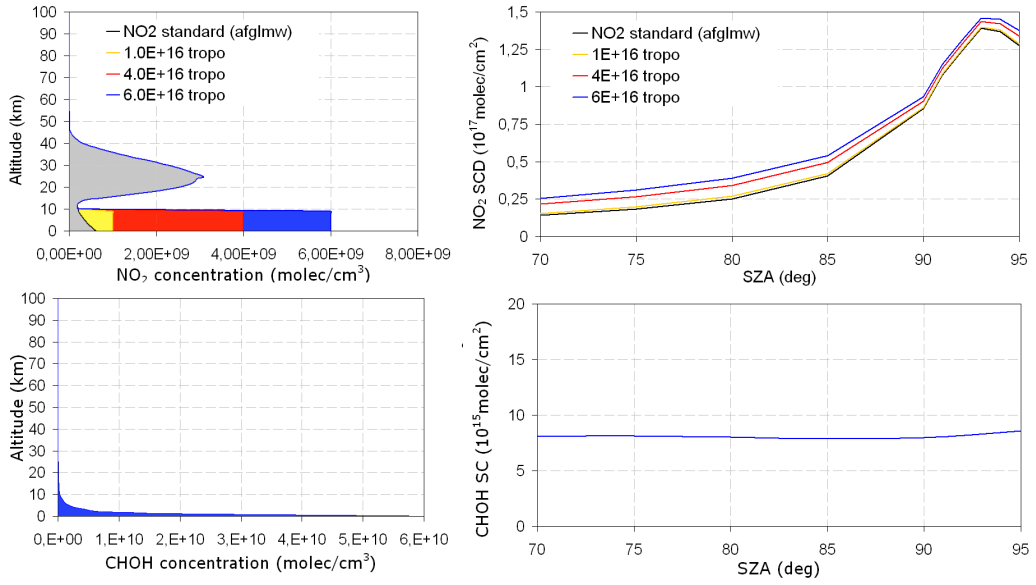

Figure 2.5: *Simulated slant column densities (right side) of nitrogen dioxide and formaldehyde for different input profiles (left side) and a zenith looking configuration (see text for details). The simulations have been carried out with the radiative transfer model PROMSAR.*

by the radiative transfer model PROMSAR (PROcessing of Multi-Scattered Atmospheric Radiation) [33], which will be accurately described in chapter 3. With regard to NO_2, in particular, four different input profiles have been used, which are depicted in the left side of Fig. 2.5, on the top: they are a

climatologic standard vertical profile ("afglmw" in the figure legend, which stands for "air force geophysics laboratory midlatitude winter" profile), and three profiles with a different tropospheric load which has been added to the standard profile. It can be noticed from Fig. 2.5 (top) that for larger tropospheric NO_2 contents we obtain larger slant column densities, as expected from the definition of slant column density.

Whereas the single scattering model is a good approximation for stratospheric absorbers, in the troposphere multiple scattering gains in importance. Since the ground-based MAX-DOAS measurements are especially sensitive to the tropospheric absorbers, and the light path for this geometry is enhanced in the lower atmosphere compared to zenith sky measurements, radiative transfer model calculations including not only multiple scattering, but also ground albedo, refraction bending and arbitrary distributions of trace gases, become necessary.

The results of a comparison exercise of radiative transfer models of various international research groups for the MAX-DOAS viewing geometry [34] are presented and summarized in section 2.4.1. Our model, the PROMSAR model, took part to this intercomparison exercise. Precise air mass factors (actually *box-air mass factors*, see section 2.4.1) were calculated by the various RTMs in order to demonstrate the sensitivity of MAX-DOAS towards various vertical trace gas profiles, the aerosol load, the instrumental line of sight, and the wavelength of radiation.

2.4.1 The intercomparison exercise for MAX-DOAS calculations

In June 2005, a workshop on radiative transfer modelling for the UV and visible spectral range was held at University of Heidelberg, Germany (web site http://satellite.iup.uni-heidelberg.de/index.php/RTM_Workshop/149/0/). The aim of this workshop was to conduct a comparison of nine state of the art RTMs from various international research groups.
These models use different approaches to solve the atmospheric radiative transfer equation; they also treat the spatial discretisation of the atmosphere and the Earth's sphericity in different ways or operate in plane parallel geometry. Most of the participating RTMs were developed for the simulation of remote sensing observations from various platforms (e.g. ground, aircraft, balloon, satellite), which is a fundamental prerequisite for the correct interpretation of these observations. In addition, these RTMs can also be applied to investigate the energy deposition of the solar radiation in the Earth's atmosphere, which is especially interesting for cloudy conditions. Current

state of the art RTMs simulate the Earth's sphericity, refraction and multiple scattering processes. Some models are capable of modelling polarization and three-dimensional scenes.

This comparison exercise had two main foci. First, to quantify the agreement and the differences between the models and give recommendations for future improvements. Second, to investigate the sensitivity of the MAX-DOAS technique for selected atmospheric scenarios and viewing geometries, with a particular focus on the influence of aerosols.
In the following sections, some of the exercises carried out during the intercomparison will be presented and the main results discussed. The full description of the comparison exercises can be found in [34].

Modelled quantities used for the comparison exercise

As primary output, RTMs yield the radiance obtained by a detector for a defined atmospheric scenario. For the interpretation of remote sensing measurements, however, the most important output is the Air Mass Factor, which yields a measure for the remote sensing measurements sensitivity to atmospheric trace gases (see, e.g., [31] and [32]). Besides the observation geometry and the atmospheric properties, the AMF depends in particular on the spatial distribution of the trace gas of interest (for many applications, it is sufficient to know the relative vertical concentration profile).
Within the intercomparison exerise, in addition to the calculation of AMFs, radiances were also simulated and compared by the participating models. The comparison of radiances is a very sensitive tool to test the correct performance of the RTMs, because it allows the identification of errors, which might not be detectable if only AMFs were compared (in the AMF calculation potential errors of the modelled radiances typically cancel each other). All modelled radiances in the comparison exercise were expressed as normalized radiances with respect to the solar irradiance (a definition of the radiometric quantities can be found in chapter 3, section 3.1).
In this comparison exercise, instead of AMFs for specific trace gas profiles, so called box-AMFs were calculated. Such box-AMFs characterize the ratio of the *partial* SCD to the *partial* VCD of an atmospheric layer with an assumed constant trace gas concentration. They can moreover be understood as a measure of the light path enhancement compared to a vertical path in a given height interval. In the case of weak absorption and a horizontally homogeneous atmosphere the box-AMF can be expressed as:

$$AMF_{Box} = \frac{\int_{Box} ds}{\int_{Box} dz} \tag{2.7}$$

with the actual light path s and the vertical path z. Box-AMFs modelled for different elevation angles therefore serve as a measure of the sensitivity of a particular viewing direction towards an absorber being present in a specific vertical box (or layer). Therefore, box-AMFs provide a criterion for determining the sensitivity of MAX-DOAS for different shapes of vertical profiles. The great advantage of calculating box-AMFs is that they can serve as an universal data base to calculate appropriate (total) AMFs for arbitrary species with different height profiles. Total AMFs can be easily calculated from the box-AMFs and the respective trace gas profile as the sum of the box-AMFs over the whole atmosphere weighted by the respective partial trace gas VCD_i:

$$AMF = \frac{\int_0^{TOA} AMF_i \cdot VCD_i}{\int_0^{TOA} VCD_i}. \tag{2.8}$$

In Eq. 2.8 AMF_i and VCD_i refer to the box-AMF and the partial VCD for layer i, respectively; within the layer the trace gas concentration is assumed to be constant. The sum is carried out over all layers i (from the surface to the top of the atmosphere, TOA). The vertical discretisation chosen for the calculation of the box-AMFs within this intercomparison exercise is shown in Table 2.1.

MAX-DOAS observations

As already pointed out, in contrast to the well established ground-based observations of zenith scattered sunlight, MAX-DOAS observations are directed into the illuminated atmosphere under various elevation angles. Since for a slant viewing geometry, the absorption paths through (and accordingly the AMFs for) the lower atmosphere can become rather large, MAX-DOAS observations are especially sensitive to tropospheric trace gases.
The simulation of the MAX-DOAS geometry exhibits a particular challenge for RTMs because of the extended light paths through the lowest atmospheric layers. For such slant lines of sight, the correct treatment of the Earth's sphericity can become important. Moreover, the optical depth with respect to Rayleigh and aerosol scattering can become very large and the correct implementation of multiple scattering becomes indispensable.

Description of the participating models

Nine models from eight international research groups took part in the comparison exercise. All models included multiple scattering schemes. Besides

Table 2.1: *Lower boundaries and vertical extensions of the atmospheric layers selected for the box-AMF calculation. Please note that above 1000 m the layers are thinner than the distances between the layers. If needed, box-AMFs for layers in between can be derived by interpolation.*

Atmospheric layer	Lower boundary (m)	Vertical extension (m)
1	ground	100
2	100	100
3	200	100
4	300	100
5	400	100
6	500	100
7	600	100
8	700	100
9	800	100
10	900	100
11	1000	100
12	1500	100
13	2000	100
14	3000	100
15	5000	100
16	10000	1000
17	20000	1000

the way they solve the radiative transfer equation, they also differ in their treatment of the Earth's curvature and refraction. The basic features of each model are summarized in Table 2.2. As for the PROMSAR model, a full description is given in chapter 3. For a description of the other models, see [34] and references therein.

Basic settings

In order to allow a meaningful interpretation of the RTM results, several basic properties were set to predefined values for all models.
For the temperature and pressure profiles the data from the U.S. Standard atmosphere were used [35]. The temperature was interpolated linearly to match the vertical discretisation of the individual models; for the pressure the logarithm was interpolated linearly.
The ozone cross section measured with the SCIAMACHY instrument [36] was used (see Table 2.3); all other atmospheric absorbers were ignored.
The exercise was carried out for five wavelengths covering regions of the UV

Table 2.2: *Overview on the intercomparison participating models and some important properties.*

Model/Institute	Type	Treatment of sphericity	Refraction
MODTRAN/Switzerland	discrete ordinate approach	Spherical	Yes
MCC++/Russia	Backward Monte Carlo	Spherical	Partly
MCARaTS/Japan	Forward Monte Carlo	plane-parallel for direct solar beam; spherical for the line of sight;plane parallel for the diffuse radiation	Yes
PROMSAR/Italy	Backward Monte Carlo	spherical	Yes
UVspec/DISORT/ Belgium	discrete ordinate approach	spherical for direct solar beam; plane parallel for multiple scattering plane parallel for integration along the line of sight	not applied
VECTOR/Canada	technique of successive orders of scattering	spherical for direct solar beam;plane parallel for multiple scattering;spherical for integration along the lineof sight	No
SCIATRAN/Bremen plane parallel	Discrete Ordinate Method	Plane parallel	not applied
SCIATRAN/Bremen spherical	Discrete Ordinate Method for multiple scattering (plane parallel); characteristics method for integration along the line of sight (spherical)	spherical for direct solar beam; pseudo-spherical for multiple scattering spherical for single scattering; spherical for integration along the line of sight	Yes
TRACY-II/Heidelberg	Backward Monte Carlo	spherical	Partly

and visible spectral range, where important trace gases show characteristic absorptions (see Table 2.3).
To minimize any complications due to different telescope apertures, the field of view was set to very small values (<0.1).
The RTM comparison was performed for five different aerosol scenarios including also a pure Rayleigh atmosphere, as indicated in Table 2.4.

Table 2.3: *Wavelengths and ozone cross sections used in the RTM comparison exercise. The data are taken from [36]. Also shown are trace gases, which are typically analysed at the respective wavelengths.*

Wavelength (nm)	310	360	440	477	577
O_3 cross section (cm^2)	$9.59 \cdot 10^{-20}$	$6.19 \cdot 10^{-23}$	$1.36 \cdot 10^{-22}$	$5.60 \cdot 10^{-22}$	$4.87 \cdot 10^{-21}$
Trace gases analyzed in this spectral range	SO_2	BrO HCHO O_4	NO_2 IO CHOCHO	O_4	O_4

For the investigation of the dependence of the model results on the viewing direction of the telescope, specific elevation angles were chosen as described in Table 2.5.

Table 2.4: *Aerosol properties for the different test cases (Case A1 represents a pure Rayleigh-atmosphere). The asymmetry parameter was assumed to be independent from wavelength.*

Case	Aerosol extinction (km^{-1})	Altitude range	Asymmetry parameter
A1	0	-	-
A2	0.5	0-2 km	0.68 (urban)
A3	0.1	0-1 km	0.68 (urban)
A4	0.5	0-2 km	0.75 (maritime)
A5	0.1	0-1 km	0.75 (maritime)

Table 2.5: *Overview of the solar zenith angles, the elevation and the relative azimuth angles of the telescope. Exercises were performed for specific combinations of these angles.*

Selected elevation angles (SZA=20°)	Selected relative azimuth angles (SZA=80°)
1°	0°
2°	30°
3°	60°
6°	90°
10°	120°
20°	150°
90°	180°

Basic test of the model properties (exercise 0)

The first step of the RTM comparison was to check basic model results for a simple viewing geometry. This check was performed to avoid any elementary mistakes, which would later complicate the interpretation of the results for the MAX-DOAS settings. Only Rayleigh scattering was allowed. The zenith viewing geometry was chosen and the solar zenith angle was set to 70°. This exercise was carried out for all five wavelengths (see Table 2.3).

In Fig. 2.6 the results for the vertical optical depth (with respect to Rayleigh scattering) and the normalized radiances (taking into account also ozone absorption) are shown. Figure 2.6 shows that the optical depth in-

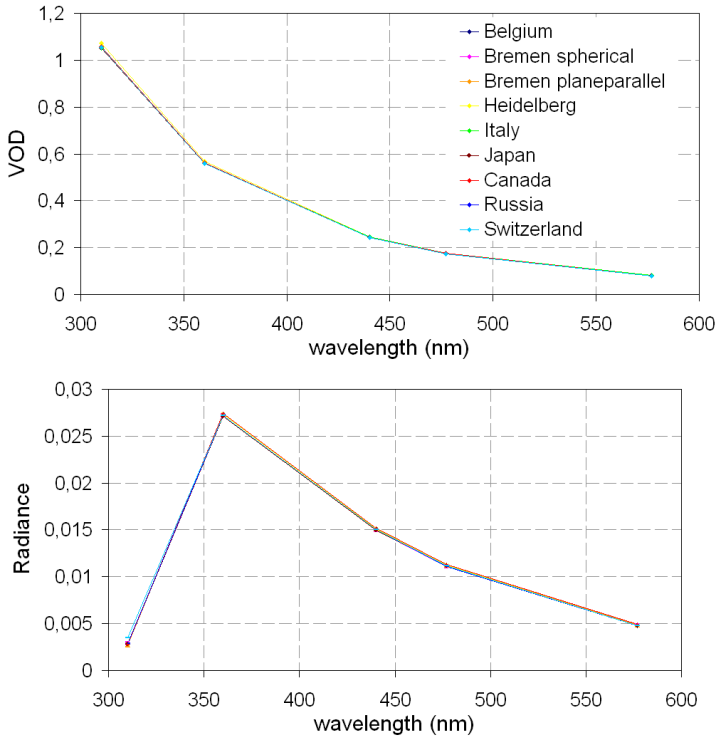

Figure 2.6: *Modelled vertical optical depth (VOD) with respect to Rayleigh scattering (top) and normalised radiance taking into account also ozone absorption (bottom), as a function of wavelength.*

creases with decreasing wavelength as expected for the strong wavelength dependence of Rayleigh scattering. Accordingly, the normalized radiances increase towards shorter wavelengths, but decrease again for the shortest wavelength (310 nm) because of the strong ozone absorption.

The results for the optical depth and normalized radiances are almost identical for all RTMs indicating that all models treat Rayleigh scattering consistently.

The Box-AMFs derived from all models for zenith viewing geometry and a solar zenith angle of 70° are displayed in Fig. 2.7. For atmospheric layers at

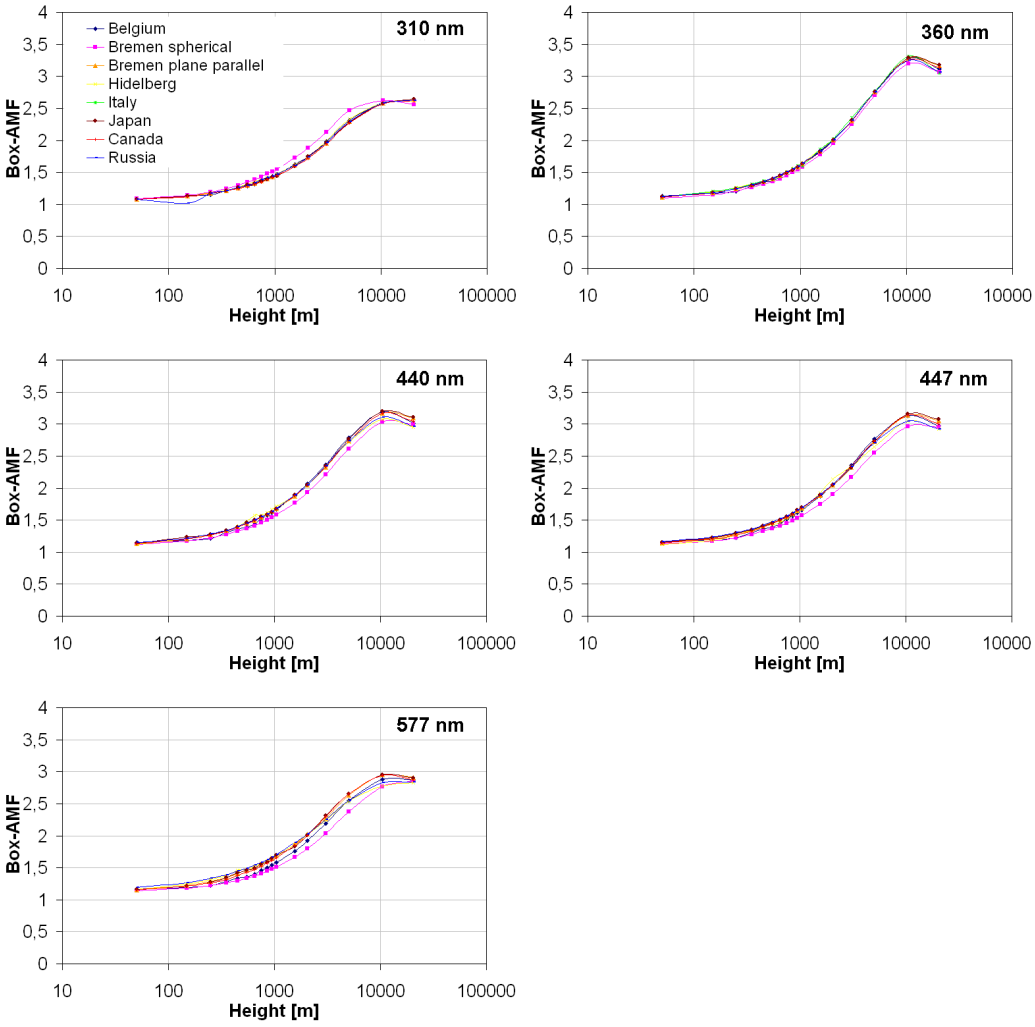

Figure 2.7: *Box-AMFs for zenith viewing geometry at a solar zenith angle of 70°. For low altitudes, the box-AMFs are about unity; for high altitudes about 1/cos(SZA)≈2.9. Please note that the altitude is displayed on a logarithmic scale.*

low altitudes, the box-AMFs are about unity, since the observed photons have traversed these layers almost exclusively on a vertical path. In contrast, the

direction of the photons for the highest layers is determined by the direct solar beam (almost all scattering events occur below). Thus, the box-AMF for these layers is similar to the geometrical approximation AMF=1/cos(SZA)∼ 2.9 (for SZA=70°). For some wavelengths and altitudes, also values greater than 2.9 are derived, indicating that multiple scattered photons enhance the geometrical light path. For the layers between the surface and 20 km, part of the photons are already scattered above, part are scattered below and the box-AMF is between unity and 2.9. It is interesting to note that at 310 nm even for the highest altitudes values less than 2.9 occur, indicating that a substantial fraction of the observed photons is scattered above 20 km.

From the test of the basic model parameters it was possible to conclude that all RTMs worked with similar prerequisites. The differences in the modelled optical depths and the normalized radiances were within only a few percent. Also the agreement of the modelled box-AMFs from the different models was good (within 5% or better) being the differences partly explained by the way in which Earth's sphericity is treated.

Variation of the elevation angle of the telescope (exercise 1)

The major characteristic of MAX-DOAS measurements is that the illuminated sky is observed under different elevation angles of the telescope. For low elevation angles (towards the horizon) the path length in the lowest part of the atmosphere is significantly longer than for higher elevation angles (towards the zenith). Accordingly, the sensitivity for the boundary layer increases with decreasing elevation angle. However, it must be noted that the sensitivity towards trace gases in the boundary layer is limited by the atmospheric visibility. In general, the visibility is decreasing towards smaller wavelengths because of the strong wavelength dependence of Rayleigh scattering. Moreover, especially for polluted situations, aerosol scattering further reduces the visibility (see also chapter 1, section 1.4); thus MAX-DOAS observations are very sensitive to the atmospheric aerosol load.
Within the exercise 1, aerosol scenarios A1 and A2 (see Table 2.4) were investigated. The calculations were performed for 7 elevation angles between 1° and 90° (see Table 2.5). The solar zenith angle was set to 20° and the relative azimuth angle to zero. The calculations were restricted to two wavelengths (360 nm, 577 nm) in order to minimize the computational effort.

Results for the box-AMFs are shown in Figs. 2.8 and 2.9 for the two wavelengths, respectively. As expected, the largest values are found for the smallest elevation angles and the lowest atmospheric layers. Especially for low extinction along the line of sight (in particular without aerosols, pure Rayleigh atmosphere or scenario A1) the box-AMFs for the lowest layers be-

come very large for 1° elevation angle (>40, the geometrical approximation for a plane parallel atmosphere would be $1/\sin(1°) \sim 57$). These strongly extended absorption paths cause the high sensitivity of MAX-DOAS observations for the boundary layer. For larger elevation angles, the box-AMFs for the lowest atmospheric layers decrease monotonously. For the highest atmospheric layers, the box-AMF converges towards the geometrical approximation for a solar zenith angle of 20° ($1/\cos(20°) \sim 1.06$). If no aerosols are present, the box-AMFs decrease systematically with increasing altitude, indicating that an increasing number of photons has been scattered below that altitude.
If aerosols are present, two major changes can be observed. First, the box-AMFs for the lowest atmospheric layers become systematically smaller (this makes MAX-DOAS observations particularly sensitive to aerosol properties). Second, multiple scattering on aerosols can cause an enhancement of the box-AMFs for atmospheric layers in and directly above the aerosol layer (0-2 km); consequently, the box-AMFs for these layers are slightly enhanced (compared to the layers above). This effect can be best observed for high elevation angles, particularly for zenith direction, for which the highest box-AMFs are found for altitudes between 1 km and 5 km (Figs. 2.8 and 2.9, bottom, right).

In general, again very good agreement (differences <5%) was found for most of the cases. Systematic differences occurred for the exercise for a pure Rayleigh atmosphere and 577 nm. For these cases, the path length along the line of sight becomes very long and thus the influence of the Earth's sphericity becomes especially important. The line of sight of the models using plane parallel geometry stays closer at the surface for larger distances from the instrument, causing systematically larger box-AMFs for low elevation angles.

Variation of the azimuth angle (exercise 2)

The relative azimuth angle between the direction of the telescope and the sun has an important influence on the amount of observed photons which are only scattered once (to a lesser degree also on photons which are scattered only a few times). The probability of these photons to be scattered into the telescope is directly proportional to the phase function of the scattering process. For Rayleigh scattering the phase function has a symmetric maximum in forward and backward direction causing a maximum in the observed normalized radiance for relative azimuth angles of 0° and 180°; for a relative azimuth angle of 90° (and 270°) a minimum occurs (see chapter 1, section 1.3.1 and chapter 3, section 3.3.2). For scattering on aerosols, the phase function typically has a pronounced maximum in forward direction (see chapter 1, section 1.3.2 and chapter 3, section 3.3.2). Thus, the observed normalized

radiance for a relative azimuth angle of 0° is much larger than for 180°.

In contrast to the single scattered photons (or those with only few scattering events), the contribution of multiple scattered photons depends only weakly on the relative azimuth angle. Thus, the strength of the azimuth dependence of the normalized radiance (and also of the box-AMF) decreases for an increasing fraction of multiple scattered photons (for example, inside a dense cloud, the normalized radiance does not depend on the viewing direction anymore).

In this exercise, box-AMFs were modelled for 7 relative azimuth angles (0°, 30°, 60°, 90°, 120°, 150°, 180°). The elevation angle was set to 2° and the solar zenith angle was set to 80° ensuring that the different relative azimuth angles relate to a representative range of the scattering phase functions for single scattered photons. The model runs were performed for a pure Rayleigh atmosphere and for two aerosol scenarios (see Table 2.4).
Figure 2.10 shows the box-AMFs for 360 nm as a function of altitude. The different graphs show the results for different relative azimuth angles (0°, 90°, 180°) and aerosol scenarios (pure Rayleigh atmosphere and the aerosol scenario A2). It can be noticed that, for most cases, a similar dependence on altitude as for the first exercise is found. The highest box-AMFs (about $1/\cos(2°) \sim 28$) are found for the lowest atmospheric layers; with increasing altitude they decrease to values close to the geometrical approximation for a solar zenith angle of 80° ($1/\cos(80°) \sim 5.8$). For the aerosol scenario A2 (see Table 2.4), the box-AMFs show minimum values within the aerosol layer (0-2 km). This indicates that this layer is characterized by a high fraction of multiply scattered photons. The effective light paths of the diffuse radiation in these layers are smaller than the light paths in the layers below and above, which are determined by the slant line of sight and slant direct solar beam.
In summary, we can again state that good agreement (differences <5%) was found for most of the cases between the various RTMs.

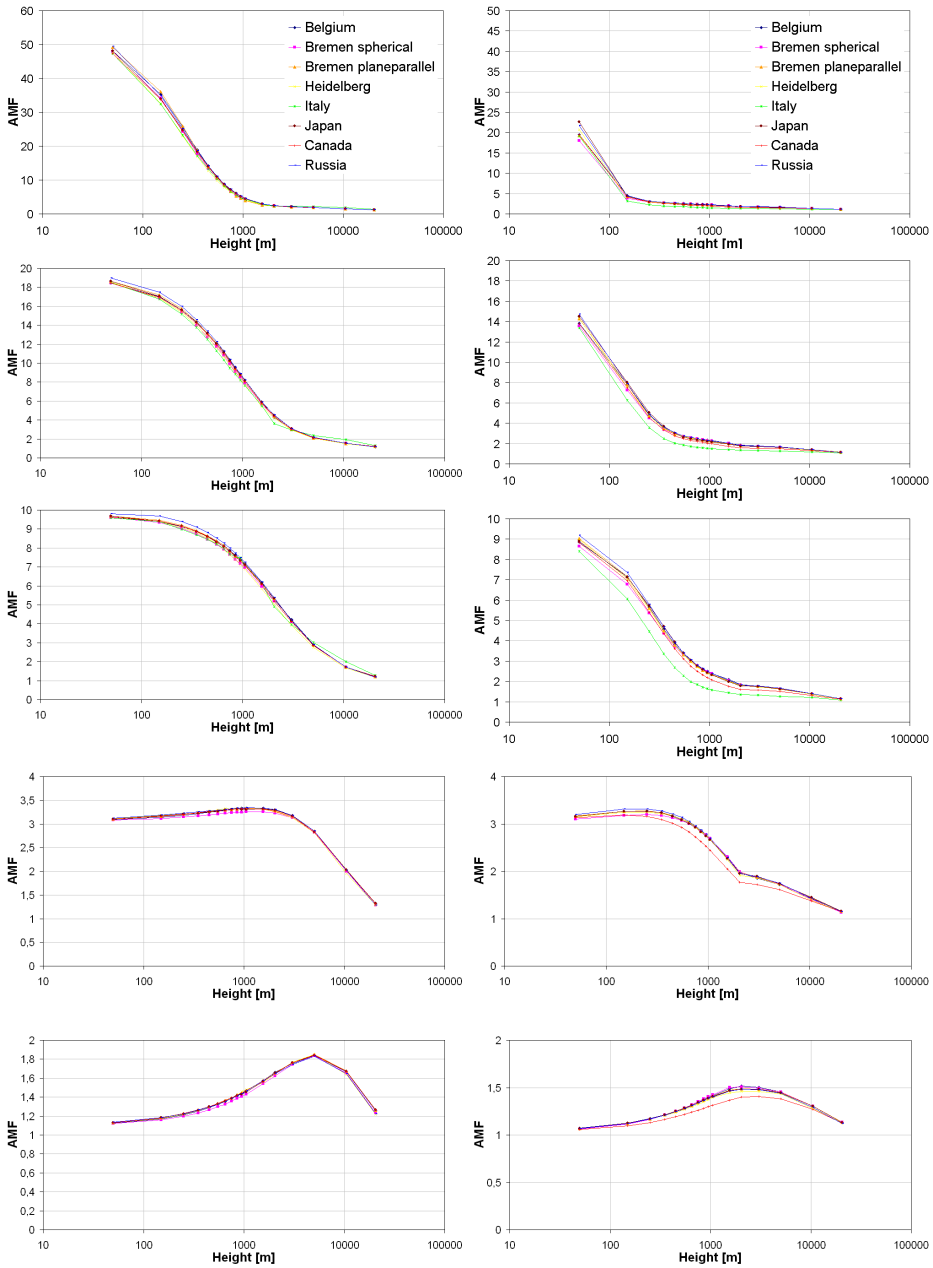

Figure 2.8: *Box-AMFs for 360 nm as a function of altitude (logarithmic scale). Left: pure Rayleigh atmosphere. Right: including also aerosol scattering (scenario A2, see Table 2.4). From top to bottom the elevation angle increases from 1° to 90°.*

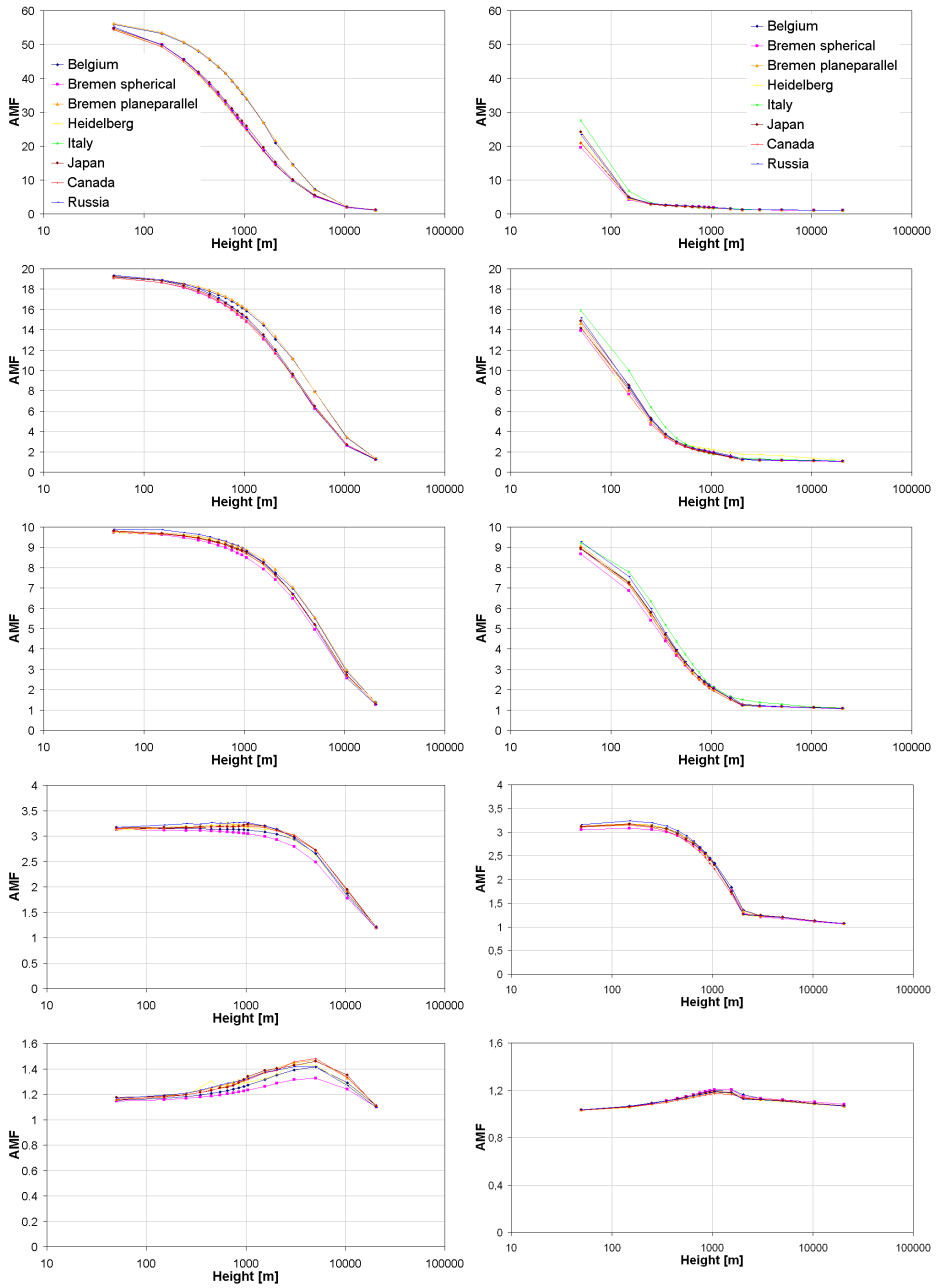

Figure 2.9: *Box-AMFs for 577 nm as a function of altitude (logarithmic scale). Left: pure Rayleigh atmosphere. Right: including also aerosol scattering (scenario A2, see Table 2.4). From top to bottom the elevation angle increases from 1° to 90°.*

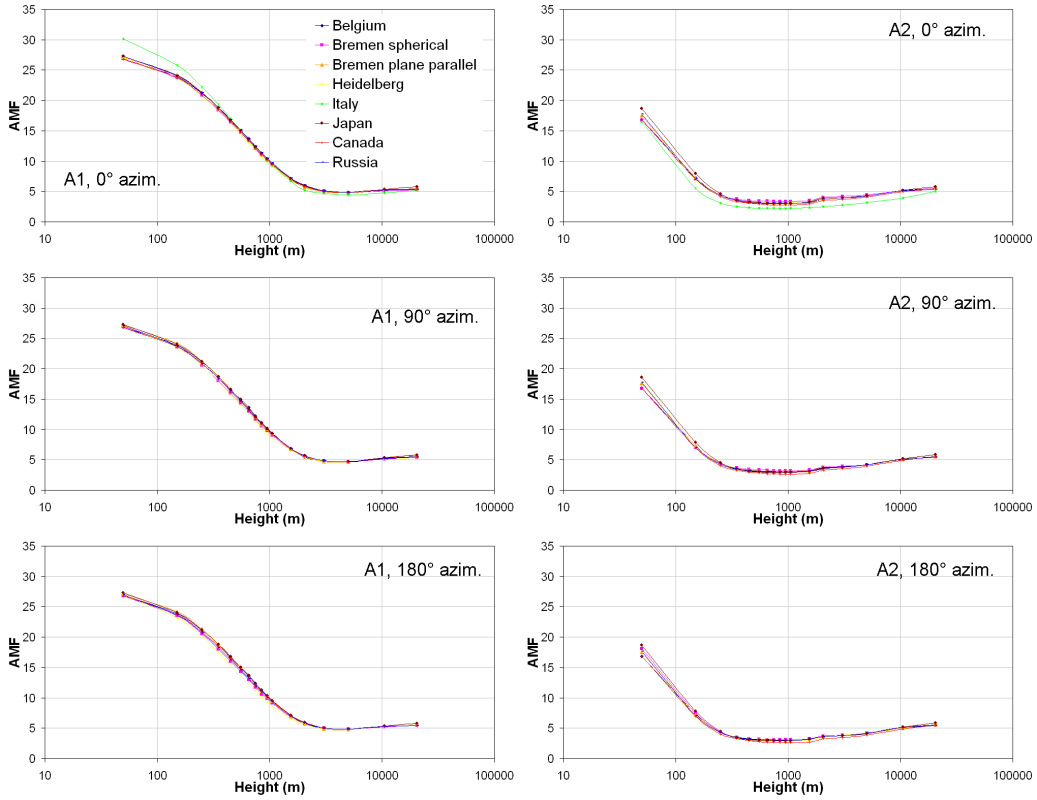

Figure 2.10: *Box-AMFs for 360 nm, an elevation angle of 2° and a SZA of 80° as a function of altitude (logarithmic scale) for different relative azimuth angles (top: 0°, middle: 90°, bottom: 180°). The calculation were performed for two different aerosol scenarios (left: no aerosol (scenario A1), right: scenario A2, see Table 2.4).*

Chapter 3

The Monte Carlo Radiative Transfer Model PROMSAR

Propagation of light in the atmosphere can be mathematically described by the Radiative Transfer Equation (RTE). Solutions to the RTE can be obtained both analytically (e.g., [37], [38]) and numerically (e.g. [39]).

The Monte Carlo (MC) method is a powerful numerical tool for performing radiative transfer simulations, even in complex geometries and with the advantage that it does not require extra simplifying assumptions compared with analytical methods.
There have been many examples of MC studies of radiative transfer in scattering and absorbing media, e.g. [40], [41], [42].
Monte Carlo methods are used extensively in problems involving optical propagation and atmospheric radiative transport, since the atmosphere is a non homogeneous medium with multiple scattering and polarization effects combining to make the problem extremely difficult for analytical treatment.

In this chapter, after introducing the radiometric quantities and the radiative transfer equation, the Monte Carlo radiative transfer model PROMSAR will be described in detail and applications to different cases discussed.

3.1 Radiometric quantities

Electromagnetic radiation may be viewed as an ensamble of waves which travel through a vacuum at the speed of light $c = 3 \times 10^8$ ms^{-1}. The waves may exhibit a continuous range of wavelengths, and the totality of all possible wavelengths is called the *electromagnetic spectrum*. Quantum theory predicts that energy transmitted by electromagnetic radiation exists in discrete units called *photons*. The amount of energy associated with a photon of radiation

is given by $h\nu$, where ν is the frequency of the radiation, expressed in s^{-1} and h is the Planck's constant, which is equal to 6.626×10^{-34} Js. The amount of energy contained in a photon of radiation is inversely proportional to the wavelength of radiation, according to the relationship $\nu = c/\lambda$.

The rate of energy transfer by electromagnetic radiation is called the *radiant flux*, which has units of energy per unit time: watts (W). For example, the radiant flux from the sun is about $3.90 \cdot 10^{26}$ W.
By dividing the radiant flux by the area through which it passes, we obtain the *irradiance, E*, which is expressed in units of Wm^{-2}. The averaged irradiance of solar radiation reaching the Earth's orbit is about 1370 Wm^{-2}, and is called *solar constant*. The irradiance per unit wavelength interval at wavelength λ is called the *monochromatic irradiance*, E_λ, which has units of $Wm^{-2}\mu m^{-1}$. With this definition, the irradiance is readily seen to be:

$$E = \int_0^\infty E_\lambda \cdot d\lambda. \tag{3.1}$$

Thus, if E_λ is plotted as a function of λ as in Fig. 3.1, the area under the curve between any two wavelengths is proportional to the contribution of the radiation in that wavelength band to the total irradiance. The irradiance

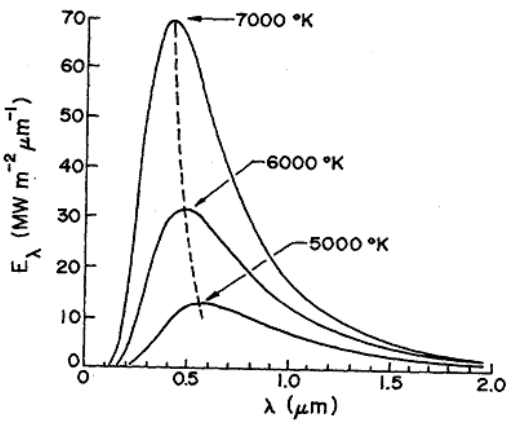

Figure 3.1: *Emission spectra for blackbodies with different temperatures. From [4].*

impinging onto the Earth's atmosphere can be measured using instruments located on high mountains, such as the Kitt Peak[1], or using satellite-mounted

[1]The Kitt Peak National Observatory (KPNO) is a United States astronomical observatory located on a 2.096 km peak of the Quinlan Mountains in the Arizona-Sonoran Desert on the Tohono O'odham Nation, 88 km southwest of Tucson. With 23 telescopes, it is the largest, most diverse gathering of astronomical instruments in the world.

sensors. An example for a spectrum measured with satellite-mounted sensors is the "Wehrli spectrum" [43], and is shown in Fig. 3.2.
If we want to identify the part of the irradiance that is coming from directions within some specified infinitesimal arc of solid angle $d\omega$, it is useful to define the *radiance, L*, which is the irradiance per unit solid angle, expressed in $\mathrm{Wm}^{-2}\mathrm{sr}^{-1}$. Given the radiance, the irradiance can be expressed as:

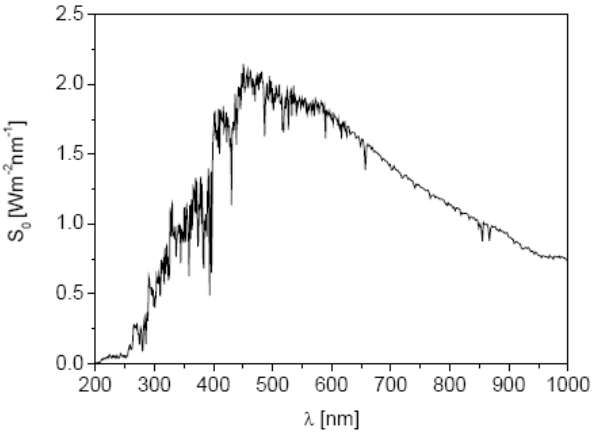

Figure 3.2: *The extraterrestrial solar irradiance by Wehrli [43].*

$$E = \int_0^{2\pi} L \cdot \cos\phi \cdot d\omega \tag{3.2}$$

where the zenith angle ϕ is the angle between the direction of the radiation and the normal to the surface in question. The quantity $L \cdot \cos\phi$ is therefore the component of the radiance normal to the surface. Equation 3.2 states that the irradiance represents the combined effects of the normal component of the radiation coming from the whole hemisphere. An element of the solid angle $d\omega$ can be expressed in spherical coordinates in the form

$$d\omega = \sin\phi \cdot d\phi \cdot d\theta, \tag{3.3}$$

where θ is the azimuth angle. The integral of $d\omega$ over the upper hemisphere is given by:

$$\int_0^{\frac{\pi}{2}} \sin\phi \cdot d\phi \int_0^{2\pi} d\theta = 2\pi, \tag{3.4}$$

which is readily seen to be equal to half the area of the sphere of unit radius. Using the definition of solid angle, Eq. 3.2 can be written in the form

$$E = \int_0^{2\pi} \int_0^{\frac{\pi}{2}} L \cdot \cos\phi \cdot \sin\phi \cdot d\phi \cdot d\theta. \tag{3.5}$$

3.2 Radiative transfer equation

The radiative transfer equation gives the change in radiance along a beam of electromagnetic energy at a point in the atmosphere. The processes affecting radiation along a beam are scattering of radiation out of the beam, absorption of radiation along the beam, multiple scattering of indirect, diffuse radiation into the beam, single scattering of direct, solar radiation into the beam, and emission of infrared radiation into the beam. *Single scattering* occurs when a photon of radiation is redirected into a beam after it collides with a particle or gas molecule, as shown in Fig. 3.3. *Multiple scattering* occurs when a photon enters a beam after colliding sequentially with several particles or gas molecules, each of which redirects the photon. Solar radiation that has not yet been scattered is *direct* radiation. Radiation, either solar or infrared, that has been scattered is *diffuse* radiation.

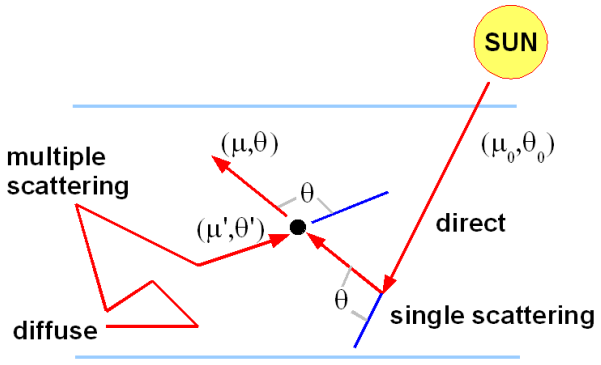

Figure 3.3: *Single scattering of direct solar radiation and multiple scattering of diffuse radiation adds to the intensity along a beam of orientation* (μ, θ)*. Adapted from [11].*

Assuming that the atmosphere can be represented by a horizontally stratified medium (plane-parallel approximation), the radiative transfer equation can be expressed by:

$$\mu \cdot \frac{dL_\lambda}{dz} = -k_\lambda(z) \cdot [L_\lambda(z;\mu,\theta) - J_\lambda(z;\mu,\theta)] \tag{3.6}$$

where $k_\lambda(z)$ is the extinction coefficient and $J_\lambda(z;\mu,\theta)$ is the source function at altitude z and for directions (μ,θ); μ is the cosine of the zenith angle and θ the azimuthal angle.
Ignoring radiative emission by the medium (a good approximation for wavelengths less than 4 μm, where radiation of solar origin dominates, as shown in Fig. 3.4), but considering scattering of light as well as absorption, the source function can be expressed by

$$J_\lambda = \frac{\Omega_\lambda(z)}{4\pi} \cdot \Big[\int_0^{2\pi} d\theta' \int_{-1}^{+1} p_\lambda(z;\mu,\theta;\mu',\theta') L_\lambda(z;\mu',\theta') d\mu' + \\ + p_\lambda(z;\mu,\theta;\mu_0,\theta_0)\Phi_\lambda(\infty)\exp(-\frac{1}{\mu_0}\int_z^\infty k_\lambda(z')dz')\Big] \tag{3.7}$$

where $\Omega_\lambda(z)$ is the albedo for single scattering defined by the ratio

$$\Omega = \frac{k_{s,\lambda}}{k_\lambda}, \tag{3.8}$$

where $k_{s,\lambda}$ and k_λ are the scattering and total extinction coefficient at wavelength λ. $p_\lambda(z;\mu,\theta;\mu',\theta')$ is the scattering phase function defining the probability that a photon originating from direction (μ',θ') be scattered in the direction (μ,θ). The direction (μ_0,θ_0) specifies the direction of the sun, and $\Phi_\lambda(\infty)$ is the solar irradiance at the top of the atmosphere. $p_\lambda(z;\mu,\theta;\mu_0,\theta_0)$ is the scattering phase function for direct radiation. Note that in Eq. 3.7 the first term accounts for multiple scattering, while the second term accounts for the scattering of the direct solar beam.

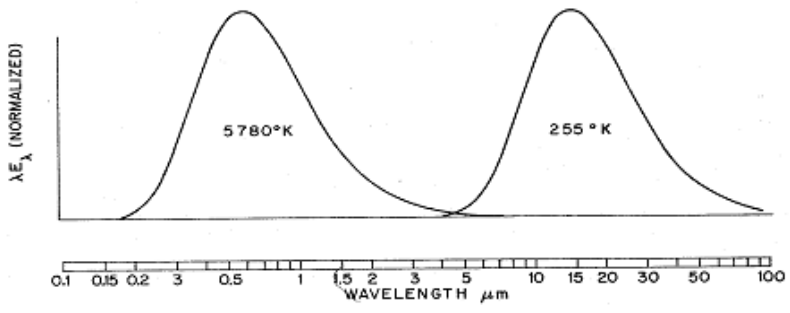

Figure 3.4: *Normalized blackbody spectra representative of the sun (left) and Earth (right), plotted on a logarithmic wavelength scale. The ordinate is multiplied by wavelength in order to make area under the curves proportional to irradiance. From [4].*

The solution of the radiative transfer equation requires that the phase function p_λ be represented by a mathematical expression. When scattering

is due only to air molecules, the phase function is provided by the Rayleigh theory. In other cases (e.g. when solid and liquid particles contribute to the scattering of light), the phase function can be derived from the Mie theory, if the physical and chemical characteristics of the particles are known. A detailed analysis of the Rayleigh and Mie phase functions will be given in section 3.3.2.
When particle scattering is included in the radiative transfer equation, analytical solutions become difficult to obtain and numerical solutions are needed. The Monte Carlo method is a powerful numerical tool for performing radiative transfer simulations including also multiple scattering with various phase functions involved. The Monte Carlo approach to the radiative transfer equation will be described in the following section.

3.2.1 The Monte Carlo approach to the RTE

> *The Monte Carlo method is defined as representing the solution of a problem as a parameter of a hypothetical population, and using a random sequence of numbers to construct a sample of the population, from which statistical estimates of the parameter can be obtained.*
> Halton, 1970 [44]

The Monte Carlo approach to atmospheric radiative transfer consists of using probabilistic concepts and methods to simulate the trajectories of each individual photon, which is subject to random events. Though the attenuation of a light beam obeys a well known exponential function, in fact, the collision of a single photon with a scattering center can happen at the very beginning or at the very end of a given distance to cover and, moreover, at the scattering site the photon can be scattered into any direction. These processes can be classified as random processes.

The basis of MC is that every interaction of a photon in the atmosphere can be described via a *Probability Density Function* (*pdf*), the integral of which (the *Cumulative Distribution Function*, *cdf*) can be linked to a random number, R. The probability for the photon to get scattered on its way to a given point is known. So a random number can be used to decide about this. At the scattering site, the photon can be scattered into any direction, the probability of a scattering being governed by the correspondent phase function. Here a random number can be used to decide which direction this individual photon gets scattered into. Once the probability of one event is known, it is possible to calculate the probability of a sequence of events as a

Markov chain[2], because the events are independent. By generating enough random realizations, the physical process (the radiation transport) can be simulated in a statistical sense.

The statistical basis

In this section we will define some basic statistical terms to lay a formal foundation for the validity of Monte Carlo calculations. At least in formal sense, all Monte Carlo calculations can be considered as the evaluation of a number of integrals of the type

$$\langle k \rangle = \int P(x)k(x)dx \tag{3.9}$$

where the random variable $k(x)$ is distributed according to the probability density function $P(x)$, and $\langle k \rangle$ specifies a certain numerical property of $k(x)$. Estimates of $\langle k \rangle$ can be obtained by sampling a great enough number of random variables x from $P(x)$ and averaging the correspondent $k(x)$ values. It is also convenient to consider the *variance* of k defined

$$var(k) \equiv \int P(x)(k(x) - \langle k \rangle)^2 dx = \int P(x)k^2(x)dx - \langle k \rangle^2. \tag{3.10}$$

In the Monte Carlo simulation of radiation transport, the random variable $k(x)$ specifies a unique track, the distribution function $P(x)$ gives the probability of occurrence of this particular track and the function $\langle k \rangle$ refers to a certain numerical property of the track (the *expectation*). The simulation of a track provides a random value x_i of x so that the value of $k(x_i)$ is obtained during the simulation of each track and accumulated in a counter. After generating a large number N of random tracks, Monte Carlo estimators of $\langle k \rangle$ and $var(k)$ are evaluated, respectively, as

$$\overline{k} = \frac{1}{N}\sum_{i=1}^{N} k(x_i) \tag{3.11}$$

and

$$s^2(k) = \frac{1}{N}\sum_{i=1}^{N} k^2(x_i) - [\frac{1}{N}\sum_{i=1}^{N} k(x_i)]^2. \tag{3.12}$$

[2]A Markov chain, named after Andrey Markov (1856-1922), is a discrete-time stochastic process with the property that, given the present state, future states are independent of the past states.

It is important to note here that the evaluation of $s^2(k)$ requires scoring of not only $k(x_i)$ but also the squared contributions $k^2(x_i)$.
Actually, a Monte Carlo simulation can be thought of as a "computer experiment" planned to measure $\langle k \rangle$, which yields the outcome $\overline{k}$. As in any real experiment, if we repeat it a number of times (with different seeds of the random number generator, to make the experiment "independent") we obtain different results. These fluctuate about the mean

$$\langle \overline{k} \rangle = \langle \frac{1}{N} \sum_{i=1}^{N} k(x_i) \rangle = \frac{1}{N} \sum_{i=1}^{N} \langle k \rangle = \langle k \rangle \tag{3.13}$$

with variance

$$s^2(\overline{k}) = var[\frac{1}{N} \sum_{i=1}^{N} k(x_i)] = \frac{1}{N^2} \sum_{i=1}^{N} var(k) = \frac{1}{N} var(k) \tag{3.14}$$

where use have been made of properties of the expectation and variance operators.
From the central limit theorem, it follows that, in the limit $N \to \infty$, the probability distribution of $\overline{k}$ is a normal (Gaussian) distribution. The quantity

$$s^2(\overline{k}) \equiv \frac{s^2(k)}{N} = \frac{1}{N} \{ \frac{1}{N} \sum_{i=1}^{N} k^2(x_i) - [\frac{1}{N} \sum_{i=1}^{N} k(x_i)]^2 \}. \tag{3.15}$$

in the limit $N \to \infty$, is an *unbiased estimator*[3] for $var(\overline{k})$. Simulation results should always be expressed in the form $\overline{k} \pm n \cdot s(\overline{k})$. With $n = 3$ the probability that the "true value" $\langle k \rangle$ lies within the error bar is approximately 0.997.

[3] An estimator, θ, can be defined as a useful approximation to a quantity of interest, Q, which may be derived from a Monte Carlo calculation. This means that θ is not expected to fluctuate far from Q. Formally,

$$\frac{\langle (\theta - Q)^2 \rangle}{Q^2} \ll 1. \tag{3.16}$$

Acceptable values of the ratio depend on the application. We write

$$\langle (\theta - Q)^2 \rangle = \langle (\theta - \langle \theta \rangle)^2 \rangle + (\langle \theta \rangle - Q)^2 \tag{3.17}$$

and observe that the quality of θ as a measure of Q comes separately from the variance of θ and from the departure of its mean from Q. The quantity $\langle \theta \rangle - Q$ is called the *bias* of the estimator. An *unbiased* estimator is one for which $\langle \theta \rangle = Q$, and the mean value of any experiment is just Q whatever the number N may be.

In practical calculations it may happen that, after a relatively long simulation time, the quantity of interest still has a large statistical uncertainty $s(\overline{k})$ that makes the numerical result meaningless. The quantity $var(\overline{k})$ is an intrinsic property of the function $k(x)$ and, for a sufficiently large number N of generated tracks, its estimator $s^2(k)$ is independent of N. Consequently, $s(\overline{k})$ is roughly proportional to $N^{-1/2}$, for large N. Thus, the obvious method to reduce the variance is simply to increase the number of generated tracks. However, as the simulation time is roughly proportional to N, in order to obtain a reduction of the statistical uncertainty by a factor of, say, 10 we must increase the computer time by a factor of 100. The aim of the so called *variance reducing techniques* (VRTs) is to yield results that are more accurate than those of the *analogue simulation*, without increasing the computation time. A practically oriented review of variance reducing methods in radiation transport has been given in [45].

Normally, variance reducing methods are based on transformations that, with the same calculation effort (computer time), reduce the variance of the quantity of interest to a fraction of its original value. These transformations usually involve additional calculations which consume some extra time and must be kept below reasonable limits. As a *figure of merit* to evaluate the effectiveness of a variance reducing method, it is common to use the efficiency ϵ, defined as

$$\epsilon = \frac{1}{s^2(\overline{k}) \cdot T \cdot} \tag{3.18}$$

where T is the computer time spent in the simulation. As $s^2(\overline{k})$ and T are proportional to N^{-1} and N respectively, ϵ is independent of N.

3.3 Description of the PROMSAR RTM

PROMSAR (PROcessing of Multi-Scattered Atmospheric Radiation) is a backward Monte Carlo model in which simulation of the radiative transfer in the atmosphere is performed according to the physical and geometrical data of an assigned atmospheric system.
Many experiments with independent radiation source and receiving optical device are allowed to be simulated by the PROMSAR code, including for example lidar experiment simulations which, however, will not be discussed in this thesis. The main computed quantities important for the study presented here refer to optical depths and transmittances of the atmosphere, direct and diffuse radiation contributions to the global radiation reaching the lowest boundary surface of a given environment, and radiance calculations

(including air mass factors for target species) for a detector with assigned central coordinates, diameter, direction cosines of the normal to the detector surface, line of sight and field of view. The detector can be placed at ground, as well as on board an aicraft or on satellite platforms.
The radiation source foreseen by the code is a monochromatic radiation in the ultraviolet-infrared range. Since the wavelength region of interest for DOAS applications is the UV/visible region, results reported in this thesis refer to this wavelength range.

3.3.1 Backward Monte Carlo technique

The strict Monte Carlo experiment is to "fire" photons out of a radiation source along initial directions governed by the aperture of that source. Then random numbers govern the entry of the photons into a model atmosphere, where they are scattered, by which scatterer, and in which direction. The photons direction is accordingly altered at each scattering location. In their random walk, eventually the photons will be absorbed, or either leave the atmosphere or reach the altitude where the modelled detector is located. There, the impact location and the incident angle are compared to the detector specifications. Each radiative transfer process can be modelled and reproduced with accuracy, and no approximations are needed. The absorption would be modelled by the destruction of the photon and the abort of the path calculation.
The problem in this is that the detector must reproduce realistic dimensions and aperture angle, i.e., the photon not only must reach the detector altitude, but must actually hit the detector, and do so from a solid angle defined by the line of sight and the aperture angle. This results in a very low total probability for one single photon to get "recorded" by the instrument.

An effective solution to this problem comes from the following considerations: the probability for a photon to leave the source (defined itself by its area and aperture angle) and reach a detector under the required conditions is the same as the probability that the photon leaves the detector on the way it entered it and reaches the source, i.e., follows backward the path it has in fact covered in forward direction. This is feasible, since any transmission probability (the probability that a photon covers the distance d from one given point to another) and any scattering probability (for a given scattering angle θ to occur) are the same in both directions. This approach is called "backward Monte Carlo".
Therefore, with the backward approach, each starting photon emerges from the detector in the line of sight direction and is traced backward since it leaves the atmosphere in the sun direction (or is absorbed). As demonstrated by

Collins [46], the backward Monte Carlo approach should be used to efficiently simulate narrow field of view instruments. It moreover eliminates a number of other problems involved in the forward Monte Carlo scheme (see also [47]).

3.3.2 The photon history tracking

> *A photon is emitted, it travels a distance, and then something happens to it.*

A unitary weight is assigned to each photon emerging from the point where the intensity (or radiance) is to be computed with a direction opposite to that in which the photon would phisically propagate. Changes in the photon weight during the simulation of its history is the signature of scattering, absorption and reflection contributions to the variation of the source intensity. Photon paths and interactions are simulated by sampling randomly from the various *pdf's* that determine the interaction lengths of each step in the random walk, scattering angles, and absorption rates.
For that purpose, the first step is sampling pseudo-random numbers[4] uniformly distributed in the interval [0,1]. As regard the random number generation, two algorithms are foreseen by the PROMSAR code: the first one generates the first random number of each history, while the second one, on the basis of this random number, generates the random numbers inside the history. In this way, corresponding histories in independent calculations begin with the same random number.
Second, the source parameters, photon paths and scattering angles are sampled according to the appropriate *pdf's*. To sample a quantity x_0 from a probability distribution function $P(x)$, which is normalized over all x, the following equation has to been solved:

$$R = \int_a^{x_0} P(x)dx = \psi(x_0) \tag{3.19}$$

where R is a random number sampled uniformly from the range 0 to 1, a is the lower limit of the range over which x is defined and ψ is the cumulative distribution function[5].

[4] pseudo-random numbers are generated according to a strict mathematical formula and therefore reproducible and not at all random in the mathematical sense but are supposed to be indistinguishable from a sequence generated truly random.

[5] For every real number x, the *cdf* of X is given by

$$x \longrightarrow F_X(x) = P(X \leq x), \tag{3.20}$$

where the right-hand side represents the probability that a random variable X takes on a

We need to sample how far a photon travels before being absorbed or scattered. The probability that a photon travels an optical path (OP) without an interaction is e^{-OP}. The probability of scattering prior to OP is $1 - e^{-OP} = \psi(OP)$. Therefore we can sample from the *cdf* according to

$$R = \int_0^{OP} e^{-x} dx \tag{3.21}$$

giving

$$OP = -\ln(1 - R) = -\ln(R) \tag{3.22}$$

where R is a random number sampled uniformly from the range 0 to 1.
To avoid the photon escaping the atmosphere without interaction with its components, we can force the photon to scatter at least once. The so called *forced collision technique* allows the physical system to be better explored by the travelling photon, by increasing the collision number. This technique is usefully used when, notwithstanding small optical thickness, collision events are of special interest in the simulation. At each point of emission/collision we calculate the optical depth to the edge of the atmospheric grid, D_{leak}. The uncolliding and colliding probabilities are $\exp(-D_{leak})$ and $[1-\exp(-D_{leak})]$, respectively, giving rise to the two corresponding particle weight fractions which separately contribute to the leakage and collision analytical estimates. The colliding fraction will remain in the system giving rise to a next collision point according to the distribution low (*truncated exponential distribution* [46]):

$$\frac{e^{-x}}{1 - e^{-D_{leak}}}. \tag{3.23}$$

Equation 3.21 becomes

$$R = \int_0^{OP} \frac{e^{-x}}{1 - e^{-D_{leak}}} dx \tag{3.24}$$

from which the following expression for the optical distance to collision is derived:

$$OP = -\ln[1 - R \cdot (1 - e^{-D_{leak}})]. \tag{3.25}$$

value less than or equal to x. The probability that X lies in the interval (a,b] is therefore $F_X(b) - F_X(a)$ if $a < b$.

where R is a random number sampled uniformly from the range 0 to 1. When the collision is forced to occur, the photon statistical weight before collision, w_{n-1}, is adjusted to remove the bias introduced by forcing the collision:

$$w_n = w_{n-1}[1 - e^{-D_{leak}}]. \tag{3.26}$$

Since the force collision technique is time consuming and can greatly and irregularly affect the particle weight, option is left to the user to force only the first collision (or first few collisions), the remaining ones being left to chance as usual, according to an analogue simulation.
Forced collisions are not allowed for those lines of flight hitting reflecting surfaces, in order not to prevent the photon from undergoing reflection. In this case, the distance to collision is sampled according to Eq. 3.22. If a reflection actually occurs, a Lambert refection law (i.e. cosine distribution along the normal to the surface) is considered. The photon weight is consequently decreased by the surface albedo coefficient. Absorbed radiation at the surface is analytically estimated by means of the same law.

At each collision point the photon's fate is determined by the probability that the photon is scattered or absorbed. The statistical weight of the "survived" photon is so multiplied to the so called *single scattering albedo*, defined as

$$\omega = \frac{sc}{ac + sc} \tag{3.27}$$

where ac and sc are the absorption and the scattering coefficients of the layer to which the scattering point belongs, respectively. The corresponding weight fraction absorbed

$$1 - \frac{sc}{ac + sc} \tag{3.28}$$

gives rise to the expected value of absorption at each collision point along the photon's path (*collision estimator* for absorption). In addition, an estimate of the absorption can also be done by means of the more effective *distance estimator*, i.e., through the computation of the product between the photon path length before collision and the absorption coefficient along that path.

Having sampled a random optical depth OP we may then calculate, on the basis of the total macroscopic cross section of the layer to which the point scattering belongs, the pysical distance L that the photon travels before undergoing interaction. The photon's position is then updated according to:

$$x = x + L\sin\theta\cos\phi, \quad y = y + L\sin\theta\sin\phi, \quad z = z + L\cos\theta \tag{3.29}$$

where θ and ϕ are, respectively, the scattering and azimuth angles of the motion direction before collision.

A random number R is then generated to decide the type of scattering event, i.e., molecular or aerosol scattering. The phase function of the respective scatterer is used to derive the new motion direction of the photon. As already introduced in section 3.2, the phase function, $f(\cos\theta)$, describes the angular distribution of scattered light. It has no physical dimension, and its integral over all directions is 1:

$$\int_0^{2\pi}\int_0^{\pi}\frac{f(\cos\theta)}{4\pi}d\theta d\phi = 1. \tag{3.30}$$

Rayleigh scattering

The angular distribution of scattered light by the air molecules and particles much smaller than the incident wavelength (see also chapter 1, section 1.3.1) is described by the Rayleigh scattering phase function

$$f(\cos\theta) = \frac{3}{16\pi}\cdot\frac{2}{(2+\delta)}\cdot[(1+\delta)+(1-\delta)\cdot\cos^2\theta] \tag{3.31}$$

where δ is the depolarization factor that gives the correction for the depolarization effect of scattering from anisotropic molecules. When δ goes to zero, that is, no depolarization or symmetric molecules, Eq. 3.31 reduces to

$$f(\cos\theta) = \frac{3}{16\pi}\cdot[1+\cos^2\theta] \tag{3.32}$$

which is a commonly used approximation for the Rayleigh phase function. A value of $\delta = 0.0295$ is generally used [48], so that Eq. 3.31 becomes:

$$f(\cos\theta) = 0.0605 + 0.05722\cos^2\theta. \tag{3.33}$$

A graphic representation of Eq. 3.33 is given in Fig. 3.5. The Rayleigh phase function is symmetric around $\cos\theta = 0$ ($\theta = 90°, \theta = 180°$) and its values vary within a very restricted range.

During the photon history tracking, the time needed for selecting the scattering angle θ should be reduced as much as possible. In case of Rayleigh scattering this can be successfully achieved carrying out random accesses to precomputed cosine probability tables. An example is given by Table 3.1. The first column contains $(n+1)$ c_i values $(0, 1/n, 2/n, 3/n, ..., 1)$ which can be obtained by dividing the range [0,1] into n intervals (in this case

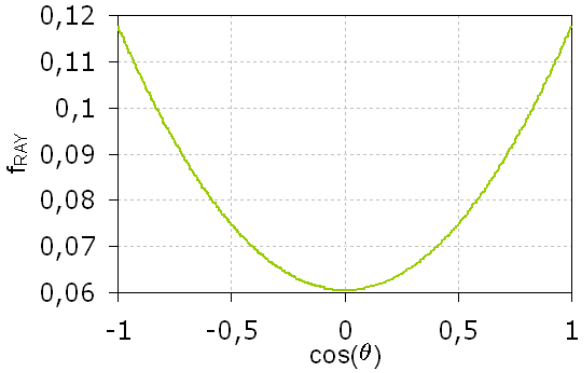

Figure 3.5: *Rayleigh phase function according to Eq. 3.33.*

$n = 32$); the second column contains $(n + 1)$ $\cos\theta_i$ values, in the range [-1,+1], corresponding to c_i values[6]. The advantage of using such a table is that, when a scattering event occurs during the photon history tracking, a random number c between [0,1] is sampled (which will be comprised in one of the intervals $[c_i, c_{i+1}]$) and the correspondent cosine angle $\cos\theta$ is quickly determined through simple linear interpolation between $\cos\theta_i$ and $\cos\theta_{i+1}$. In order to verify if the correspondence between c_i and $\cos\theta_i$ defined in Table 3.1 is correct, we reproduce the Rayleigh phase function by means of a Monte Carlo procedure and compare the numerical values obtained with the analytical ones[7]. The checking procedure is summarized in Fig. 3.6 and in Table 3.2. Figures 3.6 a) and b) show, respectively, the histogram with the number of counts per interval and the normalized histogram, that is, the Monte Carlo Rayleigh phase function. Figure 3.6 c) shows the numerical (MC) and analytical values of the Rayleigh phase function computed for the central point of each cosine interval. The values of the numerically- and analitically- computed Rayleigh phase function have been compared in Table 3.2.

[6]In order to build such a table we consider a great number M of cosine values and calculate the respective *cdf's* so as to define a correspondence between a value in the range [-1,+1] (the cosine) and a value in the range [0,1] (the *cdf*). Taking into account that each c_i value in Table 3.1 falls into one of the M intervals $[cdf_m, cdf_{m+1}]$, the correspondent $\cos\theta_i$ value in Table 3.1 is easily computed by linear interpolation.

[7]The MC procedure starts dividing the cosine range [-1,+1] in an arbitrary number m of interval, e.g. 16 intervals. Each $\cos\theta_i$ value of Table 3.1 falls into one of these m intervals. If a high number of $\cos\theta_i$ values is generated (e.g. 10^6), the normalized number of counts into each m^{th} interval supplies a numerical estimate of the Rayleigh phase function.

Table 3.1: *Cosine probability table for Rayleigh scattering.*

c_i	$\cos\theta_i$
0	-1
0.03125	-0.9569
0.0625	-0.9119
0.09375	-0.8648
0.125	-0.8155
0.15625	-0.7638
0.1875	-0.7095
0.21875	-0.6524
0.25	-0.5922
0.28125	-0.5289
0.3125	-0.4622
0.34375	-0.3921
0.375	-0.3187
0.40625	-0.2422
0.4375	-0.1631
0.46875	-0.0821
0.5	-0.0001
0.53125	0.082
0.5625	0.163
0.59375	0.2421
0.625	0.3186
0.65625	0.392
0.6875	0.4621
0.71875	0.5288
0.75	0.5922
0.78125	0.6523
0.8125	0.7095
0.84375	0.7638
0.875	0.8155
0.90625	0.8648
0.9375	0.9119
0.96875	0.9569
1	1

Mie scattering

As for the Mie phase function, it must be carefully taken into account in the simulation process the possible strong anisotropy of a scattering event according to the size parameter $2\pi r/\lambda$, where r is the particle radius and λ the wavelength of radiation (see also chapter 1), and the complex refraction index $n = m - iq$ (where $q = k_a\lambda/4\pi$, k_a being the absorption cross section). The strong anisotropy, in particular, prevents this phase function from be-

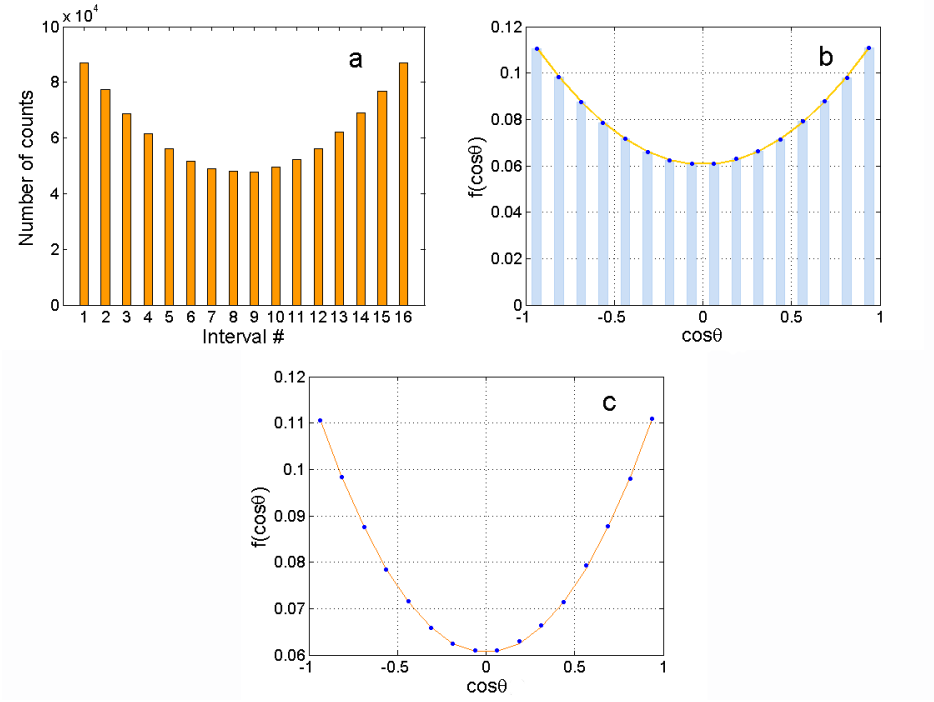

Figure 3.6: *a) The histogram showing the number of counts per interval (10^6 random samplings, 16 interval); b) the normalized histogram; c) comparison between the numerical values obtained for the Rayleigh phase function (blue circles) and the analytical values (orange line) computed for the central point of each cosine interval (see also Table 3.2).*

ing treated analytically. However, for spherical particles, we can obtain the following analytical expression from the Mie's theory:

$$f(r, \cos\theta) = \frac{\lambda^2}{8\pi^2 k_s(r)} \cdot (\mid S_1(\cos\theta) \mid^2 + \mid S_2(\cos\theta) \mid^2), \tag{3.34}$$

where S_1 and S_2 are the complex amplitude functions (describing the amplitude and phase of the scattered wave) for radiation scattered in directions perpendicular an parallel with the plane of scattering. For spherical particles, S_1 and S_2 depend only on the scattering angle θ (in general, $S = S(\theta, \varphi)$, where φ is the azimuth angle). $k_s(r)$ is the scattering cross section for the particle of radius r.
An approximation to the phase function for Mie scattering by aerosol particles is the *Henyey-Greenstein* (H-G) function [49]:

$$f(\cos\theta) = \frac{1}{4\pi} \cdot \frac{1 - g^2}{(1 + g^2 - 2g\cos\theta)^{3/2}}, \tag{3.35}$$

Table 3.2: *For the central point of each cosine interval, the numerical (Monte Carlo) and analytical values of the Rayleigh phase function, and their standard deviation are shown. See also Fig. 3.6 c.*

I	COS	ANALYTIC	MC	STD
1	-0.9375	0.111	0.111	7.20E-05
2	-0.8125	0.098	0.098	6.40E-05
3	-0.6875	0.088	0.087	5.67E-05
4	-0.5625	0.079	0.078	5.13E-05
5	-0.4375	0.071	0.072	4.68E-05
6	-0.3125	0.066	0.066	4.30E-05
7	-0.1875	0.062	0.062	4.09E-05
8	-0.0625	0.061	0.061	3.99E-05
9	0.0625	0.061	0.061	3.99E-05
10	0.1875	0.063	0.063	4.13E-05
11	0.3125	0.066	0.066	4.31E-05
12	0.4375	0.071	0.071	4.63E-05
13	0.5625	0.079	0.079	5.17E-05
14	0.6875	0.088	0.088	5.67E-05
15	0.8125	0.098	0.099	6.36E-05
16	0.9375	0.111	0.111	7.22E-05

where θ is the scattering angle and g is the asymmetry parameter. Eq. 3.35 is valid primarily for scattering that is not strongly peaked in the forward direction [50], and requires advance knowledge of the asymmetry parameter. The asymmetry parameter, or first moment of the phase function, is a parameter derived from the phase function itself that gives the relative direction of scattering by particles (or gases). Its analytical form is:

$$g = \int \int_{4\pi} f(\cos\theta) \cos\theta d\Omega. \tag{3.36}$$

The asymmetry parameter gives a measure of the asymmetry of the angular scattering. It approaches $+1$ for scattering strongly peaked in the forward direction and -1 for scattering strongly peaked in the backward direction. If $g = 0$, scattering is isotropic or symmetric (e.g. Rayleigh) type.

Properly tabulated aerosol phase functions or, alternatively, g values as a function of the scattering angle are achieved and processed by the PROMSAR code[8]. Through integration, from the tabulated phase function (or g) values the cumulative density functions can be obtained, each one relative

[8]One possibility, not the only one, is to use the standard aerosol phase functions or the g values stored in the MODTRAN (MODerate resolution TRANsmittance) code [48], [51].

to a scattering angle. During the photon history tracking, when an aerosol scattering occurs, the *cdf* can be compared to a random number to decide for the corresponding scattering angle. On the analogy of Fig. 3.6 and Table 3.2, Fig. 3.7 and Table 3.3 summarize the comparison between one possible aerosol phase function (representative of an urban extinction at 440 nm) and its MC estimate.

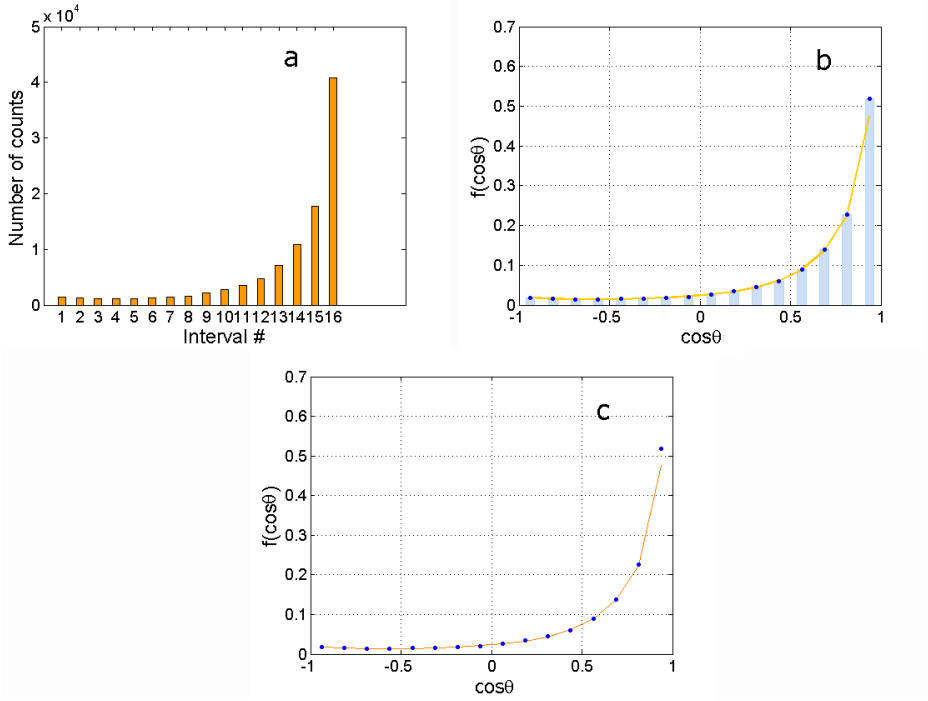

Figure 3.7: *a)The histogram showing the number of counts per interval (10^6 random samplings, 16 interval); b) the normalized histogram; c) comparison between the numerical values obtained for the Mie phase function (blue circles) and the analytical values (orange line) computed for the central point of each cosine interval (see also Table 3.3).*

Air mass factor calculation

At each collision point, the contribution to the intensity given by the i^{th} scattering of the solar radiation by the n^{th} photon and collected by the telescope is given by

$$Int_n^i = S \cdot w_n^i \cdot e^{-OD_{Sun}} \cdot p(\theta_{Sun}). \tag{3.37}$$

Table 3.3: *For the central point of each cosine interval, the numerical (Monte Carlo) and analytical values of the Mie phase function, and their standard deviation are shown. See also Fig. 3.7 c.*

I	COS	ANALYTIC	MC	STD
1	-0.9375	0.018	0.019	3.44E-05
2	-0.8125	0.016	0.016	3.19E-05
3	-0.6875	0.014	0.014	2.97E-05
4	-0.5625	0.014	0.014	3.08E-05
5	-0.4375	0.015	0.015	3.10E-05
6	-0.3125	0.016	0.017	3.41E-05
7	-0.1875	0.018	0.018	3.62E-05
8	-0.0625	0.021	0.020	3.72E-05
9	0.0625	0.026	0.027	4.12E-05
10	0.1875	0.033	0.034	5.00E-05
11	0.3125	0.044	0.045	5.79E-05
12	0.4375	0.061	0.060	6.32E-05
13	0.5625	0.089	0.090	7.83E-05
14	0.6875	0.137	0.138	1.00E-04
15	0.8125	0.224	0.227	1.33E-04
16	0.9375	0.475	0.519	2.12E-04

OD_{Sun} is the optical depth measured from the current position of the photon to the upper boundary of the medium in the direction of propagation of the incident flux, S is equal to the incident intensity, w_n^i is the weight attached to the n^{th} photon after the i^{th} scattering. $p(\theta_{Sun})$ is the phase function, which represents the probability density function for scattering of the photon in the direction antiparallel to that of solar rays, being θ_{Sun} the angle between the direction of incidence of the photon and the direction of the solar flux toward the top of the atmosphere. $e^{-OD_{Sun}}$ represents the probability that the photon propagates without undergoing any other collision from the current position to the point of incidence of the solar rays in the upper boundary of the atmosphere.

According to the air mass factor definition given in chapter 2 (Eq. 2.5), the ratio of the slant column density of an atmospheric absorber to its vertical column density has to be calculated. For this purpose the following computation steps must be performed in the PROMSAR code:

1. the radiances $I(\lambda, \sigma)$ and $I(\lambda, 0)$ are calculated. Two simulations are so performed: the first one where the absorber is included ($I(\lambda, \sigma)$) and the second one where the absorber is not included ($I(\lambda, 0)$);

2. the slant column density is calculated according to (see Eq. 2.2)

$$SCD = \frac{\ln\left[\frac{I(\lambda,0)}{I(\lambda,\sigma)}\right]}{\sigma}. \tag{3.38}$$

   Note that σ is the absorption cross section used as input parameter for the modelling of $I(\lambda, \sigma)$ in step 1;

3. the vertical column density is calculated by integrating the number density of the considered absorber in the vertical direction over the spatial extension of the model atmosphere;

4. the air mass factor is then derived according to Eq. 2.5

$$AMF = \frac{\ln\left[\frac{I(\lambda,0)}{I(\lambda,\sigma)}\right]}{\sigma \cdot VCD}. \tag{3.39}$$

In some cases, for the computation of the air mass factor, the *intensity-weighted approximation* can be used, which only needs one simulation to be run. This approximation only agrees with the more exact Eq. 3.39 in the limit of weak absorption, as explained in [52]. Assuming an infinitely narrow field of view and replacing the integration in Eq. 2.1 by a summation,

$$I(\lambda, \sigma) = \sum_z I_z(\lambda, 0) e^{-k_S(z)} \tag{3.40}$$

where $k_S(z)$ is the product σ (absorption cross section) and SCD, and

$$I(\lambda, 0) = \sum_z I_z(\lambda, 0). \tag{3.41}$$

Equation 3.39 then becomes:

$$AMF = \frac{1}{\sigma \cdot VCD} \cdot \{-\ln(\frac{\sum_z I_z(\lambda,0) e^{-k_S(z)}}{\sum_z I_z(\lambda,0)})\}. \tag{3.42}$$

If $k_S(z) \ll 1$, then $e^{-k_S(z)} \approx 1 - k_S(z)$. Hence

$$\begin{aligned} AMF &\approx \frac{1}{\sigma \cdot VCD} \cdot \{-\ln[\frac{\sum_z I_z(\lambda,0)(1-k_S(z))}{\sum_z I_z(\lambda,0)}]\} = \\ &= \frac{1}{\sigma \cdot VCD} \cdot \{-\ln[1 - \frac{\sum_z I_z(\lambda,0) \cdot k_S(z)}{\sum_z I_z(\lambda,0)}]\}. \end{aligned} \tag{3.43}$$

If $k_S(z) \ll 1$, then $\frac{\sum_z I_z(\lambda,0)\cdot k_S(z)}{\sum_z I_z(\lambda,0)} \ll 1$, and since $\ln(1+x) \approx x$ when $x \ll 1$

$$AMF \approx \frac{1}{\sigma \cdot VCD} \cdot \frac{\sum_z I_z(\lambda,0) \cdot k_S(z)}{\sum_z I_z(\lambda,0)}. \tag{3.44}$$

In the case of weak absorption, then $I_z(\lambda,\sigma) \approx I_z(\lambda,0)$ so that

$$AMF \approx \frac{1}{\sigma \cdot VCD} \cdot \frac{\sum_z I_z(\lambda,\sigma) \cdot k_S(z)}{\sum_z I_z(\lambda,\sigma)}. \tag{3.45}$$

This equation takes the weighted average of the AMFs of each ray in the calculation, the weights being set equal to the intensity received by the instrument for each ray.

End of history

After each collision, a new path length before the next interaction is generated. This process continues until the photon has undergone a fixed number of collisions or its weight is decreased below a preassigned threshold value (10^{-6} is generally used).

Besides using this criterion, other techniques can be used in the PROMSAR code to determine the photon end of history. In particular, expected values estimates are performed for absorption and leakage events.
As for absorption, at each collision point option is left to the user to perform an analog test on the survival probability when the photon weight falls below an assigned threshold weight, analytically evaluating the absorption contribution to the statistics. As for the leakage from the atmospheric system, the uncolliding probability for lines of flight hitting the upper boundary of the atmosphere is computed. The corresponding escaping weight fraction will give the contribution to the required estimate.

3.3.3 Input description of the PROMSAR code

PROMSAR requires as input a library which contains the characteristics of all components (both molecular and non-molecular) of the atmosphere. The physical properties, i.e., the vertical spatial distribution of the interaction (absorption and scattering) coefficients and of the refraction indices, and the phase functions (for non molecular scattering) must be specified for all the wavelengths of interest. For production of data sets containing the description of atmospheric environments, the MODTRAN code can be used (e.g. [48]), with its different aerosol, seasonal and latitude models. The MODTRAN code can furthermore be assumed as a reference to check the

PROMSAR correct acquiring and treatment of the library data, as it can be done, for instance, by comparing the optical vertical depths and the transmittance of the modelled atmosphere. The input library is the fundamental source of data for the PROMSAR code.

The features of the Monte Carlo calculation which has to be carried out are specified in a further input file, which contains: the number of photon histories to be processed, the variance reducing strategy (forced collision, analogue simulation), and the end of history criterion; the value of the source intensity and the solar source director cosines (or the solar source from astronomical parameters); the characteristics of the detector (altitude, line of sight, field of view); the albedo coefficient. Specific index values (1 or 0) allow to decide whether to take the refraction into account or not, or include/exclude aerosol particles or molecules in the calculation. It can moreover be decided for which molecules (among those included in the library) a special analysis (e.g., the computation of absorption rates or air mass factors) has to be carried out.

3.3.4 Variance reducing techniques

Batches of preassigned number of photon histories, each one representative of a single valuable numerical experiment, are processed in the PROMSAR model. Besides being more appropriate as regard the variance calculation, this procedure allows high number of histories (as it could be necessary) to be run without significantly precision loss when collecting the results coming from the simulation (10^5 photon histories can be run by processing, for instance, 100 batches each one of 1000 histories).
It should be noticed that, despite the variance is a function of the number of histories, N, its reduction can not be achieved simply increasing N, because this would increase the computational time. Instead, variance reducing techniques should be used.

To increase the efficiency of the MC calculations and optimize the statistical results, artificial devices are carried out during the history processing, so as to have more reliable estimators of the searched quantities than those naturally belonging to an analogue simulation. The final aim is to reduce the $V \cdot T$ product, where V is the variance of the calculation and T the running time required to obtain such a variance. Note that the $V \cdot T$ product is the inverse of the efficiency ϵ defined in Eq. 3.18.
In some situations of practical interest, a high variance can result from an extremely low interaction probability. The simplest and most effective variance reducing method consists of artificially increasing the interaction probability of the process of interest and consequently using appropriate weight factors.

An example of such a method is given by the forced collision technique introduced in section 3.3.2.

3.4 Sample applications of the PROMSAR code

The PROMSAR code has been primarily designed for the computation of the air mass factor, which is used for the interpretation of passive DOAS measurements. The AMF allows to convert the slant column density of an absorbing trace gas into its vertical column density, which does not depend on the geometry of measurement and the solar zenith angle and must be introduced if spectroscopic measurements under different viewing geometries are to be compared.
Examples of air mass factor computation for the MAX-DOAS technique have been discussed in chapter 2. In particular we have presented the results of an extensive intercomparison exercise between different RTMs in which the PROMSAR code took part, aimed at investigating the sensitivity of the MAX-DOAS technique for selected atmospheric scenarios and viewing geometries.

Besides calculating the AMF of a specific trace gas at a given wavelength, the PROMSAR code yields all the quantities that are generally computed by a radiative transfer model: (1) the vertical transmittance over the whole atmospheric system, (2) the transmittance belonging to the direction of the solar source, (3) the direct and global irradiance, and (4) the single- and multiple- scattered radiance measured by a detector with a specified position, line of sight and field of view, and for a defined atmospheric scenario. Sample calculations of the quantities listed above will be presented and discussed in the section 3.4.1. As a validation, we will also report comparisons with the same quantities computed by the MODTRAN code under the same atmospheric conditions and a comparison with experimental radiometer results.

3.4.1 Transmittance/irradiance/radiance calculations

If not differently specified, the following atmospheric model is assumed for the computations presented in this section:

- for the temperature, pressure and air density profiles, and for volume-mixing ratio of atmospheric constituent profiles the data from the “1976

U.S. Standard" atmosphere are used. This model is one of the six reference atmospheres provided by the MODTRAN code. The altitude increments are 1 km between 0 and 25 km, 2.5 km between 25 and 50 km, and 5 km between 50 and 100 km, having these increments been chosen for their compatibility with existing profiles in other radiation models. A comprehensive bibliography on reference atmospheric constituent profiles appears in Appendix B of the Anderson report [51];

- as for the aerosol scenario in the boundary layer, a "rural extinction" with visibility=23 km is used. Moreover, a "background stratospheric profile and extinction" is considered. These characteristics are specified in the MODTRAN code by the input parameters IHAZE (which defines the aerosol model used for the boundary layer and the surface meteorological range) and IVULCN (which is used to select both the profile and extinction type for the stratospheric aerosols and to determine transition profiles above the stratosphere up to 100 km), respectively. The aerosol models available in MODTRAN are described in [53];

- the wavelength of radiation is 0.440 μm

Transmittance

In chapter 1, section 1.2.1 we have defined the *optical depth* as a measure of the depletion that the beam of radiation undergoes as a result of its passage through a layer in the atmosphere. The *transmittance* or *transmissivity* is defined as

$$\tau_\lambda = e^{-OD_\lambda} \tag{3.46}$$

where OD_λ is the optical depth at wavelength λ.
The solar transmittance over the whole atmospheric system can be computed by the PROMSAR code, both in the vertical direction and in the direction of the monodirectional photon source. In this example we have assumed SZA= 30°, 60°, and 80°.
The total transmittance value, the contributions of molecules and aerosol particles and the transmittance belonging to the absorption of a special kind of molecule (ozone) are quoted in Table 3.4. Together with the PROMSAR calculations, also the values obtained by the MODTRAN code are shown resulting in a satisfactory agreement between the two models, as the percent errors indicate.

Table 3.4: *Transmittances comparison between MODTRAN and PROMSAR RTMs. Atmospheric scenario: 1976 U.S. Standard atmosphere; rural extinction and meteorological range of 23 km in the boundary layer; background stratospheric profile and extinction; λ = 0.440 μm.*

Vertical direction				
	Total	Aer. Tot.	Mol. Scat.	Ozone Abs.
MODTRAN	0.5090	0.6512	0.7849	0.9991
PROMSAR	0.5099	0.6523	0.7849	0.9991
Err. %	-0.2	-0.2	–	–
Source direction, SZA=30°				
	Total	Aer. Tot.	Mol. Scat.	Ozone Abs.
MODTRAN	0.4586	0.6094	0.7561	0.9990
PROMSAR	0.4595	0.6106	0.7561	0.9990
Err. %	-0.2	-0.2	–	–
Source direction, SZA=60°				
	Total	Aer. Tot.	Mol. Scat.	Ozone Abs.
MODTRAN	0.2597	0.4244	0.6169	0.9982
PROMSAR	0.2609	0.4261	0.6172	0.9982
Err. %	-0.5	-0.4	-0.1	–
Source direction, SZA=80°				
	Total	Aer. Tot.	Mol. Scat.	Ozone Abs.
MODTRAN	0.0219	0.0866	0.2585	0.9953
PROMSAR	0.0222	0.0876	0.2587	0.9954
Err. %	-1.4	-1.2	-0.1	-0.01

Irradiance

The direct solar irradiance has been computed with the PROMSAR code under the same conditions used in the previous calculation. Results have been compared to those obtained with the MODTRAN code, as indicated in Table 3.5, resulting in a very good agreement between the two models.

For the calculation of the solar irradiance, refraction must be taken into account. Refraction at a plane surface is described in terms of an approximate relation referred to as *Snell's law of refraction* that can be simply written as

$$\frac{\sin\theta_1}{\sin\theta_2} = \frac{n_2}{n_1} \tag{3.47}$$

where θ_1 and θ_2 are the angles of incidence and refraction, respectively, relative to the surface nomal, and n_1 and n_2 are the indices of refraction in medium 1 and medium 2, as indicated in Fig. 3.8. n_i can be expressed as the ratio of speed of light in a vacuum, $c = 3 \times 10^8$ ms^{-1}, to that in a given medium, c_i. Snell's law says that, when travelling from an optical thinner

Table 3.5: *Direct irradiance comparison between MODTRAN and PROMSAR RTMs. Atmospheric scenario: 1976 U.S. Standard atmosphere; rural extinction and meteorological range of 23 km in the boundary layer; background stratospheric profile and extinction; $\lambda = 0.440\ \mu m$.*

SZA	MODTRAN	PROMSAR	Err. %
30°	1.52E-06	1.52E-06	–
60°	8.60E-07	8.63E-07	-0.3
80°	7.26E-08	7.34E-08	-1

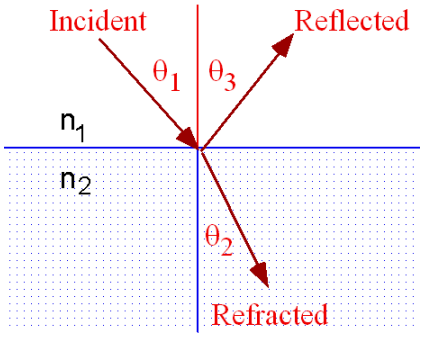

Figure 3.8: *Examples of reflection and refraction. During refraction, the angles of incidence and refraction are related by the Snell's law.*

into an optical thicker medium, light is refracted towards the vertical. In the atmosphere, therefore, light is bent towards the normal while travelling from the sun to the surface. Atmospheric refraction depends on wavelength (larger for shorter wavelengths), on density and thus air humidity and temperature, and it is largest in the troposphere.
In order to check the correct treatment of the refraction phenomenon which occurs in the atmosphere, the main parameters which are used in the MODTRAN code to describe the refraction have been computed by the PROMSAR code. The comparison between the two model outputs is summarised in Table 3.6. Figure 3.9 moreover shows a graphical representation of such parameters, allowing to better understand their physical meaning. Consider the optical path through the atmosphere from point a to b as shown in Fig. 3.9. The path is defined by the initial and final altitudes z_a and z_b and by the zenith angle θ at a. The other path quantities are: S, the curved path length from a ("total range" in Table 3.6); β, the Earth-centered angle ("earth centre angle" in Table 3.6); ϕ, the zenith angle at b ("entrance angle" in Table

Table 3.6: *Refraction parameters comparison between MODTRAN and PROMSAR RTMs. Atmospheric scenario: 1976 U.S. Standard atmosphere; rural extinction and meteorological range of 23 km in the boundary layer; background stratospheric profile and extinction; λ = 0.440 μm.*

	SZA=30°		
	MODTRAN	PROMSAR	Err. %
TOTAL RANGE (km)	115.184	115.183	9E-04
ENTRANCE ANGLE (°)	150.501	150.501	-
EARTH CENTRE ANGLE (°)	0.510	0.510	-
BENDING (°)	0.009	0.009	-
	SZA=60°		
	MODTRAN	PROMSAR	Err. %
TOTAL RANGE (km)	195.708	195.700	4E-03
ENTRANCE ANGLE (°)	121.473	121.475	-2E-03
EARTH CENTRE ANGLE (°)	1.501	1.501	-
BENDING (°)	0.028	0.026	7
	SZA=80°		
	MODTRAN	PROMSAR	Err. %
TOTAL RANGE (km)	480.032	479.889	0.03
ENTRANCE ANGLE (°)	104.102	104.105	3E-03
EARTH CENTRE ANGLE (°)	4.190	4.189	0.02
BENDING (°)	0.088	0.084	5

3.6); and ψ, the total refractive bending along the path ("bending" in Table 3.6).

A further validation of the PROMSAR model concerning the calculation of the solar irradiance has been performed by comparison with experimental radiometer results. The radiometer in question is a narrowband multifilter radiometer for 4 wavelengths of UVB radiation, which operated at the ENEA (Ente per le Nuove Tecnologie, l'Energia e l'Ambiente) Research Centre of Brasimone (44.11 °N, 11.11 °E, 890 m a.s.l.) in October 1995. Since the radiometer operated the separation of direct and diffuse components of the radiation, calculations have been performed with the PROMSAR code for the spectral ratios between diffuse and total irradiances for different zenith angles and wavelengths of radiation. In this case, for each UV radiation wavelength, a library data set has been set up by using the MODTRAN code. Every library refers to a midlatitude winter model (fall-winter season) and, due to the Brasimone environmental characteristics, to a tropospheric extinction for the boundary layer aerosols. Background stratospheric aerosol were moreover considered. Table 3.7 resumes the experimental and computational results of a systematic comparison performed during the morning of a selected day

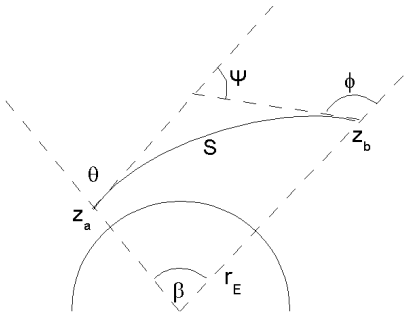

Figure 3.9: *Refracted slant path through the atmosphere from point a to point b.*

(24 October 1995), reporting the irradiance ratios to four different hours (9:00, 10:00, 11:00, 12:00 local time) and so to four different solar zenith angles (cos=0.35748, 0.46898, 0.53892, 0.56254). The percent differences between calculations and measurements are also quoted in Table 3.7. One can notice that the maximum divergence is equal to 4% for albedo=0.1 and to 3% for albedo=0.0. Both these values result smaller than the uncertainty of the instrument. There is a satisfying agreement with the results of the calculation code. The diffuse radiation component results greater for the shortest wavelengths (due to the λ^{-4} dependence). This phenomenon is more accentuated in the first hours of the morning.

Radiance

Here we compare the values of the single- and multiple-scattered radiance computed by the PROMSAR and MODTRAN codes for a ground-based point vertical radiometer. We assume three possible directions of the photon source, corresponding to SZA= 30°, 60°, and 80°. Results of this comparison are quoted in Table 3.8. The agreement between the two codes is again very good, with percent errors in most cases less than 1%.

3.4.2 Zenith-sky and off-axis Air Mass Factor calculations

The slant column densities observed by DOAS spectrometers are interpreted using the air mass factor (AMF) or enhancement factor, which is defined as the ratio between the column density of the constituent in the line of sight of observation (the slant column density) and the column density in the vertical (the vertical column density). In chapter 2 a detailed description

Table 3.7: *Diffuse to global irradiance ratio experiment-PROMSAR comparison (a=albedo). Atmospheric scenario: Midlatitude winter atmosphere; tropospheric extinction and meteorological range of 50 km in the boundary layer; background stratospheric profile and extinction; ha=0.9 km.*

cos = 0.35748 (9:00 a.m.)					
λ(nm)	Measured	a=0.0	Diff. %	a=0.1	Diff. %
318	0.880	0.875	0.6	0.880	-
312	0.899	0.894	0.6	0.898	0.1
305	0.918	0.931	-1.4	0.933	-1.6
300	0.965	0.978	-1.3	0.978	-1.3
cos = 0.46898 (10:00 a.m.)					
λ(nm)	Measured	a=0.0	Diff. %	a=0.1	Diff. %
318	0.771	0.774	-0.4	0.782	-1.4
312	0.801	0.794	0.9	0.802	-0.1
305	0.823	0.823	-	0.830	-0.9
300	0.877	0.852	2.9	0.857	2.3
cos = 0.53892 (11:00 a.m.)					
λ(nm)	Measured	a=0.0	Diff. %	a=0.1	Diff. %
318	0.701	0.716	-2.1	0.727	-3.6
312	0.732	0.734	-0.3	0.744	-1.6
305	0.754	0.754	-	0.762	-1.1
300	0.777	0.780	-0.4	0.787	-1.3
cos = 0.56254 (12:00 a.m.)					
λ(nm)	Measured	a=0.0	Diff. %	a=0.1	Diff. %
318	0.681	0.698	-2.5	0.709	-4.1
312	0.712	0.715	-0.4	0.726	-2.0
305	0.737	0.733	0.5	0.742	-0.7
300	0.747	0.767	-2.6	0.774	-3.6

of the AMFs useful for the interpretation of MAX-DOAS measurements was given. It has been shown that the MAX-DOAS configuration is particularly suitable for the derivation of the trace gases abundance in the troposphere and boundary layer.

Zenith-sky AMF

As already explained in chapter 2, before the off-axis and Multiple AXis DOAS spectrometers became attractive for the measurement of tropospheric constituents, ground-based spectrometers pointing the zenith were being used to investigate the stratospheric trace gases. However, from zenith-sky measurements, information about the tropospheric absorbers can be achieved to some degree. From the zenith-sky slant column's diurnal cycle, in fact, it can

Table 3.8: *Total single- and multiple- scattered radiance comparison between MODTRAN and PROMSAR. Atmospheric scenario: 1976 U.S. Standard atmosphere; rural extinction and meteorological range of 23 km in the boundary layer; background stratospheric profile and extinction; λ = 0.440 μm.*

	SZA=30°	
	Single-scattered radiance	(single + multiple)-scattered radiance
MODTRAN	2.27E-07	3.17E-07
PROMSAR	2.28E-07	3.18E-07
Err. %	-0.4	-0.3
	SZA=60°	
	Single-scattered radiance	(single + multiple)-scattered radiance
MODTRAN	5.64E-08	1.12E-07
PROMSAR	5.66E-08	1.19E-07
Err. %	-0.4	-6
	SZA=80°	
	Single-scattered radiance	(single + multiple)-scattered radiance
MODTRAN	1.65E-08	4.58E-08
PROMSAR	1.66E-08	4.68E-08
Err. %	-0.6	2

be determined if a gas mainly absorbs in the troposphere or in the stratosphere. In this section we report two examples which illustrate this idea.
We have considered the vertical profile of nitrogen dioxide provided within the "1976 U.S. Standard" atmosphere. It is shown in Fig. 3.10. We have then considered the same vertical profile of nitrogen dioxide, but only the values from the ground until 2 km (see Fig. 3.11), so as to treat the case of a trace gas in the boundary layer (we could have used the profile of a gas that we really know to be only located in the boundary layer/lower troposphere, such as, for example, the formaldeyde). Two radiative transfer calculations have been carried out with the PROMSAR model for the computation of the air mass factor of nitrogen dioxide at 440 nm, for the vertical profiles depicted in Figs. 3.10 and 3.11. For both the cases, we have used this model atmosphere: 1976 U.S. Standard atmosphere, rural aerosol extinction and meteorological range=23 km in the boundary layer, background stratospheric profile and extinction. The single and multiple scattering AMFs of the "stratospheric" and "tropospheric" nitrogen dioxide, and their percent differences are shown in Tables 3.9 and 3.10, respectively. It can be noticed that the percent differences between the single and multiple scattering AMFs shown in Table 3.9 are lower than those shown in Table 3.10. This indicates that, even if the air mass factor for the zenith sky configuration increases with multiple scatter-

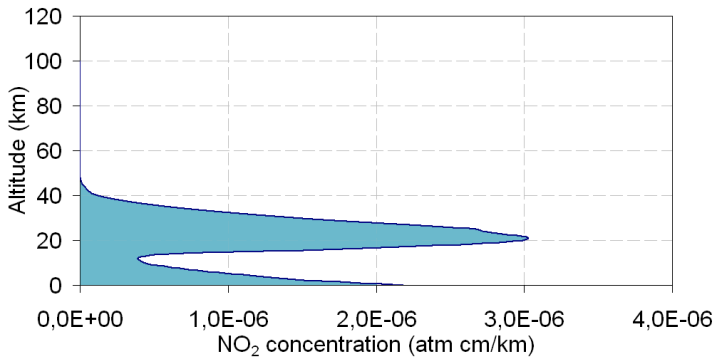

Figure 3.10: *NO_2 vertical profile provided by the 1976 U.S. Standard atmospheric model.*

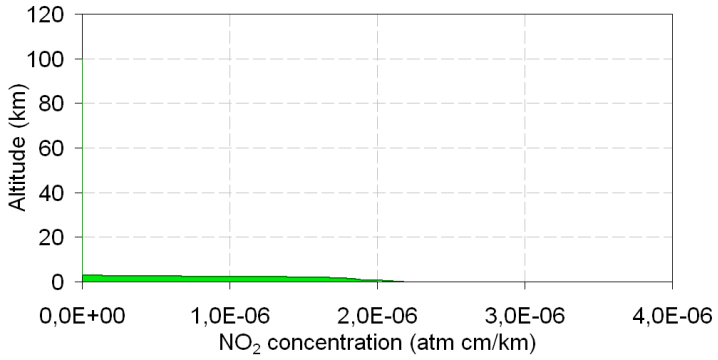

Figure 3.11: *NO_2 vertical profile between 0 and 2 km provided by the 1976 U.S. Standard atmospheric model.*

ing, the single scattering model can be considered a good approximation for stratospheric absorbers. However, when considering an absorber in the lower troposphere, multiple scattering has a consequence on the radiation transfer and, therefore, must be taken into account. The air mass factors listed in Tables 3.9 and 3.10 are shown in Fig. 3.12. As already pointed out (also in section 2.4), the dependence of the zenith-sky AMF on the solar zenith angle allows to identify either a trace gas is mainly located in the stratosphere or in the troposphere. For a stratospheric absorber like that shown in Fig. 3.10, the slant column and, hence, the air mass factor, increases with increasing SZA (see Fig. 3.12, blue lines) as long as the scattering height lies initially below and then within the absorbing layer. If at very low sun the most likely scattering height is situated above the absorbing layer the slant column de-

Table 3.9: *NO_2 AMF for single scattering approximation and multiple scattering at 440 nm. Atmospheric scenario: 1976 U.S. Standard atmosphere; rural extinction and meteorological range of 23 km in the boundary layer; background stratospheric profile and extinction.*

SZA(°)	NO_2 AMF single scattering	NO_2 AMF multiple scattering	Diff. %
5	1.004	1.015	1
10	1.015	1.031	2
15	1.034	1.054	2
20	1.062	1.087	2
25	1.099	1.130	3
30	1.148	1.186	3
35	1.211	1.257	4
40	1.291	1.347	4
45	1.393	1.459	5
50	1.524	1.606	5
55	1.697	1.793	5
60	1.929	2.044	6
65	2.255	2.388	6
70	2.734	2.894	6
75	3.501	3.695	5
80	4.883	5.134	5
85	7.935	8.290	5
90	16.87	17.35	3
91	20.10	20.56	2
92	23.64	23.87	1
93	27.07	27.13	0.2
94	28.62	29.02	1
95	26.07	28.98	10

creases in turn.
Instead, a trace gas in the lower troposphere (Fig. 3.11) absorbs below the most likely scattering height along a relatively short light path which changes only slightly with the solar zenith angle. By consequence, its slant column and, hence, air mass factor varies only slightly with the solar zenith angle (see Fig. 3.12, green lines).

Off-axis AMF

With regard to the AMF calculation in the off-axis/multiple axis geometry, several examples have been already shown in chapter 2, section 2.4.1. In this section, we just restrict ourselves to show two further examples of AMF

Table 3.10: *NO_2 AMF for single scattering approximation and multiple scattering at 440 nm. Atmospheric scenario: 1976 U.S. Standard atmosphere; rural extinction and meteorological range of 23 km in the boundary layer; background stratospheric profile and extinction. NO_2 between 0-2 km.*

SZA(°)	NO_2 AMF single scattering	NO_2 AMF multiple scattering	Diff. %
5	1.000	1.210	17
10	1.001	1.215	18
15	1.003	1.222	18
20	1.006	1.232	18
25	1.009	1.245	19
30	1.014	1.260	10
35	1.020	1.279	20
40	1.027	1.301	21
45	1.036	1.326	22
50	1.048	1.354	23
55	1.063	1.385	23
60	1.082	1.418	24
65	1.108	1.454	24
70	1.143	1.493	23
75	1.191	1.533	22
80	1.254	1.567	20
85	1.292	1.531	17
90	1.058	1.088	3
91	1.017	1.138	11
92	1.003	1.120	10
93	1.001	1.104	9
94	1.000	1.079	7
95	1.000	1.068	7

calculation in the off-axis configuration obtained with the PROMSAR code. In particular, we have considered two different profiles of nitrogen dioxide (those shown in Figs. 3.10 and 3.11), for which the single and multiple scattering AMFs have been calculated at different off-axis angles. The modelled off-axis angles between the telescope and the vertical direction (complementary angles to the "elevation angles" as defined in chapter 2) are 20°, 40°, 60°, and 80°. Results for the "stratospheric" (Fig. 3.10) and the "tropospheric" (Fig. 3.11) nitrogen dioxide AMFs are shown in Tables 3.11 and 3.12, respectively, and in Fig. 3.13 (only multiple scattering AMFs). We observe in Fig. 3.13 that differences in the multiple scattering AMFs at the different off-axis angles exist for both the "stratospheric" (Fig. 3.10) and the "tropospheric" (Fig. 3.11) nitrogen dioxide (see also Tables 3.11 and 3.12),

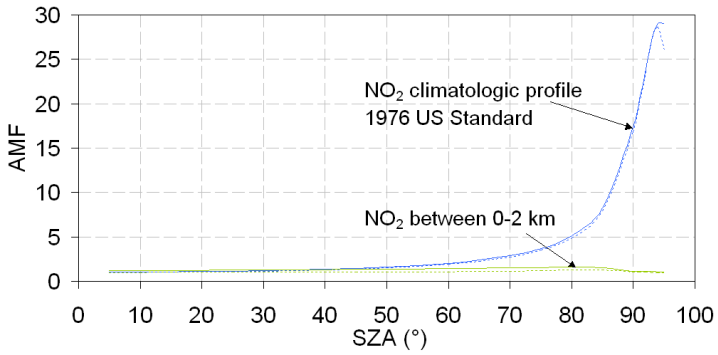

Figure 3.12: *Nitrogen dioxide air mass factors at 440 nm computed with the PROMSAR model for a stratospheric (Fig. 3.10) and a tropospheric/boundary layer (Fig. 3.11) vertical profile of the absorber. Dashed and solid lines indicate, respectively, single and multiple scattering AMFs.*

but they are especially evident in the case of the absorber located in the lower troposphere, as expected. On the other hand, the air mass factors for the horizon viewing mode are slightly increased by multilpe scattering for high sun, but clearly decreased at low sun.

Table 3.11: *NO_2 AMF for single/multiple scattering at 440 nm and for four off-axis angles (20°, 40°, 60°, 80°). Atmospheric scenario: 1976 U.S. Standard atmosphere; rural extinction and meteorological range of 23 km in the boundary layer; background stratospheric profile and extinction.*

	OA=20°			OA=40°			OA=60°			OA=80°		
SZA(°)	s.s	m.s.	%	s.s	m.s	%	s.s	m.s	%	s.s	m.s	%
5	1.008	1.035	2.6	1.021	1.082	5.6	1.052	1.161	9.4	1.08	1.21	10.7
10	1.019	1.041	2.1	1.032	1.085	4.9	1.062	1.163	8.7	1.096	1.214	9.7
15	1.037	1.053	1.5	1.051	1.096	4.1	1.081	1.171	7.7	1.114	1.224	9.0
20	1.064	1.066	0.2	1.078	1.117	3.5	1.108	1.191	7.0	1.142	1.246	8.3
25	1.1	1.118	1.6	1.115	1.148	2.9	1.146	1.22	6.1	1.179	1.276	7.6
30	1.147	1.173	2.2	1.163	1.193	2.5	1.195	1.261	5.2	1.229	1.321	7.0
35	1.208	1.242	2.7	1.224	1.246	1.8	1.258	1.318	4.6	1.293	1.378	6.2
40	1.285	1.33	3.4	1.302	1.305	0.2	1.339	1.392	3.8	1.375	1.456	5.6
45	1.385	1.441	3.9	1.402	1.427	1.8	1.442	1.489	3.2	1.482	1.557	4.8
50	1.513	1.585	4.5	1.529	1.568	2.5	1.574	1.617	2.7	1.62	1.689	4.1
55	1.682	1.773	5.1	1.698	1.75	3.0	1.745	1.78	2.0	1.802	1.866	3.4
60	1.908	2.024	5.7	1.926	1.995	3.5	1.977	1.984	0.4	2.05	2.108	2.8
65	2.224	2.367	6.0	2.244	2.334	3.9	2.302	2.347	1.9	2.398	2.449	2.1
70	2.688	2.87	6.3	2.71	2.829	4.2	2.772	2.843	2.5	2.912	2.956	1.5
75	3.421	3.652	6.3	3.446	3.606	4.4	3.518	3.621	2.8	3.725	3.756	0.8
80	4.727	5.037	6.2	4.755	4.98	4.5	4.837	4.994	3.1	5.169	5.173	0.1
85	7.593	8.063	5.8	7.676	8.001	4.1	7.773	8.008	2.9	8.068	8.138	0.9
90	15.82	17.17	7.9	16.75	17.43	3.9	17.56	17.67	0.6	17.2	17.23	0.2
91	18.12	19.81	8.5	19.21	20.22	5.0	20.7	20.76	0.3	20.75	20.39	-1.8
92	20.7	22.12	6.4	21.35	22.38	4.6	22.89	23.08	0.8	24.29	23.27	-4.4
93	22.02	23.38	5.8	22.22	23.32	4.7	24.1	24.41	1.3	27.21	25.15	-8.2
94	21.88	22.76	3.9	21.8	22.66	3.8	22.35	23.63	5.4	25.96	23.43	-10.8
95	19.5	19.32	-0.9	20.12	20.32	1.0	21.91	21.76	-0.7	26.78	23.82	-12.4

Table 3.12: *NO_2 AMF for single/multiple scattering at 440 nm and for four off-axis angles (20°, 40°, 60°, 80°). Atmospheric scenario: 1976 U.S. Standard atmosphere; rural extinction and meteorological range of 23 km in the boundary layer; background stratospheric profile and extinction. NO_2 between 0-2 km.*

	OA=20°			OA=40°			OA=60°			OA=80°		
SZA(°)	s.s	m.s.	%	s.s	m.s	%	s.s	m.s	%	s.s	m.s	%
5	1.047	1.13	7.3	1.226	1.429	14.2	1.729	2.161	20.0	3.593	4.502	20.2
10	1.05	1.119	6.2	1.227	1.404	12.6	1.727	2.129	18.9	3.578	4.455	19.7
15	1.055	1.104	4.4	1.231	1.384	11.1	1.724	2.086	17.4	3.559	4.398	19.1
20	1.064	1.07	0.6	1.238	1.372	9.8	1.729	2.065	16.3	3.558	4.363	18.5
25	1.076	1.129	4.7	1.248	1.363	8.4	1.736	2.04	14.9	3.555	4.315	17.6
30	1.089	1.167	6.7	1.262	1.361	7.3	1.748	2.023	13.6	3.573	4.297	16.8
35	1.105	1.204	8.2	1.278	1.352	5.5	1.765	2.014	12.4	3.591	4.27	15.9
40	1.125	1.25	10.0	1.305	1.314	0.7	1.79	2.015	11.2	3.634	4.283	15.2
45	1.149	1.304	11.9	1.339	1.421	5.8	1.822	2.023	9.9	3.689	4.295	14.1
50	1.177	1.367	13.9	1.372	1.495	8.2	1.864	2.042	8.7	3.767	4.321	12.8
55	1.209	1.439	16.0	1.415	1.571	9.9	1.914	2.05	6.6	3.876	4.85	20.1
60	1.245	1.519	18.0	1.465	1.66	11.7	1.999	2.016	0.8	4.028	4.484	10.2
65	1.287	1.599	19.5	1.526	1.795	15.0	2.109	2.253	6.4	4.238	4.634	8.5
70	1.323	1.679	21.2	1.591	1.861	14.5	2.217	2.416	8.2	4.54	4.859	6.6
75	1.348	1.715	21.4	1.645	1.943	15.3	2.342	2.569	8.8	4.965	5.163	3.8
80	1.301	1.668	22.0	1.625	1.929	15.8	2.41	2.647	9.0	5.735	5.74	0.1
85	1.132	1.45	21.9	1.41	1.706	17.4	2.173	2.432	10.6	6.306	5.942	-6.1
90	1.064	1.325	19.7	1.305	1.568	16.8	1.999	2.269	11.9	5.736	5.388	-6.5
91	1.064	1.328	19.9	1.305	1.569	16.8	1.999	2.271	12.0	5.736	5.392	-6.4
92	1.064	1.338	20.5	1.305	1.574	17.1	1.999	2.283	12.4	5.736	5.402	-6.2
93	1.064	1.357	21.6	1.305	1.582	17.5	1.999	2.31	13.5	5.736	5.404	-6.1
94	1.064	1.387	23.3	1.305	1.605	18.7	1.999	2.355	15.1	5.736	5.379	-6.6
95	1.064	1.399	23.9	1.305	1.644	20.6	1.999	2.372	15.7	5.736	5.318	-7.9

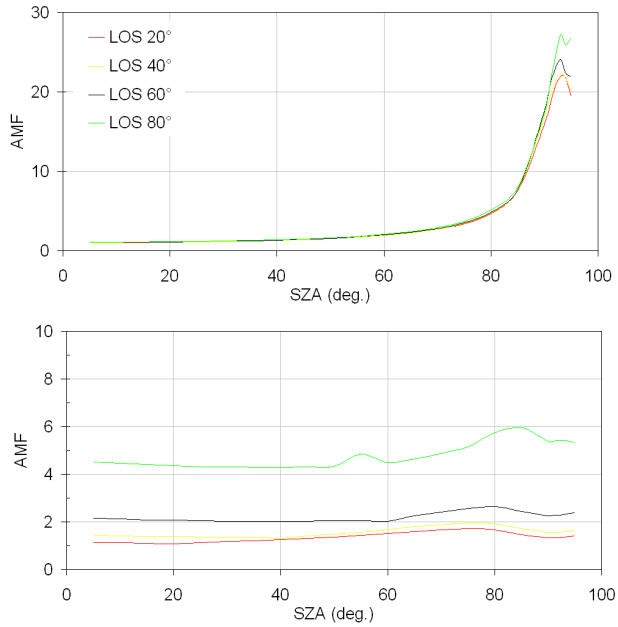

Figure 3.13: *Nitrogen dioxide air mass factors at 440 nm computed with the PROMSAR model for the stratospheric NO_2 vertical profile shown in Fig. 3.10 (top) and the tropospheric NO_2 vertical profile shown in Fig. 3.11 (bottom), and for four off-axis angles (20°, 40°, 60°, 80°).*

Chapter 4

Remote sensing and the retrieval problem

> *Remote Sensing is the science and art of obtaining information about an object, area, or phenomenon through the analysis of data acquired by a device that is not in contact with the object, area, or phenomenon under investigation.*
> T. M. Lillesand and M. W. Kiefer, **Remote Sensing and Image Interpretation**

> *Remote Sensing is defined as the acquisition of information about an object without being in physical contact with it.*
> C. Elachi, **Introduction To The Physics and Techniques of Remote Sensing**

> *Remote Sensing is the science of acquiring, processing and interpreting images that record the interaction between electromagnetic energy and matter.*
> F. F. Sabins, **Remote sensing: principles and interpretation**

Broadly speaking, remote sensing is a way of obtaining information about properties of an object or volume without coming into physical contact with that object. We may so consider remote sensing to be an indirect measurement method, i.e. we do not measure directly but by means of, for instance, electromagnetic radiation as an information carrier.

Problems of remote sensing fall into a category referred to as *inverse problems*. The nature of these inverse problems is portrayed in Fig. 4.1 in the form of an analogy, and can be posed in the following way. How well can we infer the animal from observations of its tracks? Clearly this line of

inquiry is fruitless without *a priori* knowledge of animals and the types of tracks they leave.

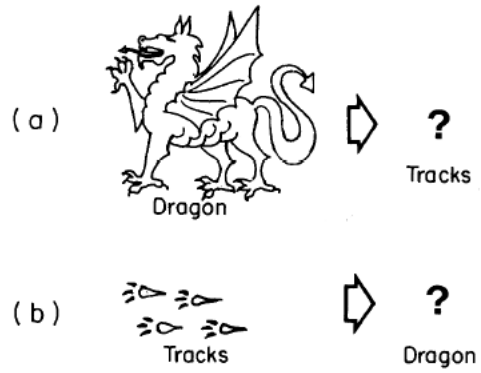

Figure 1.2 (a) The direct problem: Describe the tracks of a dragon. (b) The inverse problem: Describe a dragon from its tracks (from Bohren and Huffman, 1983.)

Figure 4.1: *The nature of inverse problems, from Stephens [54].*

The atmosphere is a typical subject for which remote sensing measurements are effective, and for which inverse methods are required. Therefore a central theme in remote sensing of the atmosphere is the understanding of how electromagnetic radiation interacts with matter since these are the tracks we exploit to infer information about the atmosphere.
The example dealt with in this thesis is one in which electromagnetic radiation emerging from the atmosphere is measured by a spectrometer and processed by the DOAS algorithm to obtain the slant column density of a trace gas (i.e. the integrated concentration along the light path), when the quantity required is the vertical profile of the trace gas in question. Of course, the slant column density is a function of the trace gas vertical profile we want to obtain. So, we have to retrieve the unknown quantity we are interested in from the measurements made. This reconstruction is called "retrieval".

The usual approach to solving a retrieval problem in the frame of the atmospheric sciences consists of several stages: design a forward model to describe the physics of the measurement and the instrument; determine the criterion by which a solution is acceptable as valid; construct a numerical method to find a solution which satisfies the criterion; carry out an error analysis, validate the process by reference to internal diagnostics and independent measurements, and finally attempt to understand how the result obtained is related to reality and examine how much information has been

obtained and with which reliability.

4.1 Atmospheric remote sensing

How well can we infer the animal from observations of its tracks?

4.1.1 The beginnings

Atmospheric inverse problems began in 1920's when Dobson started to make measurements of ozone in the stratosphere using an ultraviolet spectrometer on the ground. The initial measurements were of total ozone, based on absorption of solar ultraviolet light, but it was realized by Götz in 1930 that by measuring the Rayleigh scattered sunlight from the zenith sky as the sun sets it is possible to obtain information about the vertical distribution of ozone [55]. This is the so-called *Umkehr* method. The word umkehr means "reversal" and refers to the time variation of the ratio of the scattered intensity at two different wavelengths. Methods for deriving the vertical distribution from the umkehr curve were developed by Götz, Dobson and Meetham [15]. It was not until Mateer [56] carried out its seminal work on the information content of umkehr observations that the subject was put on a firm footing.

With the advent of meteorological satellites, it became clear that remote measurements from space would be very important in determining the state of the atmosphere globally. Kaplan [57] proposed that the vertical distribution of temperature in the atmosphere could be determined globally by measuring from satellites, as a function of wavelength, the thermal emission from the 15 μm band of carbon dioxide, and also pointed out that ozone and water vapour should also be amenable to remote measurement. Kaplan only gave a qualitative suggestion about how the profiles might be retrieved; detailed methods were developed by Wark [58] and Yamamoto [59] in two of the earliest papers on the subject of inverse theory for atmospheric remote sounding from satellites.

4.1.2 Atmospheric remote sensing methods

Remote sensing of the atmosphere has been carried out by a wide variety of instruments, using many different principles of measurement and platforms. Almost all techniques involve the measurement of electromagnetic radiation. The physical effects exploited may involve extinction, scattering, absorption,

emission at all wavelengths from radio to the ultraviolet. The measurement techniques and instruments include spectrometers, interferometers, radiometers, gas correlation methods, microwave and radio receivers. Most methods are passive, measuring naturally generated radiation, but some (e.g. lidar) are active in that they use man-made sources.

As already pointed out, the first remote measurements of the atmospheric composition was of total ozone using absorption of solar radiation. The same principle can be used for the measurement of a wide variety of gases, particularly in the infrared and microwave, where many constituents have absorption lines and bands, but also in the ultraviolet and visible, as in the case of Differential Optical Absorption Spectroscopy.

In the following sections, we will briefly discuss the theoretical basis of retrieval problems, especially following the work of Rodgers. A special inversion method, the *Chahine relaxation method*, will be in particular described. In chapter 5, the application of the Chahine relaxation method to a set of slant column densities measured by a MAX-DOAS instrument will be discussed, and the retrieved NO_2 and ozone vertical profiles will be presented in detail.

4.2 Information aspects in retrieval methods

Different remote sensing problems and related retrieval methods reduce to find the solution of equations like or similar to

$$g(y) = \int_a^b K(y,x) f(x) dx \qquad a \leq y \leq b, \tag{4.1}$$

where the limits of the integral depend on the details of the problem at hand. This equation is known as the *Fredholm integral equation of the first kind* because the limits of the integral are fixed and because the unknown, $f(x)$, appears only in the integrand. The function $K(y,x)$ is known as the *kernel* or *kernel function*. $f(x)$ can be obtained by solving Eq. 4.1 when $g(y)$ is the observation at various y values and the kernel is known. Solution to Eq. 4.1 requires inversion to obtain the distribution $f(x)$. This is an unfotunate circumstance since the solutions to Eq. 4.1 suffer a number of difficulties, including non-existence, non-uniqueness, and instability. Non-existence is usually not an issue for most practical problems since we measure $g(y)$ and $f(x)$ exists through physical considerations. Non-uniqueness is related to a blurring effect or a departure from one-to-one correspondence between $f(x)$ and $g(y)$: there exist several functions $f(x)$ which produce the same function $g(y)$. This problem tends to be overcome to a certain extent by restricting the

class of admissible solutions to physically realizable ones. In this way, *a priori* information is introduced into the retrieval scheme. The major difficulty in solving Eq. 4.1, at least for most practical problems, concerns the problem of instability which arises, for example, from errors in the observations $g(y)$. With a small error $\epsilon(y)$ in $g(y)$, Eq. 4.1 becomes

$$g(y) + \epsilon(y) = \int_a^b K(y,x) f(x) dx, \tag{4.2}$$

where $\epsilon(y)$ produces an arbitrary large change in $f(x)$ and the ultimate success of any retrieval largely depends on the accuracy of the measurement $g(y)$ and on the shape of $K(y,x)$.

In most practical situations, numerical methods are used for inversion of Eq. 4.1. A full overview of these methods and their applications can be found in [60]. An important contribution to these issues came from Rodgers, who worked to the formal statement of the problem, which also includes a treatment of errors (see e.g. [61] and [62]).

4.2.1 Formal statement of the problem

The general inverse problem can be regaded as a question of setting up and solving a set of simultaneous linear or non-linear equations, in the presence of experimental error in some of the parameters (the "measurements"), and quite possibly in the presence of approximations in the formulation of the equations. To examine the information content of the indirect measurement, we will cosider the measurements assembled into a vector $\vec{y}$, the *measurement vector*, and the unknowns into a *state vector* $\vec{x}$, describing the state of the atmosphere. Some aspects of the state of the atmosphere, for example the trace gases distribution, are properly described by continuous functions rather than discrete values, but ways can always be found of approximating continuous functions by discrete values to any desired accuracy. The process of measurement will be described by a *forward model*, which describes the physics of the measurement process.

State and measurement vectors

The quantities to be retrieved can be represented by a state vector, $\vec{x}$, with n elements, $x_1, x_2, \cdots, x_n$. Often it will represent a profile of some quantity given at a finite number of levels, enough to adequately represent the possible atmospheric variations.

The quantity actually measured in order to retrieve $\vec{x}$ can be represented by the measurement vector $\vec{y}$, with m elements, $y_1, y_2, \cdots, y_m$. This vector

should include all the quantities measured that are functions of the state vector. Measurements are made to a finite accuracy; random error or *measurement noise* will be denoted by the vector ϵ.

The forward model

For each state vector there is a corresponding ideal measurement $\vec{y}_I$, determined by the physics of the measurement. We can describe the physics formally as the *forward function* $f(\vec{x})$, so that

$$\vec{y}_I = f(\vec{x}). \tag{4.3}$$

However, in practice not only is there always experimental error, but it is often necessary to approximate the detailed physics by some *forward model* $F(\vec{x})$. Therefore we will write the relationship between the measurement vector and the state vector as

$$\vec{y} = F(\vec{x}) + \epsilon, \tag{4.4}$$

where the vector $\vec{y}$ is the measurement with error ϵ, and $F(\vec{x})$ is a vector valued function of the state, which encapsulates our understanding of the physics of the measurement. To construct a forward model we must of course know how the device works, and understand how the quantity measured is related to the quantity that is really wanted. F is described as a *model* because there may be underlying physics which is not fully understood, or the real physics may be so complicated that approximations are necessary.

The quantities to be retrieved in most inverse problems are continuous functions, while the measurements are always of discrete quantities. Thus most inverse problems are formally ill-posed or underconstrained in this trivial sense. This is simply dealt with by replacing the truly continuous state function, corresponding to a finite number of variables, with a representation in terms of a finite number of parameters. This can be done to whatever spatial resolution or degree of accuracy is required for scientific use of the retrieval, e.g., the profile of a trace gas could be represented on a finite grid of points with a spacing appropriate to the application. After discretisation the problem may or may not be underconstrained, depending on the grid spacing required and the information content of the measurement.

Weighting function matrix

For the purpose of examining the information content of a measurement it is most convenient to consider a linear problem. A linearisation of the forward model about some reference state $\vec{x}_0$ will be adequate for this purpose,

provided that $F(\vec{x})$ is linear within the error bounds of the retrieval. Write

$$\vec{y} = F(\vec{x}_0) + \frac{\partial F(\vec{x})}{\partial \vec{x}}(\vec{x} - \vec{x}_0) + \epsilon \tag{4.5}$$

$$\vec{y} - F(\vec{x}_0) = \frac{\partial F(\vec{x})}{\partial \vec{x}}(\vec{x} - \vec{x}_0) + \epsilon \tag{4.6}$$

$$\vec{y} - F(\vec{x}_0) = K(\vec{x} - \vec{x}_0) + \epsilon, \tag{4.7}$$

which defines the $m \times n$ *weighting function matrix* K, not necessarily square, in which each element is the partial derivative of a forward model element with respect to a state vector element, i.e., $K_{ij} = \partial F_i(\vec{x})/\partial \vec{x}_j$. Derivative of this type are known as Fréchet derivatives. If $m < n$ the equations are described as underconstrained because there are fewer measurements than unknowns. Similarly, if $m > n$ the equations are often described as overconstrained.

Vector spaces

The concept of a *linear vector space* is very useful in considering linear equations. We will give two such spaces special names: the *state space* is a vector space of dimension n within which each conceivable state is represented by a point, or equivalently by a vector from the origin (x_0) to the point. The *measurement space* is a vector space of dimension m, in which each conceivable measurement is likewise represented by a point or a vector (with the origin at $F(x_0)$). The act of measurement is then equivalent to a mapping from the state space into the measurement space, and the inverse problem is that of finding an appropriate inverse mapping from the measurement space back into the state space. The weighting function matrix K represents the forward mapping, equivalent to the measurement apart from the measurement error ϵ. Each row of K, of dimension n, can be thought of as a vector k_i in state space. It corresponds to the i^{th} measurement y_i in the sense that the value of the i^{th} coordinate of measurement space for a given state vector $\vec{x}$ is the vector product of $\vec{x}$ and k_i, plus measurement error. Thus each of the m rows of K corresponds to a coordinate in measurement space, providing the mapping from state space to measurement space.

4.2.2 Linear problems without measurement error

Consider first a linear problem with arbitary numbers of dimensions in the absence of measurement error. In this case the problem reduces to the exact solution of linear simulatneous equations,

$$\vec{y} = K\vec{x}, \tag{4.8}$$

and involves determining how many solutions exist, if they exist. More generally, it is a matter of investigating what information can be extracted from the measurements $\vec{y}$ about the space $\vec{x}$ particularly when there is no solution or no unique solution.

The m weighting function vectors k_j will span some *subspace* of state space which will be of dimension not greater then m, and may be less than m if the vectors are not linearly independent. The dimension of this subspace is known as the *rank* of the matrix K, denoted by p, and is equal to the number of linearly independent rows. If $m > n$, more measurements than unknowns, then the rank cannot be greater than n. The subspace spanned by the vectors forming the rows of K is called the *row space* of K. K also has a *column space* of dimension p which is a subspace of measurement space.
We can imagine an orthogonal coordinate system or *base* for the state space which has p orthogonal *base vectors* in row space, and $n-p$ base vectors outside which are orthogonal to row space and, therefore, to all of the weighting function vectors. The components of the state vector orthogonal to row space will give a zero contribution to the measurement, i.e. are unmeasurable. This part of the state space is called *null space* of K.
If $p < n$ the null space exists: in this case the solution is non-unique because there are components of the state space which are not determined by the measurements, and which could therefore take any value.

4.2.3 Linear problems with measurement error

All real measurements are subject to experimental errors. The proper treatment of such errors is fundamental in designing retrieval methods.
A description of experimental error in term of probability density functions ($pdf's$) gives useful insight. The statement that a scalar measurement has a value $\bar{y}$ and an error σ is a shorthand way of saying that our knowledge of the true value of the measured parameter is described by a *pdf* $P(y)$ with a mean $\bar{y}$ and a variance σ^2:

$$\bar{y} = \int y \cdot P(y) dy \tag{4.9}$$

$$\sigma^2 = \int (y - \bar{y})^2 \cdot P(y) dy \tag{4.10}$$

and that the probability that y lies in $(y, y+dy)$ is $P(y)dy$. The form of $P(y)$ is almost always taken to be Gaussian: this is usually a good approximation fo experimental error, and is very convenient for algebraic manipulations.
When the measured quantity is a vector, a probability density can still be

defined over measurement space, $P(\vec{y})$, with the interpretation that $P(\vec{y})d\vec{y}$ is the probability that the true value of the measurement lies in a multidimensional interval $(\vec{y}, \vec{y} + d\vec{y})$ in measurement space. Different elements of a vector may be correlated, in the sense that

$$S_{ij} = E\{(y_i - \bar{y}_i)(y_j - \bar{y}_j)\} \neq 0, \tag{4.11}$$

where S_{ij} is called the *covariance* of y_i and y_j and E is the expected value operator. These covariances can be assembled into a matrix, which we will denote by S_y for the covariance matrix of $\vec{y}$. Its diagonal elements are clearly the variances of the individual elements of $\vec{y}$. A covariance matrix is symmetric and non-negative definite, and is almost always positive definite.

4.3 Error analysis in retrieval methods

In this section we will carry out a general characterisation and error analysis, following the methods developed by Eyre [63] and Rodgers [61], that can be applied to any inverse method and which will show how a retrieval is related to the true state of e.g. the atmosphere, and how various sources of errors propagate into the final product.

4.3.1 Characterisation

The forward model

For any remote measurement, the quantity measured, $\vec{y}$, is some vector valued function f of the unknown state vector, $\vec{x}$, and of some other set of parameters, $\vec{b}$, that we have decided not to include in the state vector. There is also an experimental error term, ϵ. Therefore we write, more generally than Eq. 4.4:

$$\vec{y} = f(\vec{x}, \vec{b}) + \epsilon, \tag{4.12}$$

where the *Forward Function* f describes the complete physics of the measurement, including for example the radiative transfer theory required to relate the state to the measured signal, as well as a full description of the measuring instrument. The vector of parameters $\vec{b}$ comprises those quantities which influence the measurement, are known to some accuracy, but are not intended as quantities to be retrieved. They will be termed the *forward function parameters* and will contribute to the total measurement accuracy. The error term ϵ includes errors from sources which are not related to the forward function parameters.

The retrieval method

The retrieval $\hat{x}$ is the result of operating on the measurement with some *Retrieval Method* R,

$$\hat{x} = R(\vec{y}, \hat{b}, \vec{x}_a, \vec{c}), \tag{4.13}$$

where the circumflex does not indicate a true state but an estimated quantity. $\hat{b}$ is the best estimate of the forward function parameters, the vectors $\vec{x}_a$ and $\vec{c}$ together comprise the parameters that do not appears in the forward function, but do affect the retrieval. $\vec{x}_a$ is any *a priori* estimate of $\vec{x}$ that may be used and $\vec{c}$ contains any other parameters of this nature. Some inverse methods use an explicit *a priori*, some do not. The *a priori* estimate can be thought of as any kind of estimate of the state used in the inverse method and which is unrelated to the actual measurement. The parameters comprising $\vec{c}$ will be called *retrieval method parameters*.

The transfer function

By substituting Eq. 4.4 into Eq. 4.13, we can relate the retrieval to the true state:

$$\hat{x} = R(f(\vec{x}, \vec{b}) + \epsilon, \hat{b}, \vec{x}_a, \vec{c}). \tag{4.14}$$

Eq. 4.14 can be regarded as a *Transfer Function* which describes the way in which the whole system can operate, including both the measuring instrument and the retrieval method. Understanding the properties of the transfer function is fundamental to both *characterization* of the observing system (i.e., the sensitivity of the retrieved to the true state, expressed as $\partial\hat{x}/\partial\vec{x}$) and the *error analysis* (i.e., the sensitivity of the retrieval to all of the sources of error in the transfer function, including noise in the measurement, error in the non-retrieved parameters and in the retrieval method parameters, and the effect of modelling the true physics of the measurement by means of a forward model).

Linearisation of the transfer function

The forward function is often a source of difficulty, due to the fact that the real physics is far too complex (or uncertain) to deal with explicitly. For that reason, a *Forward Model*, F, with associated errors, may be used:

$$F(\vec{x}, \vec{b}) \cong f(\vec{x}, \vec{b}, \vec{b'}) \tag{4.15}$$

where $\vec{b}$ has been separated into $\vec{b}$ and $\vec{b'}$, where $\vec{b'}$ represents those forward function parameters which are ignored in the construction of the forward model. Replacing the forward function by the forward model, and including an error term to allow for this, Eq. 4.14 becomes:

$$\hat{x} = R[F(\vec{x}, \vec{b}) + \Delta f(\vec{x}, \vec{b}, \vec{b'}) + \epsilon, \hat{b}, \vec{x}_a, \vec{c}], \tag{4.16}$$

where Δf is the error in the forward model relative to the real physics:

$$\Delta f = f(\vec{x}, \vec{b}, \vec{b'}) - F(\vec{x}, \vec{b}). \tag{4.17}$$

The forward model can be then linearised about $\vec{x} = \vec{x}_a$ and $\vec{b} = \hat{b}$:

$$\hat{x} = R[F(\vec{x}_a, \hat{b}) + K_x(\vec{x} - \vec{x}_a) + K_b(\vec{b} - \hat{b}) + \Delta f(\vec{x}, \vec{b}, \vec{b'}) + \epsilon, \hat{b}, \vec{x}_a, \vec{c}], \tag{4.18}$$

where the matrix $K_x = \partial F / \partial \vec{x}$ is the sensitivity of the forward model to the state, the weighting function or Jacobian matrix, and $K_b = \partial F / \partial \vec{b}$ is the sensitivity of the forward model to the forward model parameters. Next, the inverse method can be linearised with respect to its first argument, $\vec{y}$,

$$\hat{x} = R[F(\vec{x}_a, \hat{b}), \hat{b}, \vec{x}_a, \vec{c}] + G_y[K_x(\vec{x} - \vec{x}_a) + K_b(\vec{b} - \hat{b}) + \Delta f(\vec{x}, \vec{b}, \vec{b'}) + \epsilon], \tag{4.19}$$

where $G_y = \partial R / \partial \vec{y}$ is the sensitivity of the retrieval to the measurement, which is the same as its sensitivity to measurement error. Rearranging Eq. 4.19 we obtain

$$\begin{aligned} \hat{x} - \vec{x}_a = {} & R[F(\vec{x}_a, \hat{b}), \hat{b}, \vec{x}_a, \vec{c}] - \vec{x}_a + \\ & + A(\vec{x} - \vec{x}_a) + \\ & + G_y \epsilon_y, \end{aligned} \tag{4.20}$$

where

$$A = G_y K_x = \frac{\partial \hat{x}}{\partial \vec{x}} \tag{4.21}$$

is the sensitivity of the retrieval to the true state and

$$\epsilon_y = K_b(\vec{b} - \hat{b}) + \Delta f(\vec{x}, \vec{b}, \vec{b'}) + \epsilon \tag{4.22}$$

is the total measurement error in the relative to the forward model.

The first term on the right hand side of Eq. 4.20, the *bias*, is the error that would result from a simulated retrieval using a simulated error-free measurement of the *a priori* state computed with the forward model. The *a priori* represents knowledge of the state before the measurement is made.

If the measurement were not made, *a priori* would be our only knowledge. Thus if the measurements are consistent with the state being equal to the *a priori*, then any "correct" inverse method should return the *a priori*, i.e. the first term of Eq. 4.20 should be zero. The linearization has been carried out about the *a priori* state mainly so that the bias term can be eliminated. Consequently, the above argument can only be applicable to methods using an explicit *a priori*.
The second term on the right hand side of Eq. 4.20, the *smoothing*, represents the way in which the observing system smooths the profile. The difference between the retrieval and the linearization point is obtained by operating on the difference between the true state and the linearization point with the matrix A:

$$\hat{x} = \vec{x}_a + A(\vec{x} - \vec{x}_a) + G_y\epsilon_y = (I_n - A)\vec{x}_a + A\vec{x} + G_y\epsilon_y. \tag{4.23}$$

In the case where the state vector represents a profile, then rows a_i^T of A can be regarded as smoothing functions or averaging kernels. In the ideal inverse method, A would be a unit matrix. In reality, rows of A are generally peaked functions, peaking at the appropriate level, and with a half-width which is a measure of the spatial resolution of the observing system, thus providing a simple characterization of the relationship between the retrieval and the true state. The averaging kernel also has an area, which is found to be approximately unity at level where the retrieval is accurate, and in general can be thought of as a rough measure of the fraction of the retrieval that comes from the data, rather than from the *a priori*.
The third term on the right hand side of Eq. 4.20, the *retrieval error*, is the error in the retrieval due to the total measurement (ϵ_y) which does not include the error of the retrieval process.

4.3.2 Error analysis

An expression for the error in $\hat{x}$ can be obtained by some further rearrangements of Eqs. 4.20 and 4.22:

$$\begin{aligned}\hat{x} - \vec{x} = {} & (A - I_n)(\vec{x} - \vec{x}_a) + \\ & + G_y K_b(\vec{b} - \hat{b}) + \\ & + G_y \Delta f(\vec{x}, \vec{b}, \vec{b'}) + \\ & + G_y\epsilon.\end{aligned} \tag{4.24}$$

The four contributions are, respectively from top to bottom, the *smoothing error*, the *model parameter error*, the *forward model error* and the *retrieval noise*. For a full explanation of such error contributions and related topics, see [62].

4.4 The Chahine inversion method

In most circumstances the maximum amount of information will be extracted from a set of measurements when we use a full non-linear retrieval which minimises a cost function based on all the data and appropriate *a priori*. Since these methods can be time consuming, approximate and numerically fast methods can be useful. One possibility is given by the non-linear relaxation method whose simplest form was popularised by Chahine [64].
A non-linear relaxation method follows the same general idea as the linear relaxation (see, e.g. [62]), except that the iteration equation is non-linear. At iteration i the value at each level j, x_j^i, is modified by multiplying by the ratio of the corresponding measured to computed signal, $y_j/F_j(x^i)$:

$$x_j^{i+1} = x_j^i \cdot \frac{y_j}{F_j(x^i)}. \tag{4.25}$$

For well peaked weighting functions, one would expect this to converge to a profile which produces the right computed signal.
Convergence can be analysed by taking logarithms:

$$\ln x_j^{i+1} = \ln x_j^i + [\ln y_j - \ln F_j(x^i)]. \tag{4.26}$$

4.4.1 Application of the Chahine inversion method

We have seen in chapter 2 (Eq. 2.2) that the relationship between the zenith-sky slant column density of a given trace gas at a given wavelength λ and solar zenith angle SZA, $y_\lambda(SZA)$, and its concentration at a given altitude z, $c_g(z)$, can be expressed by the following equation

$$y_\lambda(SZA) = \frac{-\ln \frac{I(SZA,\lambda)}{I_0(\lambda)}}{\sigma_g} = \int_0^Z c_g(z) \cdot AMF_\lambda(z, SZA) \cdot dz. \tag{4.27}$$

Assuming that the absorber concentrations remain constant during the measurement (e.g. during twilight), the variation in observed zenith-sky slant column with increasing solar zenith angle contains information regarding the vertical profile of the absorber: inversion techniques provide a means of determining the profile from such measurements.
The evident analogy between Eqs. 4.27 and 4.1 highlights that the air mass factor, $\mathrm{AMF}_\lambda(z,\mathrm{SZA})$, is the kernel of Eq. 4.27. Therefore, the retrieval of trace gases vertical profile relies on forward model calculations of the changes in air mass factor (and hence, slant column density) as a function of SZA.

In other words, fundamental in the inversion process is modelling the measurements through a radiative transfer model, which allows to construct the following linear matrix model

$$y_i^m = AMF_{ij} \cdot c_j \tag{4.28}$$

where y_i^m is the modelled (superscript m) slant column at solar zenith angle i, AMF_{ij} is the air mass factor for the trace gas added to layer j, and c_j is the amount of the trace gas in layer j.
In principle one can solve Eq. 4.28 for the concentrations in each modelled layer, in the form

$$c_j = A_{ji} y_i^o \tag{4.29}$$

where A_{ji} is the inverse of AMF_{ij} (if it is a square matrix and nonsingular) or some other estimator such as a least squares formulation, and y_i^o is the column amount observed (superscript o) at solar zenith angle i. Unfortunately, seeking a solution using an unconstrained linear method in the presence of measurement noise can lead to physically unrasonable solutions such as negative amounts in particular atmospheric layers.

The inverse problem may be approached in these cases using the Chahine solution method, which has been introduced in section 4.4.
The solution process is started by assuming a profile, $c_j^{n=1}$, of the trace gas under study for the first iteration, a *first guess* profile. The (n^{th}) iteration solution profile, c_j^n, together with the model are used to determine the $(n{+}1)^{st}$ estimate of the concentration profile by the equation:

$$c_j^{n+1} = c_j^n \cdot \sum_{l=1}^{NL} [W_{jl} \cdot \frac{y_{k(j)}^o}{y_{k(j)}^m}] \tag{4.30}$$

where $k(j)$ represents the solar zenith angle at which layer j has the largest AMF, NL is the number of layers in the model atmosphere and W_{jl} are a set of weighting factors that are introduced to stabilize the convergence of the solution in the presence of significant correlations between the rows of the matrix AMF_{ij}. The weighting factors are computed using the following relation:

$$W_{jl} = \frac{AMF_{k(l)j}}{AMF_{k(l)l}} \tag{4.31}$$

for each layer l, and then W_{jl} are normalized using

$$W_{jl} = \frac{W_{jl}}{\sum_{j=1}^{NL} W_{jl}}. \tag{4.32}$$

The iterations continue until the fitting error between the observed and the modelled values, $y_i^o - y_i^m$, is approximately the same size as the estimated uncertainty in the observations, or until a specified maximum number of iterations has been reached.

The Chahine method was successfully applied by McKenzie et al. [65] for the retrieval of the vertical profile of atmospheric absorbers such as ozone and NO_2 from ground-based zenith-sky DOAS measurements at Lauder, New Zealand (45° S, 170° E). McKenzie demonstrated that this method was able to retrieve profile information from the ground to 50 km and, moreover, it was particularly valuable for identifying the influence of pollution on such measurements. Results found by McKenzie are here summarised for nitrogen dioxide only.

A typical time series of daily NO_2 measurements made at Lauder is shown in Fig. 4.2.

The air mass factor calculations were performed by the radiative transfer model developed by Solomon et al. [31]; for that purpose the atmosphere was divided into 10 assumed layers of thickness 5 km ranging from the ground to 50 km. The air mass factors were calculated at integer steps in SZA be-

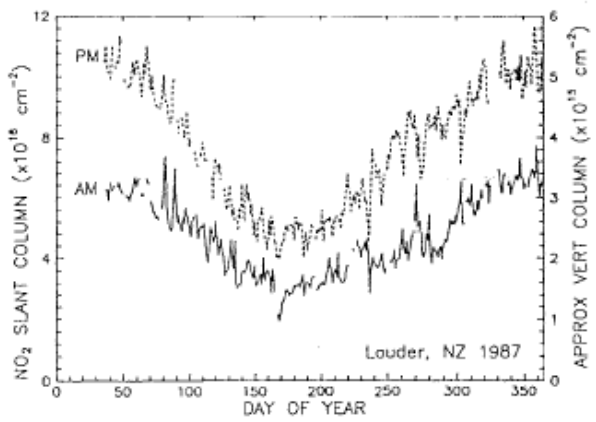

Figure 4.2: *Time series of slant column densities of NO_2 at sunrise and sunset during 1987, at Lauder, New Zealand (45° S, 170° E). From [65].*

tween 80° and 95°. Curves of the AMFs as a function of SZA for each layer are shown in Fig. 4.3. Figure 4.3*a* shows the AMFs for a diurnally invariant absorber which does not change with solar zenith angle. Figure 4.3*b* shows the calculated twilight air mass factors when changes in the chemical partitioning of NO_2 along the path are included.

To demonstrate the need to include the effects of chemical changes at twilight

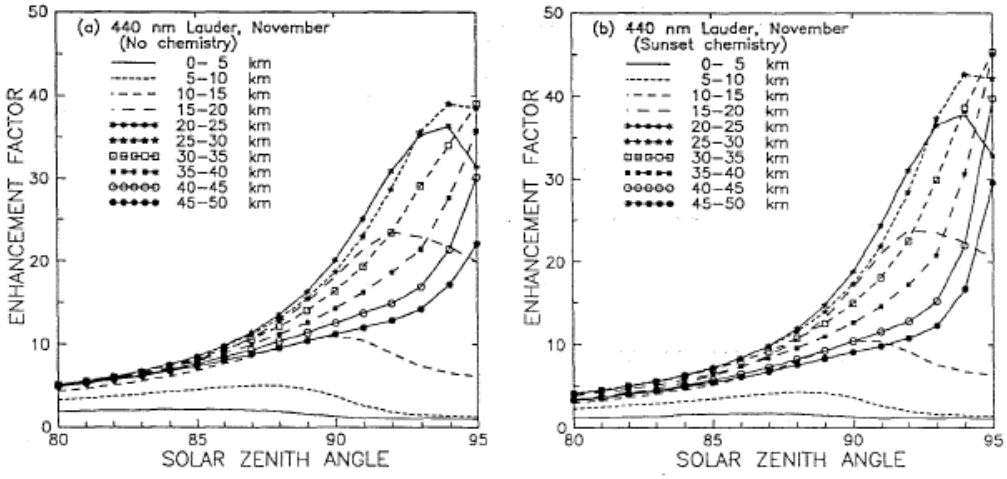

Figure 4.3: *Calculated air mass factors for assumed 5-km-thick slabs of NO_2, for November, 45° S: (a) without considering chemical changes, and (b) with NO_2/NO conversion chemistry. From [65].*

to derive NO_2 profiles, NO_2 profiles were calculated in [65] using both the air mass factors which do not include chemistry and the air mass factors which include chemistry.
Retrieved sunrise and sunset profiles of NO_2 from Lauder are shown in Figs. 4.4 and 4.5 using the air mass factors shown in Figs. 4.3*a* and 4.3*b*, respectively. Both in Fig. 4.4 and in Fig. 4.5 the abscissae are the column densities in units of 10^{14} molecules·cm^{-2} retrieved within each 5-km layer. These columns can be converted to mean concentrations in units of 10^9 molecules·cm^{-3} within each layer by dividing by $5{\cdot}10^5$.

In chapter 5, results of application of the Chahine inversion method will be presented. The retrieval method is modified for application to Multiple AXis DOAS measurements. The modified method retrieves profile information by use of various lines of sight at the same SZA, whereas the original method retrieves profile information by use of only one line of sight (the vertical one) but various SZAs, as seen in the discussion above.
Since measurements at different off-axis angles in directions near the horizon are especially sensitive to the absorbers in the lower troposphere, the Chahine relaxation method can be used in this case to retrieve the vertical profile of atmospheric absorbers in the troposphere and boundary layer.

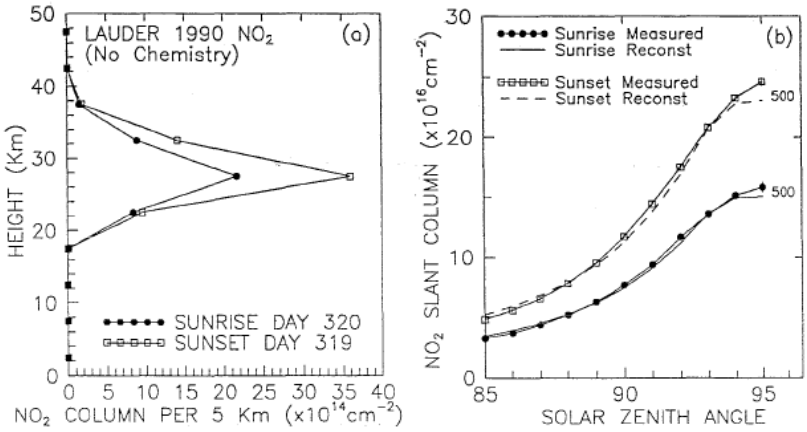

Figure 4.4: *Results of profile calculations, ignoring chemical changes at twilight. (a) NO_2 profiles at sunset (day 319) and sunrise (day 320), 1990, from obsrevations at Lauder, New Zealand. The abscissae are the column densities in units of 10^{14} molecules·cm^{-2} retrieved within each 5-km layer. (b) Observed variation of NO_2 during twilight compared with recalculated variation based on the retrieved profile to illustrate the fitting errors for the derived profile. From [65].*

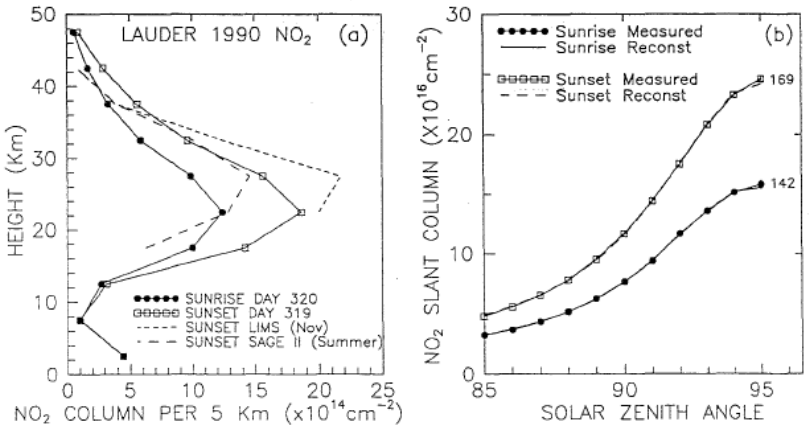

Figure 4.5: *As for Fig. 4.4, but for air mass factors that include chemistry. (a) Retrieved profiles at Lauder, but also showing satellite-measured sunset profiles of NO_2 from LIMS and SAGEII for comparison. (b) Observed variation at twilight compared with the recalculated variation. From [65].*

Chapter 5

Case study: retrieval of nitrogen dioxide and ozone vertical profiles in the boundary layer

To demonstrate the application of Multiple AXis Differential Optical Absorption Spectroscopy to tropospheric studies, one day of measurements carried out at Castel Porziano (near Rome) in October 2006 using a MAX-DOAS instrument will be analysed in this chapter for nitrogen dioxide and, to a lesser degree, for ozone. Not only the vertical column density, but especially the concentration profile of the target trace gases will be retrieved, making use of the radiative transfer model PROMSAR and of the Chahine inversion method, which have been described in chapters 3 and 4, respectively.
Results presented in this chapter are integral part of a manuscript recently submitted to the TGRS (*Transactions on Geoscience and Remote Sensing*) journal [66].

5.1 The measurement site

The Castel Porziano Estate (41.74 N, 12.40 E) is located about 20 km south of Rome and 3 km from the Tyrrhenian cost, as shown in Fig. 5.1. The territory measures approximately 60 km^2.

Since 1994 a comprehensive program promoted by the Italian General Secretariat of the President of the Republic has been underway to perform biological, climatic, physical and chemical monitoring of the Castel Porziano Estate, which was declared by the Italian Ministry for Environment a natu-

rally preserved area. In particular, the Atmosphere Working group pursued two main objectives: the studying of atmospheric quality and the contribution, through the collection of a wide atmospheric data base, to the construction of the environmental monitoring system of this Estate. This work

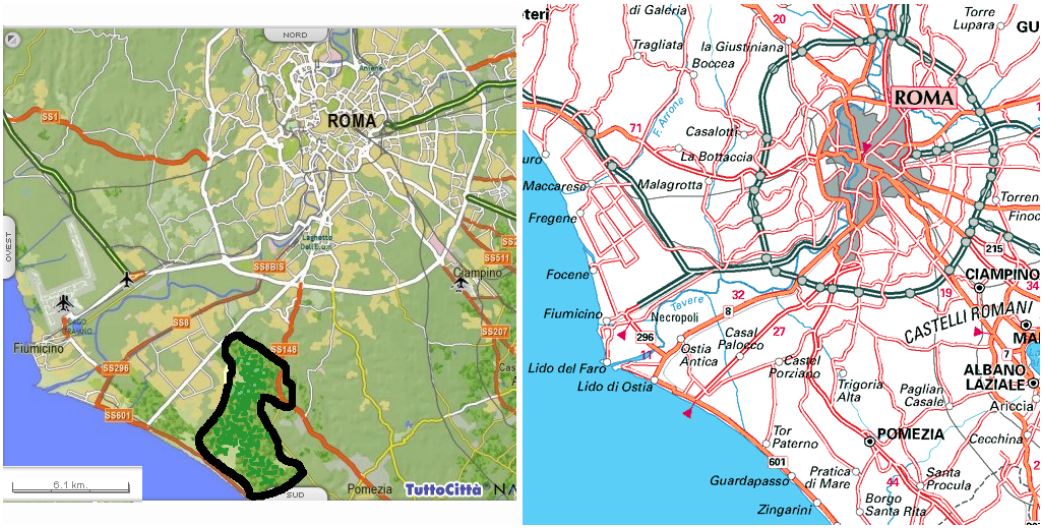

Figure 5.1: *(left) The Castel Porziano Estate (black outlined area) covers a territory of about 60 km^2 located about 20 km south the city of Rome on the Tyrrhenian coast. (right) The figure shows a more detailed map of the area: besides Rome and Castel Porziano, the important meteorological station of Pratica di Mare (located about 10 km south of Castel Porziano), and the airports of Ciampino and Fiumicino are indicated.*

involved also an investigation of the meteorology in the territory where Castel Porziano is located, because the circulation of air masses, which are responsible for pollutants transportation, depends on local meteorological conditions too. These conditions are particularly affected by the wind pattern, controlled by the sea thermal effects, by the "heat island" forming on Rome, and by the hill system behind the metropolitan area.

In 2006, the reasearch group of ISAC-CNR (Institute of Atmospheric Sciences and Climate-National Research Council) within which I was working, took part in the program, for performing remote sensing measurements of atmospheric trace gases, in particular nitrogen dioxide and ozone. It was decided to use a Multiple AXis DOAS instrument (see section 5.2).

5.2 The instrumental set-up

The basic principle of the MAX-DOAS instrument is that scattered solar light is collected by a telescope from different directions and then transmitted to a spectrometer using a quartz fibre boundle. The spectra are recorded by a detector and saved on a PC that also controls the whole set-up.

The UV/visible spectrometer used at Castel Porziano, called TROPOGAS (TROPOspheric GASCOD, where GASCOD means Gas Analyzer Spectrometer Correlating Optical Differences) [67], features a custom-built monochromator based on a Jobin-Yvon holographic spherical grating with N=1200 grooves/mm, blaze maximized at 320 nm, a focal length of 300 mm and entrance slit of 0.1 mm × 8 mm. The linear dispersion and resolution are about 2.4 nm/mm and 0.7 nm at 350 nm, respectively. A stepper motor connected to the grating permits the view of the 285-950 nm spectral range in 50-60 nm single intervals.

The detector used is a 2D (1100 × 330 pixels) back-illuminated SITe CCD (Charge Coupled Device). In order to reduce the dark current, the measured signal is binned into a matrix of 1092 columns and 11 rows (in the SITe manufactured CCD sensor, the dark current per pixel is reduced by a factor of $n_{row}\times$ 0.013, where n_{row} is the number of added rows). A Peltier cooling system maintains the detector at a constant operating temperature of (-30.0 ± 0.1)° C. A small integrating sphere with diameter of 60 mm, equipped with Hg and Quartz-Iodine tungsten lamps, is incorporated into the system for spectral calibrations, as well as for checking the CCD performance and the overall instrumental spectral characteristics.

The small telescope with both azimuthal and zenithal movements transmits the radiation collected at a given direction to the spectrometer by means of an optical fibre.

Finally, a PC sets the configuration of the system and controls the automatic measurements.

Figure 5.2 shows some pictures of various components of the instrumental set-up. Continuous measurements with this set-up (installed inside a van) were performed at Castel Porziano from September until November 2006 in the wavelength region from 436 nm to 510 nm.

5.3 Data analysis and results

From the data set of the measurement period, the detailed analysis of one day, 29 October, is presented exemplary.
Local meteorological conditions on 29 October have been considered in the

Figure 5.2: *(left) Picture of the van interior, with the spectrometer, PC and telescope mounted on the tripod. (middle) Picture of the TROPOGAS spectrometer and PC for row data acquisition and preliminary plotting. (right) Picture of the small telescope designed for Multiple AXis DOAS measurements. It is connected to the spectrometer by optical fibre and is powered by a stepper motor for both zenithal and azimuthal movements.*

discussion because the circulation of air masses and, consequently, the pollutants transportation, largely depend on meteorology.

5.3.1 Meteorological conditions on 29 October 2006

The meteorological station closest to the measurement site is the Pratica di Mare station, located about 10 km south of Castel Porziano, as shown in Fig. 5.1 (right).
Table 5.1 shows the daily mean values of the meteorological parameters temperature, pressure, wind direction/speed, and precipitation for the days in the week between 25 and 31 October 2006. Figure 5.3 shows the daily mean temperatures for the same period registered at the Pratica di Mare station and compared to the climatologic temperature values. It is evident from Fig. 5.3 that the daily mean temperatures (green line) are higher than the climatological temperature values (dashed black line) for all the days in that week. Figure 5.4 moreover shows the wind data registered at the Pratica di Mare station, which indicate that the prevailing wind direction on 29 October was from north-east.
Figures 5.5 and 5.6 show, respectively, the surface weather map and the 500 hPa weather map at 12 UTC (Coordinated Universal Time) on 29 October, which have been made available by the German meteorological Service (http://www.dwd.de). It can be noticed from Fig. 5.5 that most of Italian peninsula, and the Castel Porziano Estate area in particular, are not interested by the cold front system extending over the northern Italy. It can moreover be seen that the measurement area is situated into a high level

Table 5.1: *Daily mean meteorological data measured at the Pratica di Mare station in the week 25-31 October 2006. T_{mean}=mean temperature, T_{max}=maximum temperature, T_{min}=minimum temperature, DD=wind direction, ff=wind speed, V_{max}=maximum wind speed, RR=precipitation.*

Day	Temperature			Wind			Pressure	Rain
	T_{mean} °C	T_{max} °C	T_{min} °C	DD °	ff m/s	V_{max} m/s		RR mm
25/10/06	19.7	24.2	15.4	145	3.8	11.1	1016.0	0
26/10/06	19.4	24.6	16.0	144	1.9	8.9	1019.4	0
27/10/06	20.1	28.0	14.8	326	2.2	8.0	1022.7	0
28/10/06	19.4	24.8	14.8	332	3.7	9.9	1021.8	0
29/10/06	18.5	23.4	14.8	33	1.3	7.0	1015.5	0
30/10/06	17.6	23.4	13.8	168	0.3	8.9	1012.6	0
31/10/06	15.4	21.4	10.8	36	4.6	12.0	1015.6	0

pressure system (both Figs. 5.5 and 5.6) which indicates that the day under study was a fine meteorological day. This was also a day without cloud influence.

5.3.2 Slant column measurements of NO_2 and ozone

Multiple AXis DOAS measurements were performed at the off-axis angles 20°, 40°, 60°, 70°, 75°, 80°, 84°, 87°, 88°, 89°, and 90° (angles between the line of sight direction and the vertical) and with the telescope pointed to a fixed azimuth of 115° (south-east direction). The measurements were taken quasi simultaneously in the different lines of sight so as to avoid complications due to changes in the atmospheric composition during a measurement cycle.

The spectra measured with the above described set-up have been analysed using the DOAS method. As explained in chapter 2, in this technique, only the narrowband, i.e. the differential structures of the absorption cross sections are used to identify absorbers and quantify their integrated amount along the light path (the *slant column density*, SCD). Broadband absorption, extinction by Mie and Rayleigh scattering and broadband instrumental features are removed by a polynomial of low order. This polynomial as well as the differential absorption cross sections of all relevant absorbers together with a reference spectrum usually taken at high sun are fitted to the logarithm of the measured spectra, so as to obtain the slant column density of the species under investigation.

The slant column densities of nitrogen dioxide and ozone deduced from the spectra measured at Castel Porziano, were retrieved employing fitting

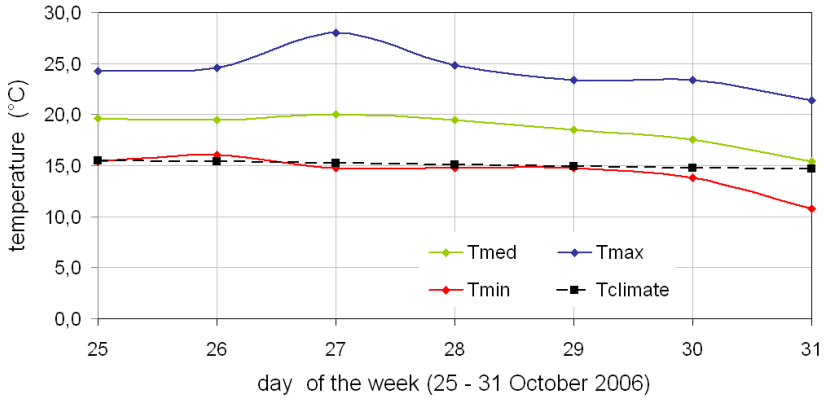

Figure 5.3: *Daily mean temperatures (maximum, minimum and mean values) for the days in the week from 25 to 31 October 2006 measured at the Pratica di Mare station, located about 10 km South of Castel Porziano. Also the climatologic values of temperature are shown.*

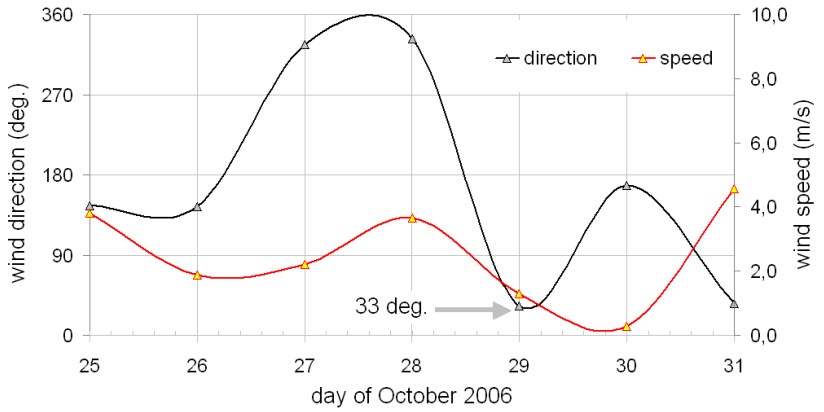

Figure 5.4: *Daily averages of wind direction and speed measured at the Pratica di Mare station from 25 to 31 October 2006.*

windows from 436 nm to 464 nm and 487 nm to 510 nm, respectively. Although ozone shows a stronger absorption in the UV than in the visible, as shown in chapter 1, Fig. 1.3, the (487-510) nm interval was chosen because the ozone absorption cross section in the visible is less temperature dependent, and the intensity of available radiation at ground is stronger in the visible than in the UV, allowing a better signal to noise ratio, a short integration time and, therefore, a better time resolution.

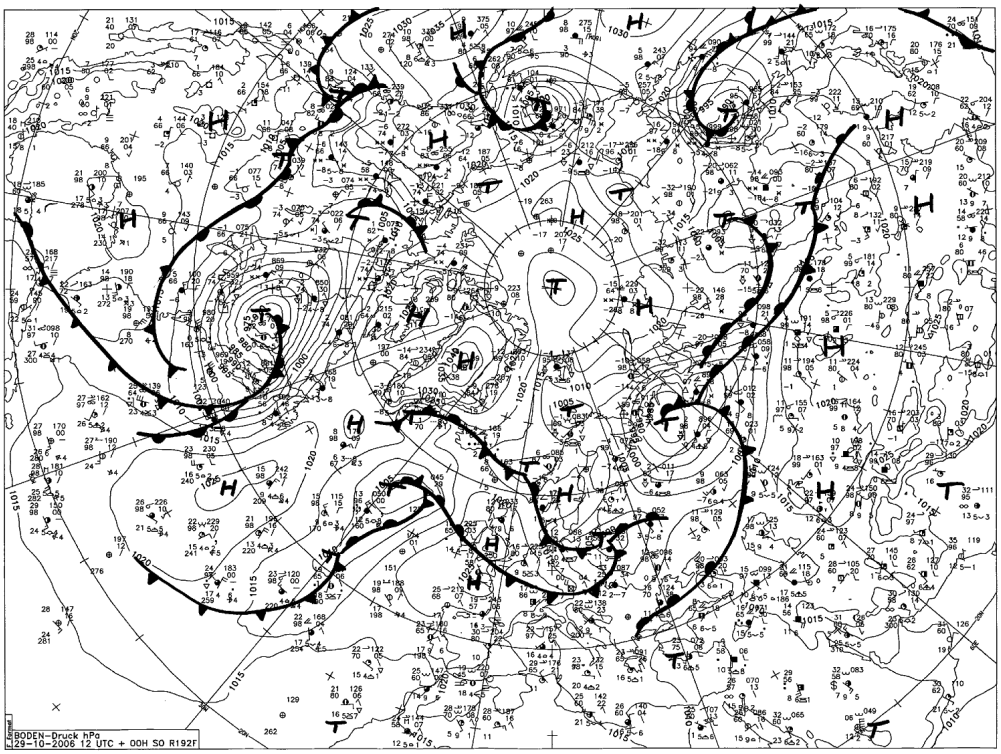

Figure 5.5: *Surface weather map at 12 UTC 29 October 2006. German meteorological Service (http://www.dwd.de).*

In Fig. 5.7, panel A, the diurnal variation of the measured nitrogen dioxide slant column densities on 29 October 2006 is shown. In panel B, blue and grey colors have been used to distinguish between each about one minute long cycle of measurements at different off-axis angles. The red sequence has been zoomed in panel C, in order to show the dependence of the slant column densities on the off-axis angle at which they are measured. In panel C the light blue area indicates the four off-axis directions actually used for the profile retrieval, 84°, 87°, 88°, 89°, which have been chosen to lay particular emphasis on absorption in the boundary layer. The time series slant column densities of nitrogen dioxide measured at these four directions are shown more in detail in Fig. 5.8.

The diurnal variation of the measured ozone slant column densities on 29 October 2006 is shown in Fig. 5.9. Panels A, B, and C show, respectively, the measurements taken at all zenithal directions, a zoomed sequence of measurements around midday, and the four slant column densities considered

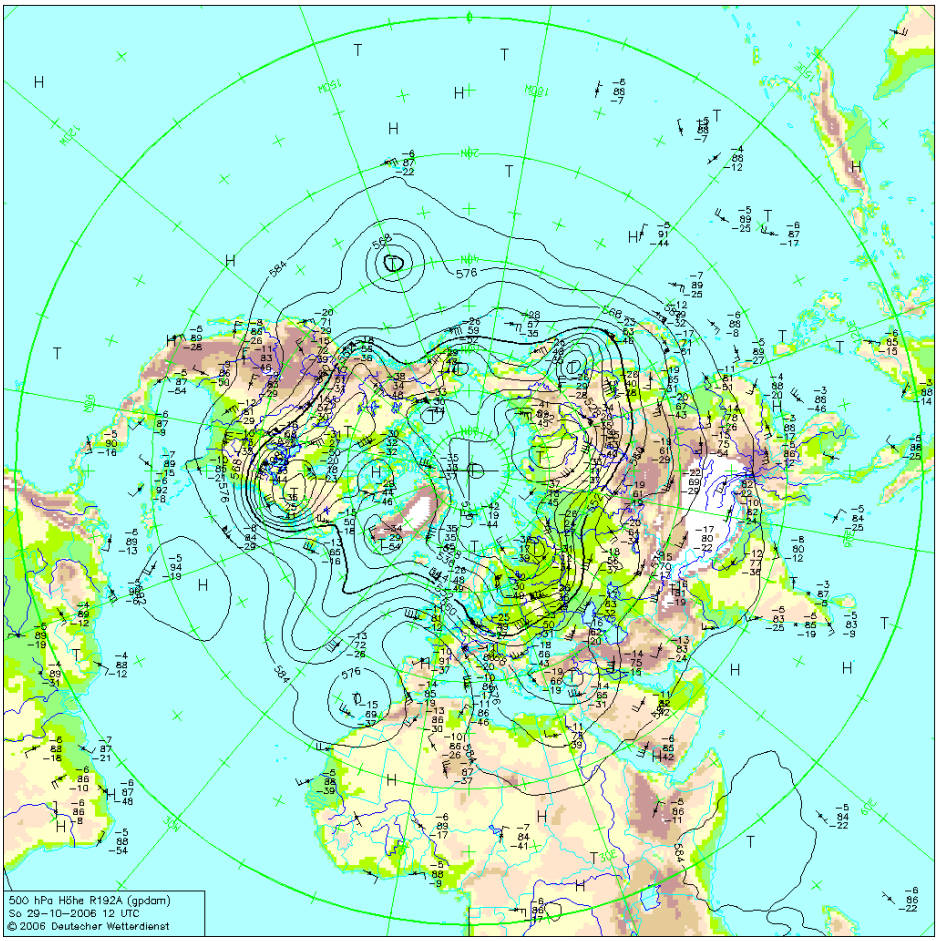

Figure 5.6: *500 hPa weather map at 12 UTC 29 October 2006. German meteorological Service (http://www.dwd.de).*

in the profile retrieval.

The ligth path for the MAX-DOAS geometry is enhanced in the lower atmosphere compared to zenith sky measurements (see chapter 2, Fig. 2.1). In particular, for the measurements at the four off-axis angles 84°, 87°, 88°, and 89° described here, the photon path is affected by multiple scattering effects which necessitate comparison of the measured slant column densities with model calculations in order to gain vertical column densities and profile information of the absorbers. When modelling the radiative transfer in the atmosphere, a number of parameters has to be set to realistic values. The most important ones are the viewing geometry, the position of the sun, wavelength, and the vertical profiles of absorbers, pressure and temperature.

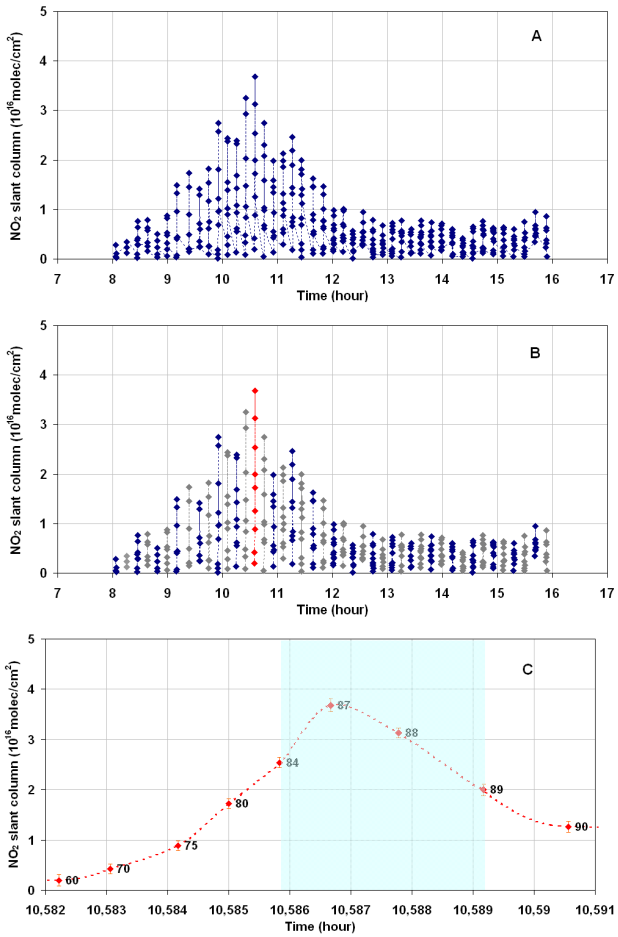

Figure 5.7: *MAX-DOAS NO_2 slant column densities measured at Castel Porziano on 29 October 2006. A: The whole ensemble of measurements taken at the azimuthal direction of 115° and at a sequence of twelve off-Axis angles (OA) repeated from 8 a.m. to 4 p.m. (local time). B: the same as in A, every sequence of measurement being represented by blue and grey colors. The red color sequence has been zoomed in panel C. C: the sequence of nine OA measurements (60°-89°) around 10:35 local time, the interval considered for the inversion being displayed (light blue area).*

However, the atmospheric aerosol loading also has an impact on the results.

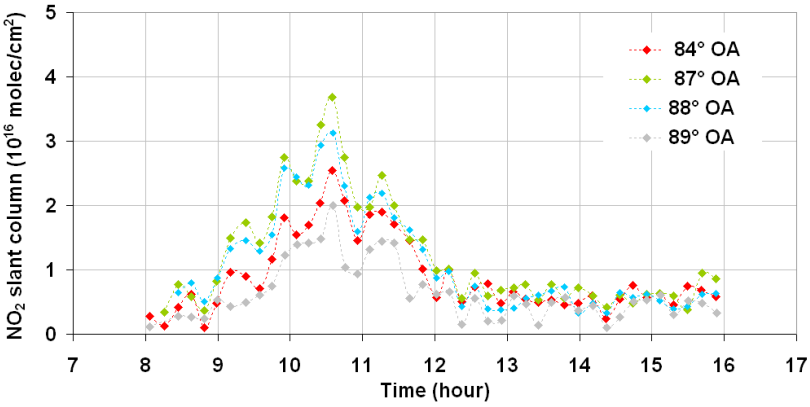

Figure 5.8: *MAX-DOAS NO_2 slant column densities measured at Castel Porziano on 29 October 2006. Only the four off-axis measurements considered for the inversion have been displayed, corresponding to 84°, 87°, 88°, and 89°.*

5.3.3 AMF calculation and aerosol setting

The output of the DOAS analysis are the slant column densities. To convert these into vertical column densities, which are independent of the viewing geometry, air mass factors (AMFs) have to be calculated with a radiative transfer model. The AMF is defined as the ratio of the slant to the vertical column density of a given absorber (see Eq. 2.5, chapter 2). In the present study, AMFs were computed by the radiative transfer model PROMSAR (see chapter 3). This model is able to calculate the air mass factor of selected trace gases taking into account multiple scattering and different aerosol scenarios. Both these aspects greatly affect the light paths in the lowest atmosphere and have to be considered in the analysis of MAX-DOAS measurements.

The length of the light path through the atmosphere and thus the observed optical depth of a trace gas will depend on the amount and optical properties of aerosol particles present in the atmosphere. In general, increasing the aerosol extinction reduces the light path for the lower viewing directions but has litte impact on the zenith-like directions, thereby reducing the difference in tropospheric absorption path for the different viewing directions.

Assuming the properties of atmospheric aerosols and therefore the light path distribution is known, it is possible to retrieve information on the vertical profile of atmospheric trace gases by measuring their optical depth at different viewing directions. However, a complementary way of retrieving information on the state of the atmosphere is to use measurements of the optical depths

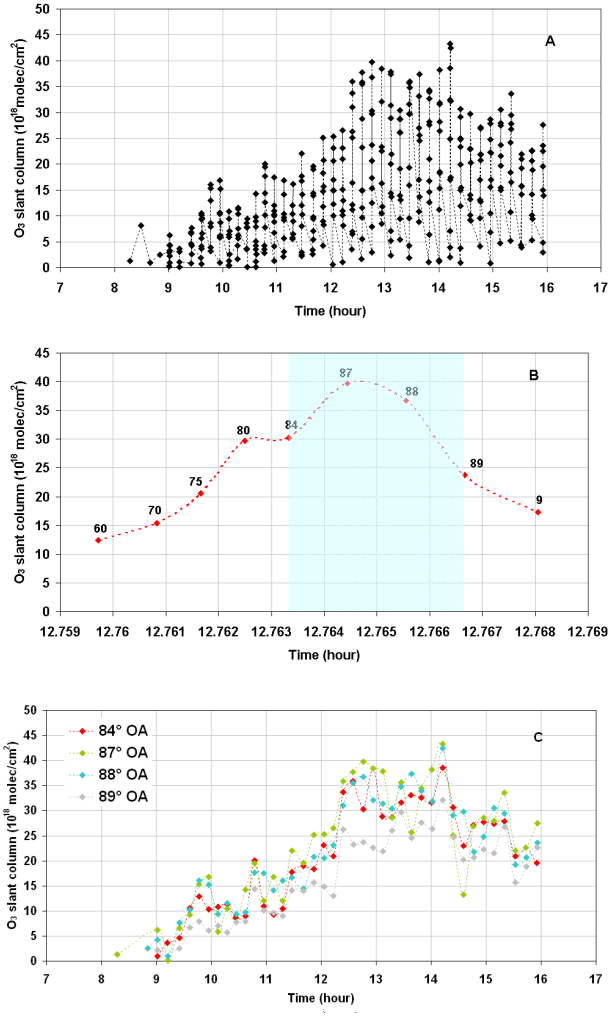

Figure 5.9: *MAX-DOAS O_3 slant column densities measured at Castel Porziano on 29 October 2006. A: The whole ensemble of measurements taken at the azimuthal direction of 115° and at a sequence of twelve OA repeated from 8 a.m. to 4 p.m. (local time). B: the sequence of nine OA measurements (60°-89°) at about 12 local time, the interval considered for the inversion being displayed (light blue area). C: the four OA measurements considered for the inversion (84°, 87°, 88°, 89°).*

along different lines of sight for an absorber with known vertical profile. This provides information on the vertical distribution and optical properties of atmospheric aerosols [68]. Recent studies (e.g. [69]) illustrate that the oxygen dimer O_4 is ideally suited for this approach. The concentration of O_4 is pro-

portional to the square of the O_2 concentration and therefore exponentially decreasing with altitude with a scale height of approximately 4 km. Since the majority of O_4 is located close to the surface, the optical depth of O_4 is very sensitive to changes in the light path distribution at low altitudes.
Deriving the aerosol properties from the O_4 measurements consists in simulating with a radiative transfer model the vertical columns of O_4 varying the aerosol extinction profile and composition, and comparing the simulated columns to the measured ones until closure for all lines of sight has been reached.

O_4 has some absorption bands in the UV/visible spectral region. However, during the measurement campaign at Castel Porziano, we used two spectral intervals optimised for NO_2 and ozone retrieval which do not include useful O_4 absorption bands. For that reason, within the present study, we didn't use the above described criterion to identify the aerosol scenario needed to perform the radiative transfer simulations and calculate the AMFs of the trace gases under investigation. We founded our criterion on the assumptions made about the origin of air masses arriving over Castel Porziano on 29 October 2006, based on the wind direction data analysis (see section 5.3.1) and on backward trajectory calculations, which will be discussed in section 5.3.4. Taking into account that the prevailing wind direction on 29 October was from the north-east (the direction of Rome), the AMFs have been simulated using an urban aerosol extinction profile taken from the MODTRAN library, with visibility of 5 km and 23 km in the boundary layer and in the free troposphere, respectively. In the stratosphere, the aerosol loading was that of a background aerosol setting and a cloud-free model was assumed.

In Fig. 5.10 the AMFs (actually box-AMFs, see chapter 2) at 440 nm and SZA=50°, 80° are shown. As expected, the largest values of AMFs are found for the largest off-axis angles and the lowest atmospheric layers, in agreement with what discussed in chapter 2. These strongly extended absorption paths in the lowest few kilometers cause the high sensitivity of MAX-DOAS observations for the boundary layer. For smaller off-axis angles, the box-AMFs for the lowest atmospheric layers decrease monotonously. For the highest atmospheric layers, the box-AMF converges towards the geometrical approximation for a solar zenith angle of 50° ($1/\cos(50°) \sim 1.56$) and a solar zenith angle of 80° ($1/\cos(80°) \sim 5.76$), as shown in Fig. 5.11.

5.3.4 The retrieval of NO_2 and ozone vertical profiles

The retrieval theory presented in chapter 4, in particular the Chahine algorithm, can be applied to derive the vertical profile of nitrogen dioxide and

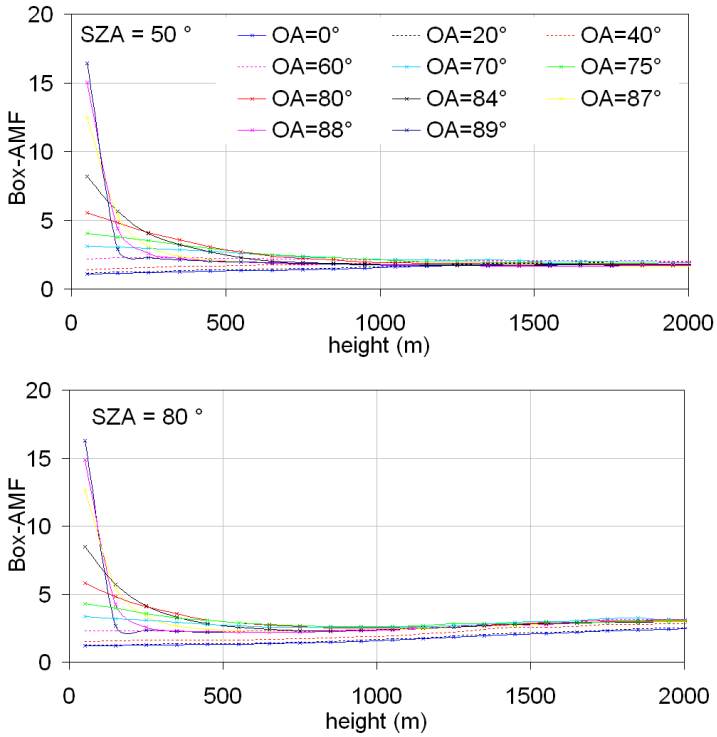

Figure 5.10: *Box-AMFs for 440 nm as a function of altitude. The of-axis angles increase from 0° (zenith) to 89°. (top) SZA=50°, (bottom) SZA=80°.*

ozone in the boundary layer from the measured slant column densities, shown in Figs. 5.8 and 5.9 (bottom).

While the vertical profile of a trace gas is a continuous function in the real atmosphere, it has to be approximated by a discrete function and, therefore, sampled at a finite number of points in the retrieval process. The vertical resolution of retrieved profiles depends on the number of viewing directions, SZA, aerosol loading and surface albedo but is in the order of 3 to 5 layers for the lower troposphere [70]. This means that, depending on measurement conditions, between 3 and 5 pieces of information can be retrieved.
Figure 5.12 shows the vertical profiles of nitrogen dioxide and ozone resulting from application of the Chahine inversion algorithm to the measured SCDs. NO_2 and ozone concentrations in the lower troposphere are driven by a series of factors, such as the presence of sources and sinks, the chemical transformations and the transport. All these factors lead to a strong variability of such species both in space and time. For non urban sites typical values of NO_2 and ozone in the boundary layer range from 1 to 20 ppb and from 10 to

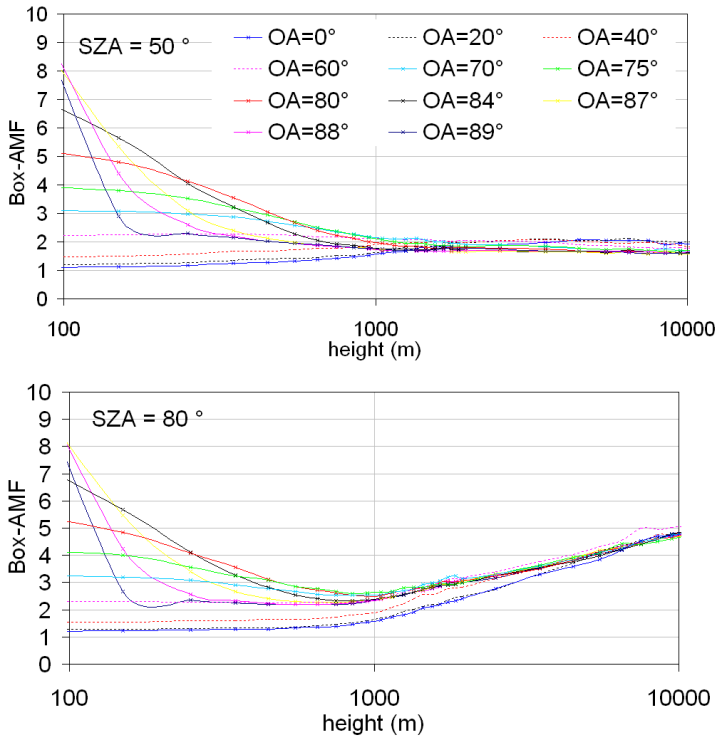

Figure 5.11: *Box-AMFs for 440 nm as a function of altitude (logarithmic scale). The off-axis angles increase from 0° (zenith) to 89°. (top) SZA=50°, (bottom) SZA=80°.*

100 ppb, respectively (see e.g., [71],[72], and [5]). Since it was not possible to use in this study climatological mean profiles as the initial guess, as it would be appropriate, the initial guess profiles used were that NO_2 had a concentration exponentially decreasing with altitude (a constant mixing ratio with altitude) and ozone has a homogeneous constant concentration with altitude. The vertical profiles have been retrieved at four altitude levels, 50 m, 350 m, 650 m, and 1150 m. The first level was set to 50 m for two main reasons. First, this altitude was deduced from simple geometric considerations based on the greatest off-axis angle used (89°) and the PROMSAR-estimated length of the path (∼3 km) the photons cover, on average, when collected at this line of sight. Second, this choice prevents light reflected by the ground or obstacles from entering the field of view of the instrument. The other levels correspond to the heights for which averaging kernels show the highest retrieval sensitivity. The averaging kernels (see chapter 4 for the formal treatment) define the sensitivity of the retrieved profiles to changes of the

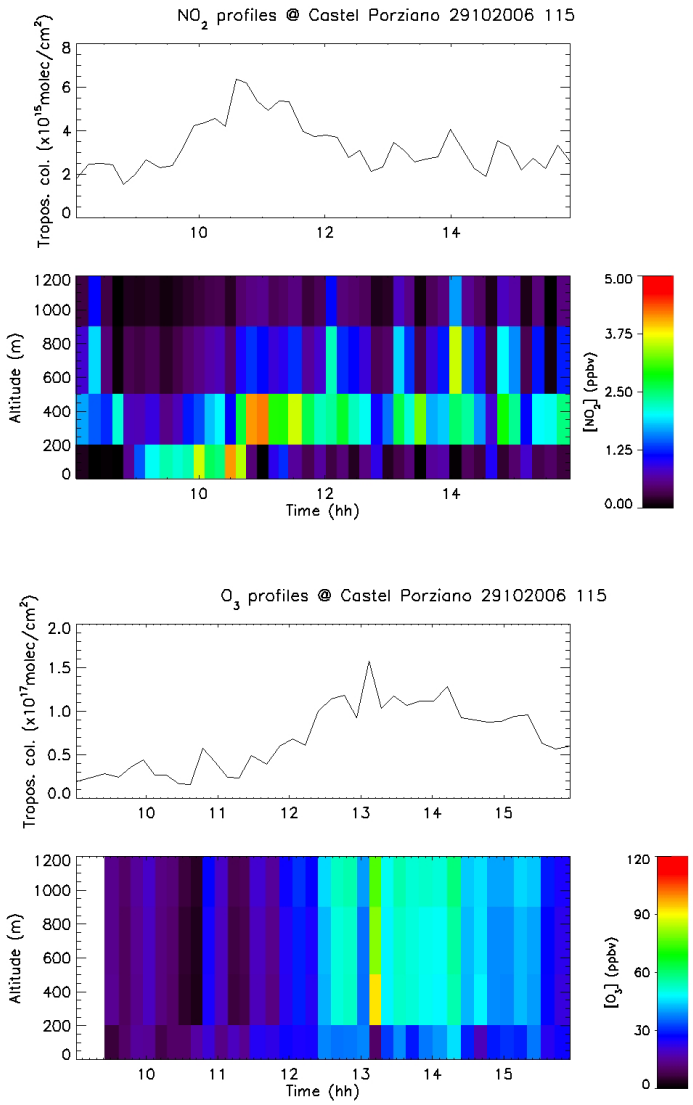

Figure 5.12: *NO_2 (top) and O_3 (bottom) concentration profiles and vertical column densities in the boundary layer deduced from a set a MAX-DOAS measurements taken at four off-axis angles (84°, 87°, 88°, 89°) and at the azimuthal direction of 115°. Measurements have been carried out at the Presidential Estate of Castel Porziano (20 km South-West of Rome) on 29 October 2006.*

real atmospheric profiles; in other words they demonstrate how much the retrieval algorithm is able to reproduce a given input profile. For example, Fig. 5.13 illustrates the capability of the retrieval algorithm in reproducing four

input profiles (the dashed red lines) with the gas concentrated, respectively, at 50 m, 350 m, 650 m, and 1150 m (the four altitudes of the retrieval). Solid red lines represent the retrieved profiles. The averaging kernels corresponding to the four levels of the retrieval are shown in Fig. 5.14. Figures 5.13 and

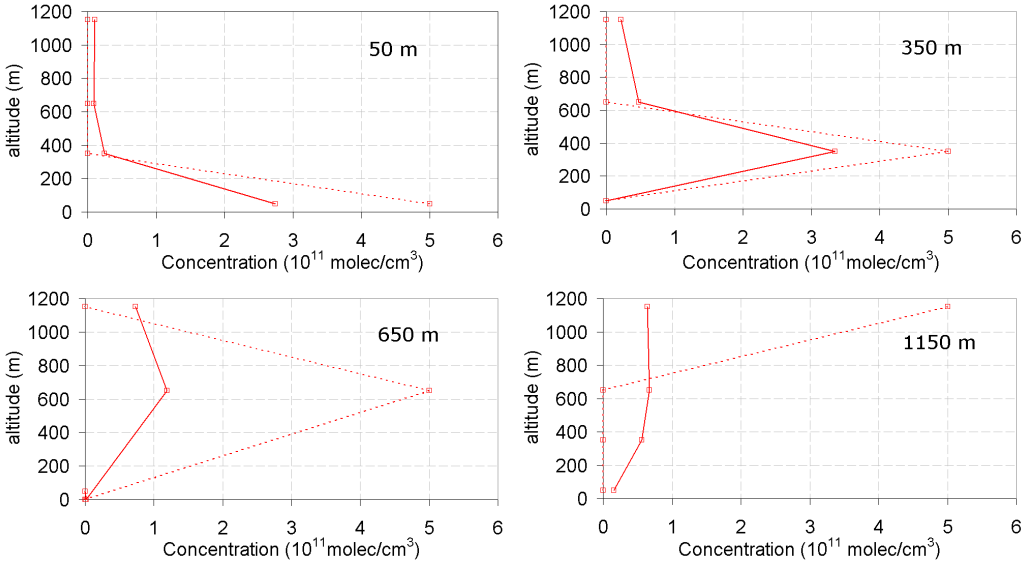

Figure 5.13: *The profiles obtained through inversion of the slant column amounts simulated using different input profiles have been compared with the input profiles themselves. From this analysis, the averaging kernels are calculated.*

5.14 illustrate that at most three pieces of information can be retrieved. Essentially no information (other than that contained in the first guess profile), in fact, was found to come from the upper level (1150 m) meaning that the retrieval algorithm is not able to detect changes in the true profile at 1150 m. Concerning the other levels, the averaging kernel at 50 m shows that the retrieval algorithm is able to detect close to 55% of change in the true profile, the averaging kernel at 350 m close to 70%, and the averaging kernel at 650 m close to 20%. We can conlude, therefore, that the resolution of the retrieved profiles is of 3 layers between 0 to 2 km. Finally, the averaging kernels shown in Figs. 5.13 and 5.14 reveal a better sensitivity of the profile retrieval at 350 m. The maxima of the weighting functions are indicators for the altitude from which we obtain most of the information for a given line of sight.

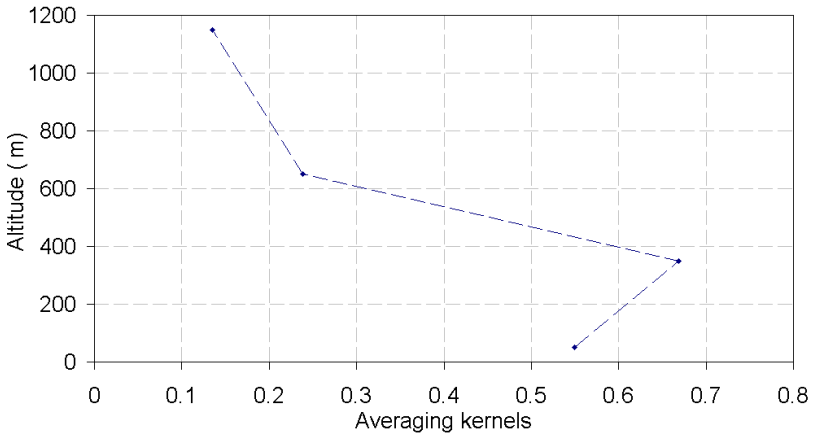

Figure 5.14: *Averaging kernels.*

Considerations about the retrieved profiles and validation

Figure 5.12 shows the retrieved vertical profile of NO_2 and O_3 and their vertical column density from 0 to 2 km, calculated by integrating the concentration values from the lower to the upper level of retrieval. The vertical columns reach maximum values of about $6 \cdot 10^{15}$ molecules/cm^2 for nitrogen dioxide and $1.5 \cdot 10^{17}$ molecules/cm^2 for ozone. Moreover, the vertical columns of NO_2 and O_3 are anti-correlated, which is indicative of their daily photochemical cycle. NO_2, in fact, is known to produce ozone after some delay and it is not surprising that the ozone amount is fairly uniform from about 12:20 to 14:20. As for the spike in ozone at about 13:05 and the minimum at 12:55, we can exclude any artefact and hypothesize a correlation with transport.

Comparing the vertical columns in the boundary layer with similar independent quantities can be useful for checking the correctness of the retrieval algorithm. As for nitrogen dioxide, for example, we have compared the vertical column shown in Fig. 5.12 (top) with the tropospheric vertical column obtained from satellite observations. In particular, we refer to the measurements carried out by the Ozone Monitoring Instrument (OMI) spectrometer ([73], [74]), a Dutch-Finnish monitoring instrument that flies on the Earth Observing System (EOS) NASA's Aura satellite, launched in January 2004. OMI is a nadir viewing, near-UV and visible spectrograph which draws heavily on European experience in atmospheric research instruments such as GOME (flying on ERS-2), SCIAMACHY and GOMOS (both flying on ENVISAT). OMI's nadir spatial resolution ranges from 13 $\times$ 24 km to 24

× 48 km , depending on the instrument's operating mode.
Figure 5.15 shows the mean tropospheric vertical columns of nitrogen dioxide from OMI instrument, carried out on 29 October 2006. Such columns

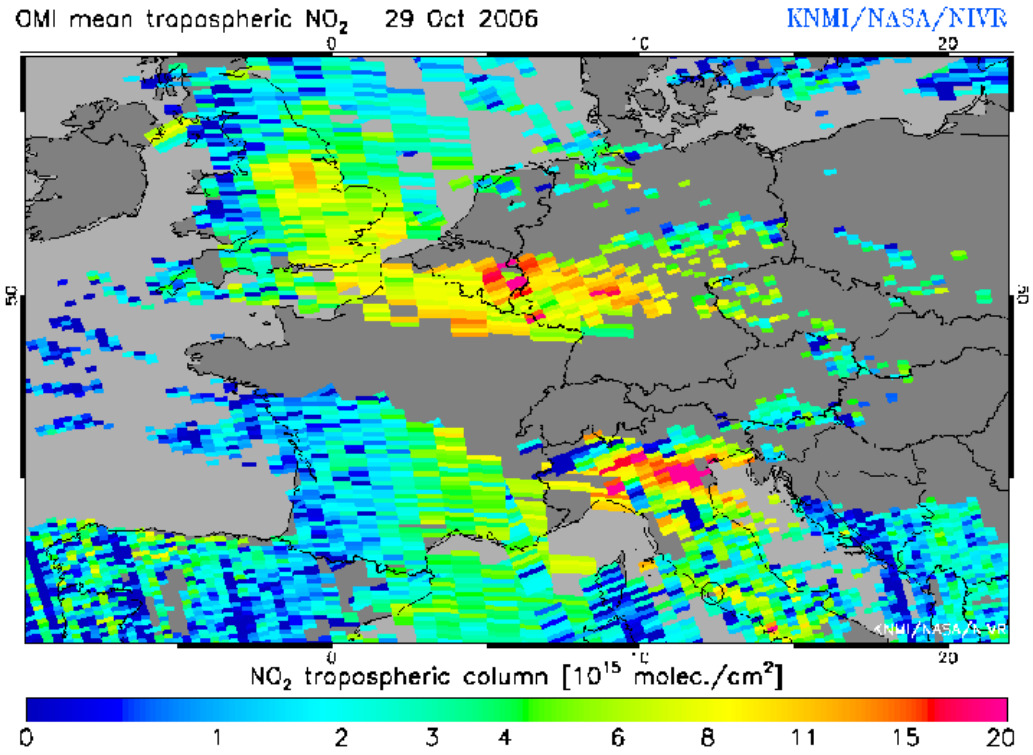

Figure 5.15: *NO_2 tropospheric columns from OMI on 29 October 2006.*

range from about $6 \cdot 10^{15}$ molecules/cm^2 to about $10 \cdot 10^{15}$ molecules/cm^2. A good agreement is therefore found with the vertical column amounts in the boundary layer deduced from MAX-DOAS measurements.

In order to focus our discussion on nitrogen dioxide we analyse Fig. 5.16, which shows the daily evolution of the NO_2 vertical profile at 50 m, 350 m, and 650 m. Also error bars are shown in Fig. 5.16, calculated according to the analysis of averaging kernels discussed previously. Figures 5.16 and 5.12 show that the highest NO_2 values are found at 350 m (with a peak of about 5 ppb at 10:45), although the initial guess profile of nitrogen dioxide had a concentration exponentially decreasing with altitude. This suggests that NO_2 was probably transported over the Castel Porziano Estate from remote sources, rather than local ones. Because of the absence of independent *in-situ* measurements using e.g. balloon and aircraft-borne instruments, a *real* validation of these retrieved profiles was not allowed. Nevertheless, we

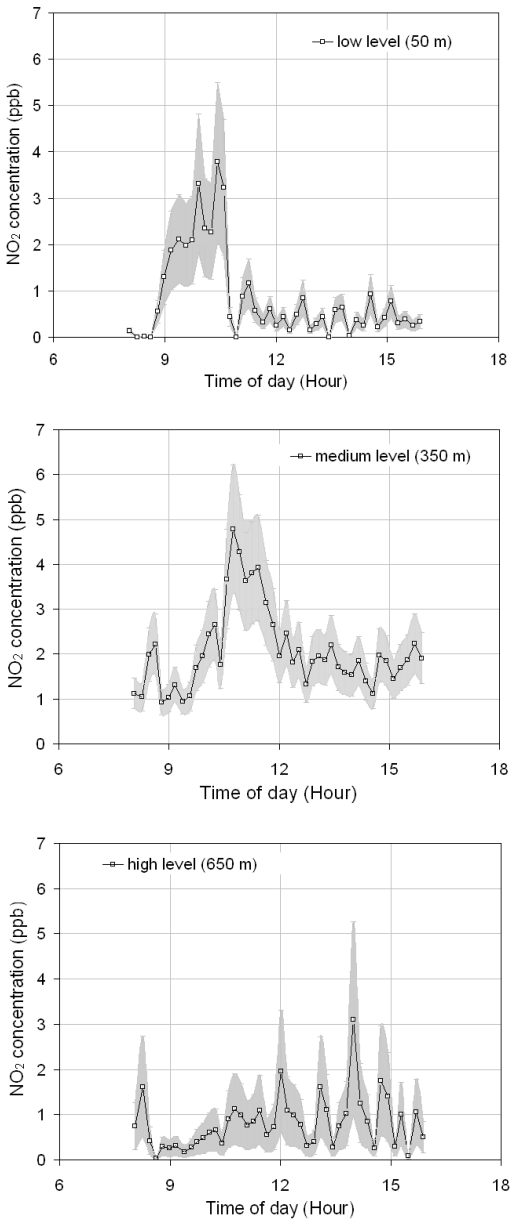

Figure 5.16: *Diurnal evolution of nitrogen dioxide vertical profile at different altitude levels, as deduced by means of the retrieval inversion algorithm.*

performed a set of simulations with the Hybrid Single Particle Lagrangian Integrated Trajectory (HYSPLIT) model, initialized with synoptic meteorological fields produced by the National Weather Service's National Centers

for Environmental Prediction (NCEP) and archived at the NOAA Air Resources Laboratory (GDAS1 archive), in order to calculate the backward trajectories of the polluted air masses arriving over the Castel Porziano area during the day under examination.
Figure 5.17 shows the backward trajectories ending at 9 UTC (10 a.m. local time) computed at three altitude levels (red: 50 m, blue: 250 m, green: 500 m., a.s.l.) on 29 October 2006. It can be seen that the prevailing direction

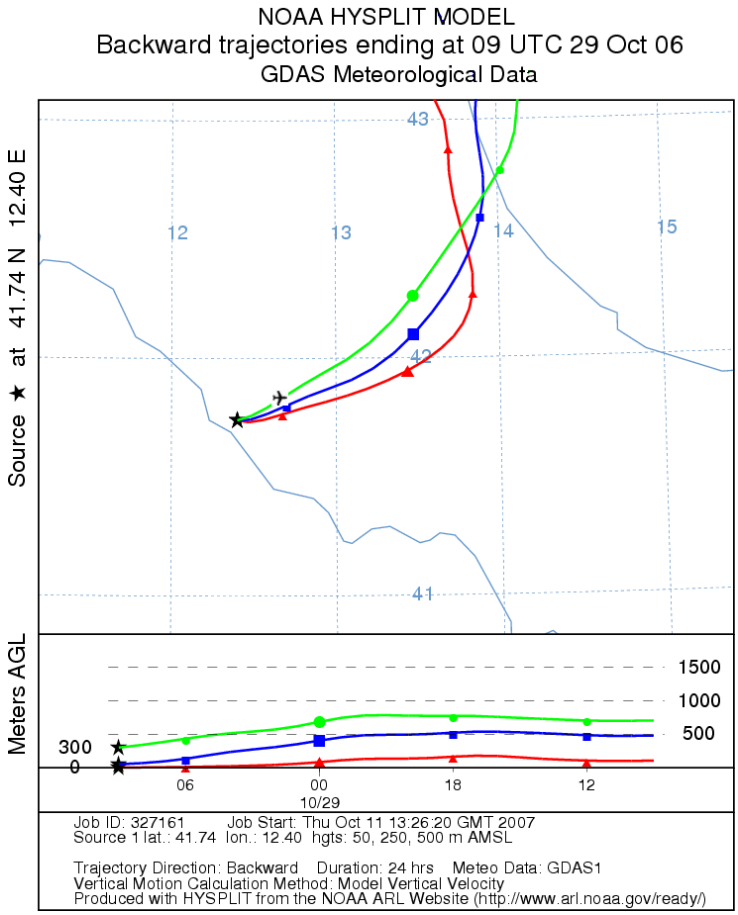

Figure 5.17: *Trajectories ending at Castel Porziano on 29 October 2006. Castel Porziano (41.74 N, 12.40 E) is indicated by the star symbol. Red, blue and green lines indicate, respectively, back trajectories ending exactly at Castel Porziano at different altitude levels (red: 50 m, blue: 250 m, green: 500 m). Trajectories have been computed with the Hybrid Single Particle Lagrangian Integrated Trajectory (HYSPLIT) model, provided by the NOAA Air Resources Laboratory. The Ciampino airport (41.80 N, 12.60 E) is also indicated.*

of air masses resulting from the HYSPLIT model was the North-East direction, which corresponds to Ciampino Airport (41.80 N, 12.60 E) and the areas of heavy traffic surrounding the city of Rome. It can be noticed that the air mass coming from the Ciampino airport has been sampled at Castel Porziano less than two hours later, a time interval which is shorter than the NO_2 lifetime [5].
Trajectories ending at 8 UTC and 10 UTC were also computed (not shown here), and turned out to be very similar to those ending at 9 UTC. Figure 5.18 also shows the backward trajectories ending at 9 UTC computed at three different altitude levels (red: 50 m, blue: 250 m, green: 500 m., a.s.l.) on 25, 26, 27, 28, 29, and 30 October 2006. The mean wind data recorded at the Pratica di Mare station and shown in Fig. 5.4 confirme that the prevailing wind direction measured on 29 October 2006 was from North-East.

Retrieval method performances

The retrieval method performances can be evaluated, for example, by comparison between the measured and recalculated (i.e. simulated) slant column densities for the different off-axis directions. Figure 5.19 shows the agreement between the observed and recalculated NO_2 SCDs at 84°, 87°, 88°, and 89°. The observed SCDs are directly obtained from MAX-DOAS observations and recalculated SCDs are the model calculated values deduced from retrieved vertical profiles for the day under study. The fitting is good, with percent differences displayed in Fig. 5.20.

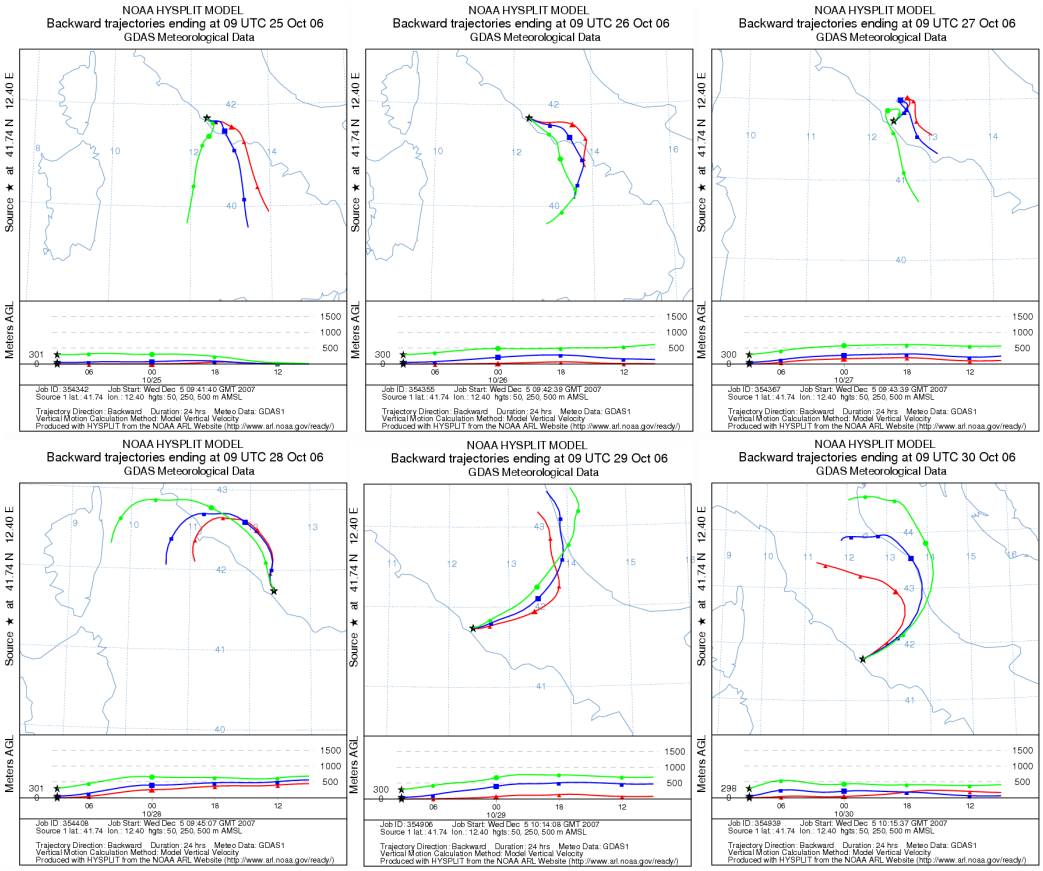

Figure 5.18: *Trajectories ending at Castel Porziano on 25, 26, 27, 28, 29, and 30 October 2006. In every panel Castel Porziano (41.74 N, 12.40 E) is indicated by the star symbol. Red, blue and green lines indicate, respectively, back trajectories ending exactly at Castel Porziano at different altitude levels (red: 50 m, blue: 250 m, green: 500 m). Trajectories have been computed with the Hybrid Single Particle Lagrangian Integrated Trajectory (HYSPLIT) model, provided by the NOAA Air Resources Laboratory.*

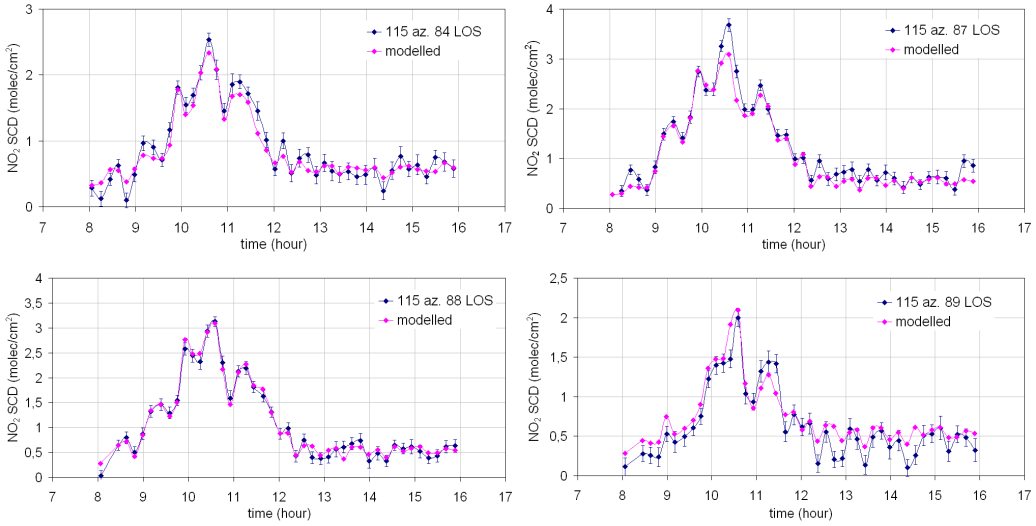

Figure 5.19: *Measured and recalculated nitrogen dioxide slant column densities at 84°, 87°, 88°, and 89°.*

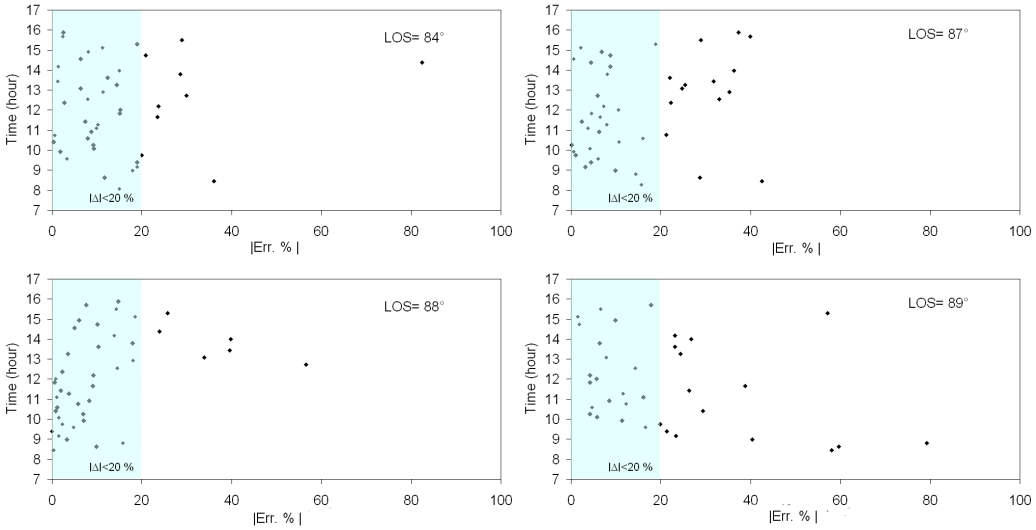

Figure 5.20: *Percent errors distribution of the measured and simulated slant column densities shown in Fig. 5.19.*

Conclusions

A recent development in ground-based remote sensing of atmospheric consituents by UV/visible absorption measurements of scattered light is the simultaneous use of several directions in addition to the traditional zenith-sky pointing: this technique is referred to as Multiple AXis Differential Optical Absorption Spectroscopy (MAX-DOAS).

As well as zenith-looking DOAS, Multiple AXis DOAS can detect the presence of a trace gas in terms of its integrated concentration over an atmospheric path, the so called *slant column density*. A special feature of the MAX-DOAS technique, however, are the off-axis viewing directions close to the horizon, showing stronger signal of tropospheric absorbers than zenith-sky observations, particularly sensitive to stratospheric absorbers. In this way, the MAX-DOAS represents a new approach to the problem of measuring tropospheric concentrations of some atmospheric trace gases by observing their absorption in UV/visible scattered sunlight. Depending on tropospheric visibility, the light path in the lower atmospheric layers can become very long using the MAX-DOAS configuration and increases as the viewing direction approaches the horizon. Information from the different lines of sight can be used to derive the vertical profile of the absorbers of interest, in the troposphere and even in the boundary layer.

Retrieval of profile information from the slant column density of a given trace gas couldn't be performed without (1) accurately modelling of the light path with radiative transfer models (RTMs) and (2) application of effective inversion techniques.

The ability to properly interpret UV/visible absorption measurements of atmospheric constituents using scattered light, in fact, depends crucially on how well the optical path of light collected by the system is understood. This knowledge is essential to convert the slant column density of the absorber, which can be derived from the absorption measurements, into a *vertical column density* (the concentration of the absorber integrated along the vertical), with the help of the so-called *Air Mass Factor* (AMF). This factor is defined as the ratio of the slant column density to the vertical column density and

can be used to quantify the enhancement of the light path length within the absorber layers.
In the case of zenith-sky DOAS measurements, calculations of the air mass factor have been made using "simple" single scattering radiative transfer models. For measurements with the telescope pointing toward the horizon, however, multiple scattering has to be taken into account. In addition, the full treatment of atmospheric sphericity in the radiative transfer including refraction turns out to be necessary at low sun.

A useful approach to take into account such aspects and, moreover, to deal with all physical parameters affecting the light paths, to support all DOAS geometries, and treat multiple scattering with varying phase functions involved, is the Monte Carlo approach. The development and application of the Monte Carlo radiative transfer model PROMSAR (PROcessing of Multi-Scattered Atmospheric Radiation) is a major concern of the research presented in this thesis.
Besides calculating the air mass factor, which is the fundamental output for the interpretation of remote sensing measurements, the PROMSAR model also calculates the atmospheric transmittance, the solar direct and diffuse irrandiance and the radiance, for a detector with assigned central coordinates, diameter, direction cosines of the normal to the detector surface, line of sight and field of view. As a validation, the radiometric quantities and the air mass factors calculated by the PROMSAR model have been extensively compared with the same quantities computed by other radiative transfer models: the MODTRAN code, as for the transmittance, irradiance and radiance calculations, and eigth different state-of-the-art RTMs from seven international research groups, as for the AMF and radiance calculations.

In order to derive the vertical concentration profile of a trace gas from its slant column density, the AMF is only one part in the quantitative retrieval process. The other indispensable requirement is a robust approach to solve for the equation system composed from the AMFs, the measurements and the unknown concentrations: that is, an inversion method. Within the present study, after dealing with the retrieval theory in general, mainly following the work of Rodgers, the Chahine relaxation method has been presented. This method was successfully used in the past by several authors to estimate the profile information contained in zenith-sky DOAS measurements at different solar zenith angles using ground-based instruments. The vertical resolution of such profiles was, however, relatively low (from 5 to 10 km) and information was limited mainly to the stratospheric part of the profile. Within the study presented in this thesis, the Chahine inversion method has been modified so as to be applied for inversion of ground-based Multiple AXis DOAS measurements. The aim is the retrieval of the vertical profile of the

trace gases of interest in the lower troposphere and boundary layer, which is possible taking advantage of the variation of the slant column measurements with the off-axis angle instead of variation with the solar zenith angle, as in the case of zenith-sky measurements.

One day of measurements carried out at Castel Porziano (41.74 N, 12.40 E), near Rome, in October 2006 using a MAX-DOAS instrument have been, finally, presented. The amount of profile information that can be retrieved from such measurements, in particular, is investigated for the trace gases NO_2 and, to a lesser degree, for ozone. Even if uncertainties remain in the retrieved profiles mainly due to the lack of independent observations and of a climatology for comparison, the results indicate that the pollutants are probably transported over Castel Porziano from remote sources, mainly the Ciampino airport and the heavy traffic area surrounding the city of Rome. This hypotesis finds confirmation in the backward trajectory calculations carried out with the HYSPLIT model and the wind data recorded at the Pratica di Mare meteorological station, located near the area under study.

In summary, ground-based Multiple AXis Differential Optical Absorption Spectroscopy, combined with appropriate radiative transfer models and inversion techniques, is a promising tool for atmospheric studies in the lower troposphere and boundary layer, including the retrieval of profile information with a good degree of vertical resolution. This thesis has presented an application of this powerful comprehensive tool for the study of a preserved natural Mediterranean area where pollution can only be transported from remote sources.

Application of this tool in densely populated or industrial areas is beginning to look particularly fruitful and represents an important subject for future works. In these areas the most important source of NO_2 are anthropogenic emissions; since all NO_2 emissions affect the boundary layer directly, the monitoring of the NO_2 levels in the boundary layer is getting more and more important. In the troposphere NO_2 is an important trace gas since its photochemistry is also involved in the production of tropospheric ozone. Thus the monitoring of NO_2 concentrations in these areas is necessary because ozone and nitrogen dioxide itself are harmful species affecting both human health and the growth of vegetation. To understand the NO_2 (actually, NO_x) and ozone chemistry in more detail not only the concentrations at ground but also the acquisition of the vertical distribution of the trace gases is necessary. Thus a tool to resolve the vertical profile information is really important. A MAX-DOAS instrument, together with a sophisticated radiative transfer model and a retrieval method are a tool with promising applications.

Appendix

Urban and free tropospheric NO_2 and O_3 chemistry

In this Appendix, some chemical reaction pathways primarily involving nitrogen dioxide and ozone are described for the free troposphere and urban regions. The omitted reactions can be found, for example, in [5] and [11].

Photostationary-state ozone concentration

In the background troposphere, the ozone (O_3) mixing ratio is determined primarily by a set of three reactions involving itself, nitric oxide (NO), and nitrogen dioxide (NO_2). These reactions are:

$$NO + O_3 \longrightarrow NO_2 + O_2 \tag{1}$$

$$NO_2 + h\nu \longrightarrow NO + O \qquad \lambda < 420\ nm \tag{2}$$

$$O + O_2 \longrightarrow O_3 \tag{3}$$

where $h\nu$ implies a photon of solar radiation and λ is the wavelength of the radiation. Background tropospheric, mixing ratios of O_3 (20 to 60 ppbv) are much higher than those of NO (1 to 60 pptv) or NO_2 (5 to 70 pptv). Because the mixing ratio of NO is much lower than is that of O_3, reaction 1 does not deplete ozone during the day or night in background tropospheric air. In urban air reaction 1 can deplete local ozone at night because NO mixing ratios at night may exceed those of O_3.

If k_1 ($cm^3 \cdot molecule^{-1} \cdot s^{-1}$) is the rate coefficient of reaction 1 and J (s^{-1}) is the photolysis rate coefficient of reaction 2, the volume mixing ratio of ozone can be calculated from these two reactions as

$$\chi_{O_3} = \frac{J}{N_d k_1} \cdot \frac{\chi_{NO_2}}{\chi_{NO}} \tag{4}$$

where χ is volume mixing ratio (molecule of gas per molecule of dry air) and N_d is the concentration of dry air (molecules of dry air per cubic centimeter). This equation is called the **photostationary-state relationship**. The equation does not state that ozone is affected by only NO and NO_2. Indeed, other reactions affect ozone, including ozone photolysis. Instead, Eq. 4 predicts a relationship among NO, NO_2, and O_3. If two of the three concentrations are known, the third can be found from the equation.

Two important reactions aside from Eqs. 1-3 that affect ozone are:

$$O_3 + h\nu \longrightarrow O_2 + O(^1D) \qquad \lambda < 310\ nm \tag{5}$$

$$O_3 + h\nu \longrightarrow O_2 + O \qquad \lambda > 310\ nm \tag{6}$$

where $O(^1D)$ is the excited atomic oxygen. In the free troposphere, the liftime of ozone against destruction by these reactions are about 0.7 and 14 h, respectively. The lifetime of ozone against destruction by NO is in general longer than lifetime of ozone against photolysis. Thus, in the daytime free troposphere, photolysis destroys ozone faster than does reaction with NO. When the ozone concentration changes due to photolysis, the χ_{NO_2}/χ_{NO} ratio in Eq. 4 changes to adapt to the new ozone concentration.

The photostationary-state relationship in Eq. 4 is useful for free tropospheric analysis. In urban air, though, the relationship often breaks down because reactions of NO with organic gas radicals provide an additional impotant source of NO_2, not included in Eq. 4. When organic-radical concentrations are large, as they are during the morning in urban air, the photostationary-state relationship does not hold. In afternoon, though, organic gas concentrations in urban air decrease, and the relationship holds better.

When excited atomic oxygen forms, as in Eq. 5, it rapidly produces O by

$$O(^1D) \overset{M}{\rightleftharpoons} O \tag{7}$$

and O rapily produces O_3 by Eq. 3. The reactions 3 and 5-7 cycle oxygen atoms quickly among among $O(^1D)$, O, and O_3. Losses of O from the cycle, such as from conversion of NO to NO_2 by Eq. 1, are slower than are transfers of O within the cycle.

Daytime removal of nitrogen oxides

During the day, NO_2 is removed slowly from the photostationary-state cycle by the reaction

$$NO_2 + OH \xrightarrow{M} HNO_3 \tag{8}$$

where M represents any other molecule which, while not directly involved in the chemical reaction, can carry away excess energy formed in the reaction. Because molecular oxygen O_2 and nitrogen N_2 together make up more than 99 percent of the gas molecules in the air today, M is most likely to be O_2 or N_2. Although HNO_3 photolyzes back to NO_2 + OH (for $\lambda < 335$ nm), its lifetime against photolysis is 15 to 80 days, depending on the day of the year and the latitude. Because this lifetime is faily long, HNO_3 serves as sink for **nitrogen oxides** NO_x (= NO + NO_2) in the short term. In addition, because HNO_3 is soluble, much of it dissolves in cloud drops or aerosol particles before it photolyzes back to NO_2.
Reaction 8 requires the presence of the **hydroxyl radical** (OH), an oxidizing agent that decomposes (scavenges) many gases. Given enough time, OH breaks down every organic gas and most inorganic gases in the air. The globally averaged tropospheric OH concentration is about 8×10^5 molecules cm^{-3}. Its daytime concentration in the clean free troposphere usually ranges from 2×10^5 to 3×10^6 molecules cm^{-3}. In urban air, OH concentration typically ranges from 1×10^6 to 1×10^7 molecules cm^{-3}.
The primary free-tropospheric source of OH is the pathway

$$O_3 + h\nu \longrightarrow O_2 + O(^1D) \qquad \lambda < 310\ nm \tag{9}$$

$$O(^1D) + H_2O \longrightarrow 2OH \tag{10}$$

Most of the $O(^1D)$ atoms produced by reaction 9 dissipate their excess energy as heat and eventually recombine with O_2 to form O_3, which is a *null cycle* (i.e., it has no net chemical effects). However, a small fraction ($\sim$0.01) of the $O(^1D)$ atoms reacts with water vapour to form two hydroxyl radicals as in reaction 10. Thus, the OH concentrations in the free troposphere depend on ozone and water vapour contents. In the upper troposphere, H_2O is scarce, limiting the ability of reaction 10 to produce OH. Minor sources of OH in the free troposphere are photolysis of gases, some of which are produced by OH itself. For example, **nitrous acid** (HONO), produced during the day by the reaction of NO with OH, rapidly photolyzes to produce OH and NO ($\lambda < 400$ nm). HONO concentrations are high only during the early morning because the photolysis rate increases as sunlight becomes more intense during the day. During the night, HONO is not produced from gas-phase reactions, since OH, required for its production, is absent at night. HONO is produced from gas-particle reactions and emitted from vehicles during day and night.

Once formed, the OH radical is a powerful oxidant that reacts quickly (the lifetime of OH in the atmosphere is only about one second) with a number of atmospheric pollutants: NO_2 to form HNO_3 (reaction 8), CO to form CO_2, H_2S to form SO_2, SO_2 to form H_2SO_4, CH_2O to form CO, and so

on. Because of its pivotal role in transforming a large number of tropospheric gases (many of which are major pollutants) into their oxidized forms, OH has been referred to as the "atmopshere's detergent".

Nighttime nitrogen chemistry

During the night, reaction 2 shuts off, eliminating the major chemical sources of O and NO. Because O is necessary for the formation of ozone, ozone production also shuts down at night. Thus, at night, neither O and NO, nor O_3 is produced chemically. If NO is emitted at night, it destroys ozone by reaction 1. Because NO_2 photolysis shuts off at night, NO_2 becomes avalilale to produce NO_3, N_2O_5, and HNO_3 at night by the sequence

$$NO_2 + O_3 \longrightarrow NO_3 + O_2 \tag{11}$$

$$NO_2 + NO_3 \overset{M}{\rightleftharpoons} N_2O_5 \tag{12}$$

$$N_2O_5 + H_2O \longrightarrow 2HNO_3 \tag{13}$$

Reaction 11 occurs during the day as well, but, during the day, it is less important than NO+O_3, an the NO_3 produced from the reaction is photolyzed almost immediately by solar radiation

$$NO_3 + h\nu \longrightarrow NO + O_2 \tag{14}$$

and

$$NO_3 + h\nu \longrightarrow NO_2 + O \tag{15}$$

Although NO_3 is much less reactive than OH, at night it is present in higher concentrations than OH is during the day.
Reaction 12 is a reversible reaction. At high temperature, such as during the day, the reverse reaction occurs within seconds. At low temperature, such as at night, is occurs within hours or days or even months.
Reaction 13 is an heterogeneous reaction, occurring on aerosol or hydrometeor particle surfaces.

Ozone production in the background troposphere: an air pollution problem

Ozone plays a key but dichotomous role in the atmosphere. In both the troposphere and the stratosphere it is a key reactant. In the stratosphere ozone absorbs dangerous UV radiation, thereby protecting life on Earth. In

the troposphere it is a potent pollutant, toxic to humans and vegetation due to its oxidizing power on biological tissues, but it is also the source of the "detergent" OH.
Besided being involved in the photostationary-state relationship (4), O_3 is produced in the troposphere from the oxidation of the carbon monoxide (CO), methane (CH_4) and certain nonmethane organic gases by OH in the presence of NO_x. In densely populated regions with high emissions of NO_x and hydrocarbons, rapid O_3 production can take place and results in a surface air pollution problem.
CO produces ozone by

$$CO + OH \longrightarrow CO_2 + H \tag{16}$$

$$H + O_2 \longrightarrow HO_2 \tag{17}$$

$$NO + HO_2 \longrightarrow NO_2 + OH \tag{18}$$

$$NO_2 + h\nu \longrightarrow NO + O \qquad \lambda < 420\ nm \tag{19}$$

$$O + O_2 \overset{M}{\rightleftharpoons} O_3 \tag{20}$$

Methane, is the most abundant organic gas in the Earth's atmosphere. Its free-tropospheric lifetime against chemical destruction is 8 to 12 years. This long lifetime has enabled it to mix uniformly up to the tropopause. Above the tropopause, its mixing ratio decreases. The methane oxidation sequence producing ozone is

$$CH_4 + OH \longrightarrow CH_3 + H_2O \tag{21}$$

$$CH_3 + O_2 \longrightarrow CH_3O_2 \tag{22}$$

$$NO + CH_3O_2 \longrightarrow NO_2 + CH_3O \tag{23}$$

$$NO_2 + h\nu \longrightarrow NO + O \qquad \lambda < 420\ nm \tag{24}$$

$$O + O_2 \overset{M}{\rightleftharpoons} O_3 \tag{25}$$

Note that in the stratosphere, reaction 21 is an important source of water vapour. As with reaction 17, reaction 22 is fast.

Urban photochemistry and air pollution

Photochemical smog results from the emission of organic gases in the presence of sunlight. It differs from background air in two ways. First, mixing ratios of nitrogen oxides and organic gases are higher in polluted air than in

background air, causing ozone levels to be higher in urban air than in the background. Second, photochemical smog contains higher concentrations of high molecular weight organic gases, particularly aromatic gases, than does background air. Because such gases break down quickly in urban air, most are unable to survive transport to background troposphere.

Photochemical smog involves reactions among **nitrogen oxides** (NO_x = NO + NO_2) and **reactive organic gases** (ROGs, total organic gases minus methane) in the presence of sunlight. The most recognized gas-phase by-product of smog reactions is ozone because has harmful health effects and is an indicator of the presence of other pollutants.

On a typical morning, NO and ROGs are emitted by traffic, power plants, and other combustion sources. Emitted pollutants are **primary pollutants**. ROGs are oxidized to organic peroxy radicals, denoted by RO_2, which react with NO to form NO_2. Pre-existing ozone also convert NO to NO_2. Sunlight then breaks down NO_2 to NO and O. Finally, O reacts with molecular oxygen to form ozone. The basic reaction sequence is thus:

$$NO + RO_2 \longrightarrow NO_2 + RO \tag{26}$$

$$NO + O_3 \longrightarrow NO_2 + O_2 \tag{27}$$

$$NO_2 + h\nu \longrightarrow NO + O \qquad \lambda < 420\ nm \tag{28}$$

$$O + O_2 + M \longrightarrow O_3 + M \tag{29}$$

Pollutants, like ozone, that form chemically or physiscally in the air are **secondary pollutants**.

Because RO_2 competes with O_3 to convert NO to NO_2 in urban air, and because the photostationary state relationship is based on the assumption that only O_3 converts NO to NO_2, the **photostationary relationship is usually not valid in urban air**. In the afternoon, the relationship holds better than it does in the morning because RO_2 mixing ratios are lower in the afternoon than in the morning.

Bibliography

[1] Brasseur, G. P., J. J. Orlando, G. S. Tyndall (eds.), **Atmospheric chemistry and global change**, Oxford University Press, New York, 1999.

[2] Stull, R. B., **An introduction to boundary layer meteorology**, Kluwer Academic Publishers, Dordrecht, 1988.

[3] Solomon, S., R. W. Portmann, R. W. Sanders, J. S. Daniel, W. Madsen, B. Bartram, E. G. Dutton, On the role of nitrogen dioxide in the absorption of solar radiation, *J. Geophys. Res.*, **104** (D10), 12047-12058, 1999.

[4] Wallace, J. M., P. V. Hobbs, **Atmospheric Science, an introductory survey**, Academic Press, San Diego, 1977.

[5] Hobbs P. V., **Introduction to atmospheric chemistry**, Cambridge University Press, 262 pages, 2000.

[6] Rayleigh, L., On the light from the sky, its polarization and colour, *Phil. Mag.*, **41**, 107-20, 1871.

[7] Mie, G., Optics in turbid media, *Ann. Phys.*, **25**, 377-445, 1908.

[8] Waggoner, A. P., R. E. Weiss, N. C. Ahlquist, D. S. Covert, S. Will, R. J. Charlson, Optical characteristics of atmospheric aerosols, *Atmos. Environ.*, **15**, 1891-1909, 1981.

[9] Cass, G. R., On the relationship between sulfate air quality and visibility with examples in Los Angeles, *Atmos. Environ.*, **13**, 1069-1084, 1979.

[10] Tang, I. N., W. T. Womg, H. R. Munkelwitz, The relative importance of atmospheric sulfates and nitrates in visibility reduction, *Atmos. Environ.*, **15**, 2463-71, 1981.

[11] Jacobson, M. Z., **Fundamentals of atmospheric modeling**, Cambridge University Press, 2005.

[12] Schneider, W., G. K. Moortgat, G. S. Tyndall, J. P. Burrows, Absorption cross-sections of NO_2 in the UV and visible region (200-700 nm) at 298 K, *J. Photochem. Photobiol. A: Chem.*, **40**, 195-217, 1987.

[13] Plane, J. M. C., N. Smith, Atmospheric monitoring by differential optical absorption spectroscopy, in **Spectroscopy in Environmental Sciences**, edited by Hester, R. E. and Clark, R. J. H., John Wiley, New York, 223-262, 1995.

[14] Dobson, G. M. B., D. N. Harrison, Measurements of the amount of ozone in the Earth's Atmosphere and its Relation to other Geophysical Conditions, *Proc. R. Soc. London*, **110**, 660-693, 1926.

[15] Götz, P. F. W., A. R. Meetham, G. M. B. Dobson, The Vertical Distribution of Ozone in the Atmosphere, *Proc. Roy. Soc.*, A 145, 416-446, 1934.

[16] Davies, J., Correlation Spectroscopy, *Analytical Chemistry*, **42**, 101-112, 1970.

[17] Hoff, R., M. Millan, Remote SO_2 mass flux measurements using COSPEC. *JAPCA*, **31**, 381-384, 1981.

[18] Hoff, R. M., Differential SO_2 Column Measurements of the Mt. Pinatubo Volcanic Plume, *Geophys. Res. Lett.*, **19**, 175-178, 1992.

[19] Platt, U., **Differential optical absorption spectroscopy (DOAS)**, in Air Monitoring by Spectroscopic Techniques, edited by: Sigrist, M. W., Chemical Analysis Series, **127**, John Wiley, New York, 1994.

[20] Sanders, R. W., S. Solomon, J. P. Smith, L. Perliski, H. L. Miller, G. H. Mount, J. G. Keys, A. L. Schmeltekopf, Visible and Near-Ultraviolet Spectroscopy at McMurdo Station Antarctica, 9. Observations of OClO from April to October 1991, *J. Geophys. Res.*, **98**, D4, 7219-7228, 1993.

[21] Arpaq, K. H., P. V. Johnston, H. L. Miller, R. W. Sanders, S. Solomon, Observations of the stratospheric BrO column over Colorado, 40° N, *J. of Geophys. Res.*, **99**, D4, 8175-8181, 1994.

[22] Miller, H. L., A. Weaver, R. W. Sanders, K. Arpag, S. Solomon, Measurements of arctic sunrise surface ozone depletion events at Kangerlussuaq, Greenland (67°N, 51°W), *Tellus*, **49B**, 496-509, 1997.

[23] Weaver, A., S. Solomon, R. W. Sanders, K. Arpag, H. L. Miller, Atmospheric NO_3 5. Off-axis measurements at sunrise: Estimates of tropospheric NO3 at 40°N, *J. Geophys. Res.*, **101**, D13, 18605-18612, 1996.

[24] Smith, J., S. Solomon, Atmospheric NO_3: 3. Sunrise Disappearance and the Stratospheric Profile, *J. Geophys. Res.*, **95**, D9, 13819-13827, 1990.

[25] Smith, J., S. Solomon, R. Sanders, H. Miller, J. Perliski, J. Keys, A. Schmeltekopf, Atmospheric NO_3: 4. Vertical Profiles at Middle and Polar Latitudes at Sunrise, *J. Geophys. Res.*, **98**, D5, 8983-8989, 1993.

[26] Stutz, J., U. Platt, Numerical Analysis and Estimation of the Statistical Error of Differential Optical Absorption Spectroscopy Measurements with Least-Squares methods, *Appl. Opt.*, **35**, 30, 6041-6053, 1996.

[27] Grainger, J., J. Ring, Anomalous Fraunhofer line profiles, *Nature*, **193**, 762, 1962.

[28] Fish, D. J., R. L. Jones, Rotational Raman scattering and the Ring effect in zenith-sky spectra, *Geophys. Res. Lett.*, **22**, 811-814, 1995.

[29] Sioris, C. E., W. F. J. Evans, Filling in of Fraunhofer and gas absorption lines in sky spectra as caused by rotational Raman scattering, *Appl. Opt.*, **38**, 12, 2706-2713, 1999.

[30] Marquard, L., T. Wagner, U. Platt, Improved Air Mass Factor Concepts for Scattered Radiation Differential Optical Absorption Spectroscopy of Atmospheric Species, *J. Geophys. Res.*, **105**, 1315-1327, 2000.

[31] Solomon, S., A. L. Schmeltekopf, R. W. Sanders, On the interpretation of zenith sky absorption measurements, *J. Geophys. Res.*, **92**, 8311-8319, 1987.

[32] Perliski, L. M. S. Solomon, On the evaluation of air mass factors for atmospheric near ultraviolet and visible absorption spectroscopy, *J. Geophys. Res.*, **98**, 10363-10374, 1993.

[33] Palazzi, E., A. Petritoli, G. Giovanelli, I. Kostadinov, D. Bortoli, F. Ravegnani, S. S. Sackey, PROMSAR: A backward Monte Carlo spherical RTM for the analysis of DOAS remote sensing measurements, *Adv. Space Res.*, **36(5)**, 1007-1014, 2005.

[34] Wagner, T., J. P. Burrows, T. Deutschmann, B. Dix, C. von Friedeburg, U. Frieß, F. Hendrick, K.-P. Heue, H. Irie, H. Iwabuchi, Y. Kanaya, J.

Keller, C. A. McLinden, H. Oetjen, E. Palazzi, A. Petritoli, U. Platt, O. Postylyakov, J. Pukite, A. Richter, M. van Roozendael, A. Rozanov, V. Rozanov, R. Sinreich, S. Sanghavi, F. Wittrock, Comparison of Box-Air-Mass-Factors and Radiances for Multiple-Axis Differential Optical Absorption Spectroscopy (MAX-DOAS) Geometries calculated from different UV/visible Radiative Transfer Models, *Atmos. Chem. Phys.*, **7**, 1809-1833, 2007.

[35] United States Committee on Extension to the Standard Atmosphere: U.S. Standard Atmosphere, 1976, National Oceanic and Atmospheric Administration, National Aeronautics and Space Administration, United States Air Force, Washington D.C., 1976.

[36] Bogumil, K., J. Orphal, T. Homann, S. Voigt, P. Spietz, O. C. Fleischmann, A. Vogel, M. Hartmann, H. Bovensmann, J. Frerik, J. P. Burrows, Measurements of Molecular Absorption Spectra with the SCIAMACHY Pre-Flight Model: Instrument Characterization and Reference Data for Atmospheric Remote-Sensing in the 230-2380 nm Region, *J. Photochem. Photobiol. A.*, **157**, 167-184, 2003.

[37] Lenoble, J. (Editor), Standard Procedures to Compute Atmospheric Radiative Transfer in a Scattering Atmosphere - Volume I, International Association of Meteorology and Atmospheric Physics (IAMAP), Boulder, Colorado, USA, 1977.

[38] Fouquart, Y., W. M. Irvine, J. Lenoble (eds.), Standard Procedures to Compute Atmospheric Radiative Transfer in a Scattering Atmosphere - Volume II, International Association of Meteorology and Atmospheric Physics (IAMAP), Boulder, Colorado, USA, 1980.

[39] Stamnes, K., S-C. Tsay, W. Wiscombe, K. Jayaweera, Numerically Stable Algorithm for Discrete-Ordinate- Method Radiative Transfer in Multiple Scattering and Emitting Layered Media, *Appl. Opt.*,**27(12)**, 2502-2509, 1988.

[40] Plass, G. N., G. W. Kattawar, Monte Carlo calculations of light scattering from clouds, *Appl. Opt.*, **7**, 415-419, 1968.

[41] Plass, G. N., G. W. Kattawar, Radiative transfer in an atmosphere-ocean system, *Appl. Opt.*, **8**, 455-466, 1969.

[42] Tinet, E., S. Avrillier, J. M. Tualle, Fast semianalytical Monte Carlo simulation for time-resolved light propagation in turbid media, *J. Opt. Soc. Am. A*, **13**, 1903-1915, 1996.

[43] Wehrli, C., Extraterrestrial Solar Spectrum, WMO No. 615, July 1985. (http://rredc.nrel.gov/solar/standards/am0/wehrli1985.html)

[44] Halton, J. H., A Retrospective and Prospective Survey of the Monte Carlo Method, *Siam. Rev.*, **12**, 1-63, 1970.

[45] Bielajew, A. F., D. W. O. Rogers, Variance-reduction techniques. In: Jenkins T. M., Nelson W. R., Rindi A. (eds) Monte Carlo transport of electrons and photons. Plenum, New York, pp. 407-419, 1988.

[46] Collins, D. G., W. G. Blättner, M. B. Wells, H. G. Horak, Backward Monte Carlo calculations of the polarization characteristics of the radiation emerging from spherical-shell atmospheres, *Appl. Opt.*, **11**, 2684-2696, 1972.

[47] Blättner, W. G., H. G. Horak, D. G. Collins, M.B. Wells, Monte Carlo studies of the sky radiation at twilight, *Appl. Optics*, **13**(3), 534.547, 1974.

[48] Berk, A., L. S. Berstein, D.C Robertson, MODTRAN: A Moderate Resolution Model of LOWTRAN7, Final Report, GL-TR-0122, AFGL, Hanscom AFB, Maryland, 42 pages, 1989.

[49] Henyey L. C., J. L. Greenstein, Diffuse radiation in the galaxy, *Astrophys. J.*, **93**, 70-83, 1941.

[50] Liou, K. N., **An Introduction to atmospheric radiation**, Amsterdam, Academic Press, 2002.

[51] Anderson, G. P., J. Wong, J. H Chetwynd, MODTRAN3: An Update on Recent Validations Against Airborne High Resolution Interferometer Measurements, Summaries of the Fifth Annual JPL Airborne Earth Science Workshop, JPL Publication 95-1, 1, Pasadena, California, 5-8, 1995.

[52] Sarkissian, A., H. K. Roscoe, D. J. Fish, Ozone measurements by zenith-sky spectrometers: an evaluation of errors in air-mass-factors calculated by radiative transfer models, *J. Quant. Spectrosc. Radiat. Transfer*, **54**, No. 3, pp. 471-480, 1995.

[53] Shettle, E. P., R. W. Fenn, Models of the aerosols of the lower atmosphere and the effects of humidity variations on their optical properties, AFGL-TR-79-0214, 1979.

[54] Stephens, G. L., **Remote Sensing of the Lower Atmosphere, An Introduction**, 523 pp., Oxford University Press, New York, 1994.

[55] Dobson, G. M. B, Forty years' research on atmospheric ozone at Oxford: a history, *Appl. Opt.*, **7**, no. 3, 387-405, 1968.

[56] Mateer, C. L., On the information content of Umkehr observations, *J. Atmos. Sci.*, **22**, 370-381, 1965.

[57] Kaplan, L. D., Inference of atmospheric structure from remote radiation measurements, *J. Opt. Soc. Am.*, **49**, 1004, 1959.

[58] Wark, D. Q., On indirect temperature soundings of the stratosphere from satellites. *J. Geophys. Res.*, **66**, 77, 1961.

[59] Yamamoto, G., Numerical method for estimating the stratospheric temperature distribution from satellite measurements in the CO_2 band, *J. Met.*, **18**, 581, 1961.

[60] Deepak, A., **Inversion methods in atmospheric remote sounding**, Academic Press, 1977.

[61] Rodgers, C. D., Characterisation and error analysis of profiles retrieved from remote sounding measurements, *J. Geophys. Res.*, **95**, 5587-5595, 1990.

[62] Rodgers, C. D., **Inverse methods for atmospheric sounding**, World Scientific, 2000.

[63] Eyre, J. R., On systematic errors in satellite sounding products and their climatological mean values, *Quart. J. Roy. Meteorol. Soc.*, 113, 279, 1987.

[64] Chahine, M. T., Determination of the temperature profile in an atmosphere from its outgoing radiance, *J. Opt. Soc. Am.*, **58**, 1634-1637, 1968.

[65] McKenzie, R. L., P. V. Johnston, C. T. McElroy, J. B. Kerr, S. Solomon, Altitude distributions of stratospheric constituents from ground-based measurements at twilight, *J. Geophys. Res.*, **96**, 15499-15511, 1991.

[66] Palazzi E., A. Petritoli, F. Ravegnani, I. Kostadinov, D. Bortoli, S. Masieri, M. Premuda, G. Giovanelli, Retrieval of Gas Pollutants Vertical Profile in the Boundary Layer by Means of Multiple Axis DOAS, **submitted** to *IEEE Trans. Geo. Rem. Sens.*.

[67] Bortoli D., SPATRAM - SPectrometer for Atmospheric TRAcers Measurements - a Prototype Equipment for the monitoring of minor compounds of the atmosphere, Ph.D. thesis, University of Évora, 2005.

[68] Wagner, T., C. von Friedeburg, M. Wenig, C. Otten, U. Platt, UV-visible observations of atmospheric O_4 absorptions using direct moonlight and zenith-scattered sunlight for clear-sky and cloudy sky conditions, *J. Geophys. Res.*, 107 (D20), 4424, doi:10.1029/2001JD001026, 2002.

[69] Wagner, T., B. Dix, C. von Friedeburg, U. Frieß, S. Sanghavi, R. Sinreich, U. Platt, MAX-DOAS O_4 measurements: A new technique to derive information on atmospheric aerosols-Principles and information content, *J. Geophys. Res.*, 109, D22205, doi:10.1029/2004JD004904, 2004.

[70] Wittrok, F., The retrieval of oxygenated volatile organic compounds by remote sensing techniques, Ph.D. thesis, University of Bremen, 2006.

[71] Pisano, J. T., I. McKendry, D. G. Steyn, D. R. Hastie, Vertical nitrogen dioxide and ozone concentrations measured from a tethered balloon in the Lower Fraser Valley, *Atmos. Environ.*, 31(14), 2071-2078, 1997.

[72] Glaser, K., U. Vogt, G. Baumbach, Vertical profiles of O_3, NO_2, NO_x, VOC, and meteorological parameters during the Berlin Ozone Experiment (BERLIOZ) campaign, *J. Geophys. Res*, 108(D4), Article Number 8253, 2003.

[73] Levelt, P. F., G. H. J. van den Oord, M. R. Dobber, A. Malkki, H. Visser, J. de Vries, P. Stammes, J. O. V. Lundell, H. Saari, The Ozone Monitoring Instrument, *IEEE Trans. Geo. Rem. Sens.*, **44** (5), pp. 1093-1101, 2006.

[74] Loughner, C. P., D. J. Lary, L. C. Sparling, R. C. Cohen, P. DeCola, W. R. Stockwell, A Method to Determine the Spatial Resolution Required to Observe Air Quality From Space, *IEEE Trans. Geo. Rem. Sens.*, **45** (5), pp. 1308-1314, 2007.